THE PHYSICAL SOCIETY
RECEIVED
30 NOV 1959

MEMOIRS

OF THE

COLLEGE OF SCIENCE

UNIVERSITY OF KYOTO

SERIES A

VOL. XXIX, No. 2

September, 1959

KYOTO

THE PHYSICAL SOCIETY

Memoirs of the College of Science, University of Kyoto, Series A,
Vol. XXIX, No. 2, Article 1, 1959.

OPTICAL OBSERVATIONS OF THE SECOND RUSSIAN EARTH SATELLITE

BY

Akira HATTORI* and **Bunta YADA***

(*Received August 27, 1958*)

ABSTRACT

This paper deals with the observations of 1957β carried out at Kwasan Observatory and in cooperation with the Western Japanese Moon Watch Stations. Part I gives the description of instruments used and observational data. In part II, the orbital elements are determined. For example, on March 20.000 (J.S.T.), 1958, the period T was $94.^{m}477 \pm 0.^{m}003$, the eccentricity 0.0434 ± 0.0020, and perigee and apogee heights were 195 km$\pm$14 km and 791 km$\pm$14 km respectively. The inclination of orbit to the equatorial plane, i, is estimated as $65.^{\circ}5 \pm 0.^{\circ}2$. In part III, some results are derived. The period shows erratic variations. $\Delta\Omega$, the retrograde rate of orbit per day, may be connected with the period by an empirical formula: $\Delta\Omega = (1.08 \pm 0.01) \times 10^{5} \cos i \times T^{-2.1 \pm 0.1}$. Finally, air density at about 195 km altitudes above the equatorial regions is estimated as 6×10^{-10} kg m^{-3} to 10×10^{-10} kg m^{-3}.

I. OBSERVATIONS

1. Introduction

It is well known that the calculation of air density from the measured drag of a satellite is one of the frequently suggested uses of the vehicle. Especially, above about 200 km there are no direct determinations of air density or pressure, and air density must be computed from an assumed temperature and molecular weight. But, considering the observations of the satellite orbit, we can evaluate the atmospheric density roughly in the order of magnitude.

In July 1955, the announcement of the American program for the launching of small satellites during the International Geophysical Year was made. Soon after the Russian authorities announced that they were also undertaking the same plan. At Kwasan Observatory, it was planned to observe Earth satellites for the study of physical conditions of the upper atmosphere. So, we started at once to construct Schmidt cameras. In spring 1956 a 16 cm F 1.5 camera was built, and in September 1957 a 40 cm F 1.5 camera was completed. On October 4, the U.S.S.R. announced from Moscow the

* Kwasan Observatory, Kyoto University.

launching of the first Earth satellite (1957 α). We immediately began to observe the satellite by the two Schmidt cameras. The first photographs were obtained on the morning of October 16. At about a month after the launching of the first, the news of the launching of the second Earth satellite (1957 β) was received. At that time, the Baker Schmidt camera had not arrived yet at Tokyo Observatory. As a Schmidt camera of medium size in Japan, our 40 cm camera was the only available one.

In this paper we deal with 1957 β only. According to the preliminary reports from Moscow, it was launched on the morning of November 3, weighing 508.3 kg, moving in an elliptic orbit with its maximum altitude of 17000 km, and taking about 103.7 minutes to complete one revolution. It was also reported that the satellite was travelling in an orbit inclined at about 65° to the equatorial plane.

At Kwasan, the observations of 1957 β were carried out from November 6, 1957 to March 21, 1958. The Moon Watch teams in Western Japan — Shizuoka, Yokkaichi, Kashiwara, Osaka, Kanaya, Tadotsu, Kochi, Hiroshima and Miyazaki (including photographs) — also reported their observational data to us. By adding these to ours, the orbital elements of the satellite and their variations have been determined. Using these values, we have derived an empirical formula between the retrograde rate of orbit and the period, and have finally estimated the air density at perigee altitudes.

2. Observations

a) *Instruments*

The observational material mainly consists of a group of Kwasan 40 cm F 1.5 Schmidt (film diameter 10 cm, field 8°, designed by Y. Nakai) and 16 cm F 1.5 Schmidt (film diameter 6 cm, field 15°) photographs taken by Y. Nakai, S. Saito and the present authors and of a number of photographs obtained by the present authors with a Nikon S II camera (F 1.2). We used the exposure time of 2~10 seconds. Fuji SSS film and Fuji X-Ray film for fluorography were used. All films were developed with Rendol at 20°C (3 minutes for SSS, 6 minutes for X-Ray film).

In order to record the time at which the shutters were opened and closed, three methods were adopted; 1. synchronized recording of shutter signals and J.J.Y. signals from radio into pen-oscillograph, 2. synchronized recording of the two signals into tape-recorder, 3. eye and ear methods with a chronometer. The instruments we have made use of are illustrated in Figs. 1 a, 1 b and 1 c. Moon Watch teams used Astro and Nikko Satellite telescopes (field 7°). Time recordings were made by using tape-recorder and J.J.Y. signals. Miyazaki Team took also many photographs.

Fig. 1 a. 40 cm Schmidt camera.

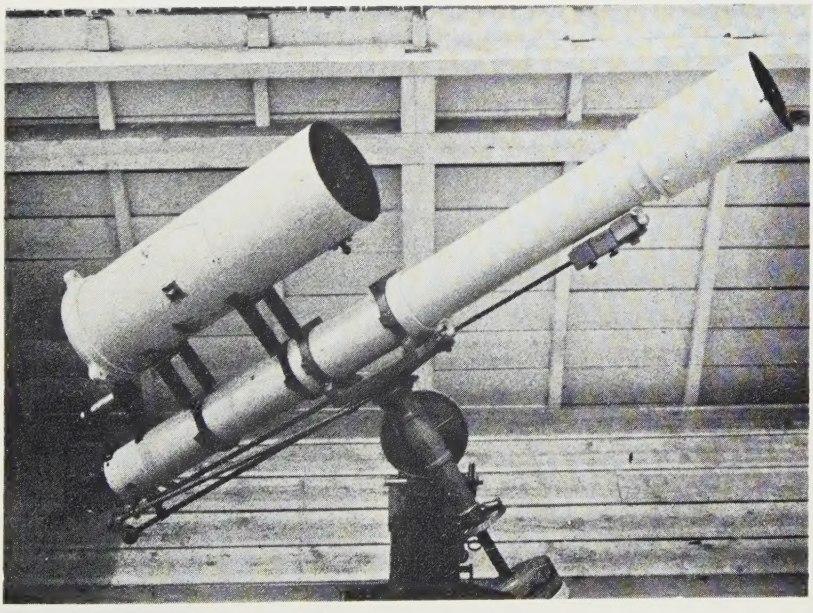

Fig. 1 b. 16 cm Schmidt camera.

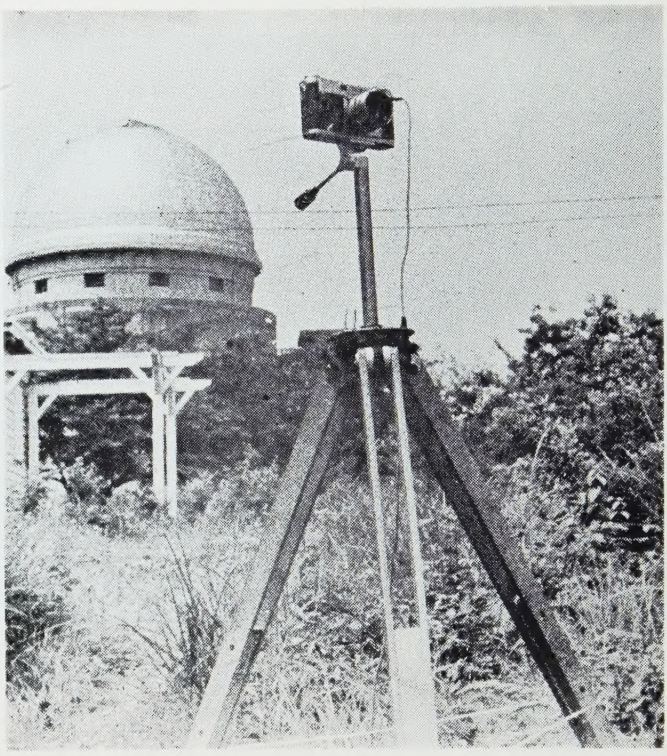

Fig. Ic. Nikon S II camera.

b) *Data*

Observations of the satellite consist in measuring its position at a recorded time. As for the photographic observation, the time recorded is that of the opening or closing of the shutters. Fig. 2 shows an example of the photographic observation.

Table 1.

No.	Team	Longitude	Latitude	Altitude
1	Shizuoka	138°23′18″E	34°58′25″N	20 m
2	Yokkaichi	136 39 00	35 00 15	3
3	Kashiwara	135 48 15	34 30 24	66
4	Kwasan	135 47 33.66	34 59 55.46	221
5	Osaka	135 30 30	34 41 51	30
6	Kanaya	135 15 10	34 03 46	40
7	Tadotsu	133 45 16	34 16 20	2–5
8	Kochi	133 30 35	33 33 25	30
9	Hiroshima	132 28 10	34 22 08	3
10	Miyazaki	131 25 24	31 55 23	8

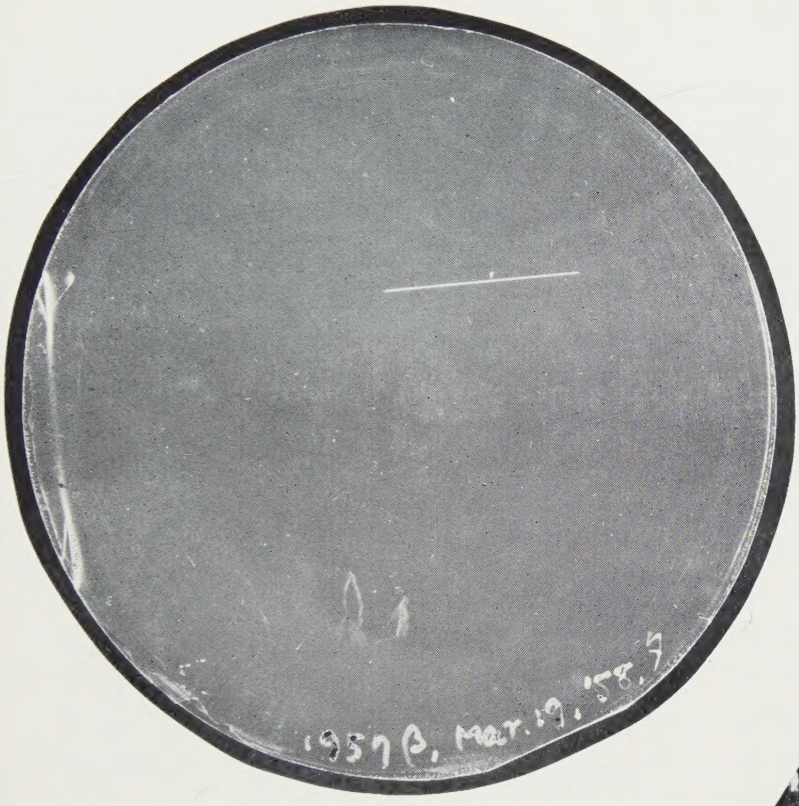

Fig. 2 a. A photograph taken by the 16 cm Schmidt camera: the left end of the trail corresponds to the current number 188 in Table 2, and the right end to 189.

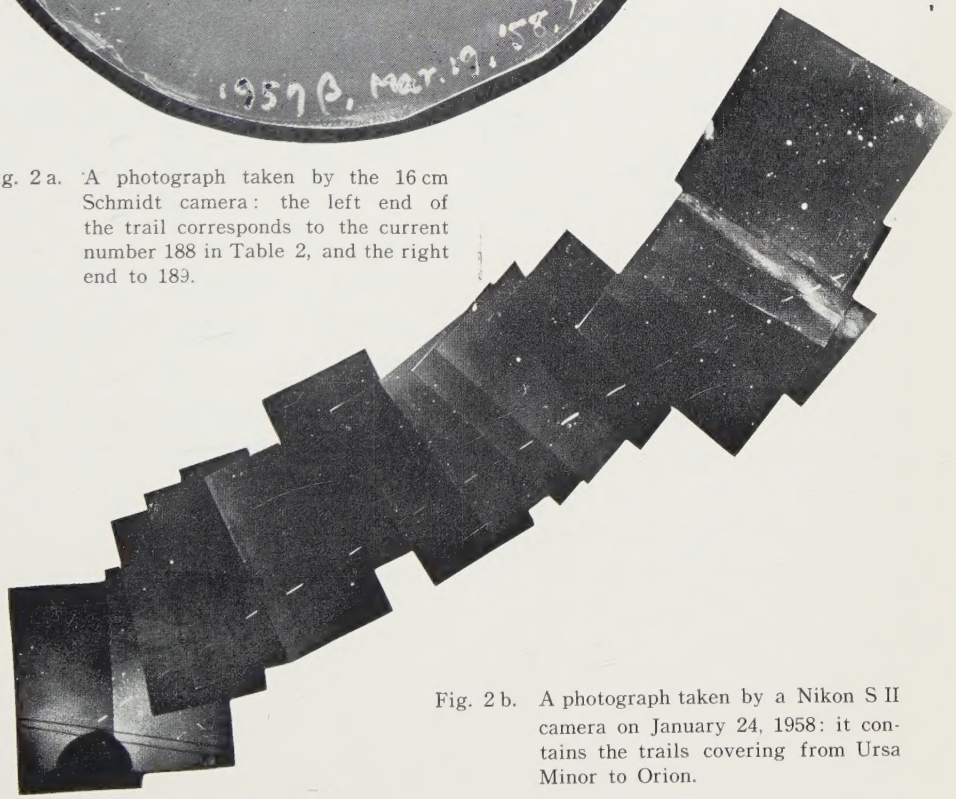

Fig. 2 b. A photograph taken by a Nikon S II camera on January 24, 1958: it contains the trails covering from Ursa Minor to Orion.

Table 2.

No.	Date	Team	Time	R.A.	Declination	Azimuth	Altitude	Remarks
			h m s	h m				
1	Nov. 6, '57	Kochi	5 8 16	8 2	−43°	S 0° 6′E	13°27′	V.
2		Shizuoka	5 9 25.5	6 50	−29	S21 44W	22 26	V.
3		Kwasan	~5 10 50.0	—	—	~E	—	P.*
4	Nov. 7, '57	Kwasan	5 21 20.2	5 21.8	+18.25	S80 13W	45 42	P.
5			21 39.00	5 18	+45.1	N59 29W	52 51	P.
6			21 43.32	5 17	+49.5	N52 14W	52 33	P.
7			21 46.75	5 16.3	+52.3	N47 42W	52 8	P.
8			21 50.12	5 15	+57.3	N39 51W	51 0	P.
9			22 24.68	19 30	+84.46	N 1 37E	29 38	P.
10			22 28.48	18 41	+82.25	N 3 58E	28 2	P.
11			22 33.25	18 30	+79.58	N 5 43E	25 49	P.
12			22 37.83	18 18	+77.34	N 7 28E	24 7	P.
13			22 59.83	18 3	+68.7	N13 6E	17 11	P.
14			23 13.77	18 2	+66.0	N14 38E	14 55	P.
15			23 17.95	18 1	+65.2	N15 9E	14 17	P.
16		Shizuoka	5 21 33.0	4 2	+25	N79 15W	30 31	V.
17	Nov. 8, '57	Kanaya	5 33 27	—	—	N 5 W	8	V.
18		Hiroshima	5 33 39	19 45	+62	N 5 22E	6 48	V.
19	Dec. 9, '57	Shizuoka	5 18 5	17 55	+51.3	N38 12E	16 32	V.
20	Dec. 10, '57	Shizuoka	5 5 56	17 30	+50	N40 54E	17 58	V.
21	Dec. 12, '57	Kwasan	6 24 40	—	—	~N40 W	~40	P.§
22	Dec. 13, '57	Kanaya	6 11 3	10 35	+20	S48 25W	70 18	V.
23	Dec. 14, '57	Kanaya	5 55 58	10 35	+20	S42 5W	71 57	V.
24		Yokkaichi	5 55 59	10 8	+14	S47 7W	61 48	V.
25		Kochi	5 56 18	11 34	+15	S10 59E	71 9	V.

Table 2. (continued)

No.	Date	Team	Time	R.A.	Declination	Azimuth	Altitude	Remarks
			h m s	h m				
26	Dec. 15, '57	Kwasan	5 39 14.5	9 12	+33.°6	N84°14′W	64°34′	P.
27			39 19.5	9 19	+32.3	N88 1W	65 43	P.
28		Yokkaichi	5 40 19	10 4	+13	S 42 39W	62 6	V.
29	Dec. 16, '57	Kwasan	5 22 23	8 23	+43.4	N62 26W	58 19	P.
30			22 27	8 33	+42.1	N64 54W	60 10	P.
31			24 2	10 28	+10.8	S 20 55W	64 27	P.
32			24 6	10 33	+ 9.2	S 17 17W	63 14	P.
33		Kashiwara	5 23 18	9 51	+27	S 69 6W	72 46	V.
34		Kanaya	5 23 50	10 26	+20	S 31 40W	73 52	V.
35		Yokkaichi	5 23 56	10 8	+13	S 35 3W	64 15	V.
36		Miyazaki	5 25 34	12 56	− 3	S 47 2E	43 44	V.
37		Kochi	5 27 11	12 36	−24	S 25 21E	27 55	V.
38		Kanaya	5 27 37	12 18	−26	S 18 22E	27 31	V.
39	Dec. 17, '57	Kwasan	5 4 57	7 59	+48.8	N52 48W	56 3	P.
40			5 7	8 17	+47.0	N55 18W	59 16	P.
41			6 37	10 16	+16.8	S 25 12W	70 14	P.
42			6 46	10 23	+13.5	S 17 57W	67 37	P.
43	Dec. 18, '57	Miyazaki	4 50 42	12 45	− 1	S 53 0E	42 38	V.
44	Dec. 19, '57	Kwasan	4 33 43	11 43	−17.8	S 22 26E	34 5	P.
45			33 55	11 46	−19.8	S 22 23E	31 59	P.
46	Dec. 23, '57	Miyazaki	17 52 31	1 55	+29	N87 22E	61 53	V.
47		Hiroshima	17 52 38	23 49	−11	S 0 10W	44 38	V.
48		Shizuoka	17 53 7	19 47	+12.5	S 87 6W	26 15	V.
49		Yokkaichi	17 53 24	20 19	+39	N67 19W	45 8	V.
50		Osaka	17 53 49	23 59	+89	N 0 1W	35 42	V.

Table 2. (continued)

No.	Date	Team	Time	R.A.	Declination	Azimuth	Altitude	Remarks
			h m s	h m				
51	Dec. 24, '57	Kanaya	17 30 2	0 5	+18°	S 19°36′ E	73° 7′	V.
52		Kashiwara	17 30 59	6 10	+59	N34 43 E	26 1	V.
53	Jan. 23, '58	Kashiwara	19 17 3	18 40	+63	N20 18W	14 39	V.
54		Osaka	19 19 59	2 0	+64	N18 25W	57 34	V.
55			22 9	4 33	+16	S 39 23 E	67 0	V.
56		Kanaya	19 21 2	3 53	+46	N17 40 E	77 22	V.
57			21 59	4 40	+24	S 60 16 E	72 5	V.
58		Miyazaki	19 21 23	6 13	+45.0	N56 2 E	53 30	V.
59		Yokkaichi	19 22 41	4 34	+ 7	S 27 50 E	59 12	V.
60			22 45	4 35	+ 5	S 26 48 E	57 17	V.
61	Jan. 24, '58	Kwasan	18 24 18	15 50	+72	N 5 35W	17 42	P.
62			24 24	15 43	+73	N 4 47W	18 32	P.
63			24 44	15 31	+74.8	N 3 29W	20 7	P.
64			24 50	15 15	+76.4	N 2 9W	21 32	P.
65			25 1	14 29	+78.5	N 0 39 E	23 31	P.
66			25 10	14 5	+79.5	N 1 48 E	24 37	P.
67			25 27.5	12 43	+80.8	N 5 5 E	26 53	P.
68			25 33	12 15	+81.0	N 6 3 E	27 38	P.
69			25 51	10 13	+80.0	N10 43 E	30 39	P.
70			25 58	9 48	+79.5	N11 49 E	31 26	P.
71			26 12.5	8 49	+77.0	N15 40 E	33 36	P.
72			26 19.5	8 28	+75.4	N17 48 E	34 36	P.
73			26 39	7 47	+70.5	N24 3 E	37 19	P.
74			26 44	7 38	+69.8	N24 55 E	38 6	P.
75			27 6.5	7 13	+62.2	N34 42 E	40 49	P.

Table 2. (continued)

No.	Date	Team	Time	R.A.	Declination	Azimuth	Altitude	Remarks
			h m s	h m				
76	Jan. 24, '58	Kwasan	18 27 11.5	7 8	+60.°6	N36°49′E	41°27′	P.
77			27 25	7 0	+56.3	N42 37E	42 29	P.
78			27 30	6 57	+54.3	N45 21E	42 50	P.
79			27 48	6 47	+48.8	N53 5E	44 0	P.
80			27 53	6 46	+47.2	N55 19E	44 0	P.
81			28 4.5	6 44	+43.2	N60 53E	43 44	P.
82			28 9.5	6 42	+41.0	N63 58E	43 40	P.
83			28 22.5	6 39	+37.2	N69 15E	43 19	P.
84			28 30	6 37	+34.0	N73 37E	42 47	P.
85			28 49	6 33	+28.6	N80 53E	41 45	P.
86			28 58	6 33	+25.6	N84 32E	40 32	P.
87			29 5	6 32	+23.6	N87 3E	39 53	P.
88			29 14	6 32	+21.2	N89 48E	38 49	P.
89			29 20	6 31	+20.1	S88 48E	38 30	P.
90			29 14	6 31	+21.2	N89 57E	39 1	P.
91			29 20	6 30.5	+20.0	S88 37E	38 33	P.
92			29 43	6 29	+13.7	S81 35E	35 38	P.
93			29 48	6 28	+12.3	S79 59E	35 6	P.
94			29 59	6 28	+10.4	S78 3E	34 2	P.
95			30 3	6 27	+ 9.8	S77 17E	33 54	P.
96			30 10	6 27	+ 7.5	S75 3E	32 33	P.
97			30 17	6 27	+ 5.8	S73 26E	31 33	P.
98		Shizuoka	18 26 2	2 49	+85	N 0 6W	39 59	V.
99		Miyazaki	18 26 33	8 55	+64.6	N28 6E	25 29	V.
100			27 17.0	8 21.4	+53.3	N41 32E	25 42	V.

Table 2. (continued)

No.	Date	Team	Time	R.A.	Decli-nation	Azimuth	Altitude	Remarks
			h m s	h m				
101	Jan. 24, '58	Miyazaki	18 28 49.8	7 32	+32.°2	N67°12′E	26°58′	V.
102		Osaka	18 28 7	6 46	+43	N60 45E	43 0	V.
103			32 24	6 28	−13	S57 55E	19 14	V.
104		Yokkaichi	18 28 13	6 36	+44	N60 16E	45 56	V.
105		Kanaya	18 28 43	6 52	+34	N71 21E	39 11	V.
106		Miyazaki	20 8 45.5	0 7.6	+27.6	N78 19W	38 25	V.
107			9 20.4	0 36.6	+20.8	N89 46W	41 48	V.
108			9 25.9	0 44	+19.2	S87 18W	42 40	V.
109			9 48.0	1 1	+14.6	S79 8W	43 59	V.
110			10 29.0	1 37.5	+ 5.5	S61 23W	45 49	V.
111		Kashiwara	20 8 49	23 59	+12	S86 51W	26 2	V.
112	Jan. 25, '58	Kwasan	19 14 49	0 36	+33	N79 59W	53 11	P.
113			14 58.5	0 43	+31.7	N82 46W	54 13	P.
114			15 4.5	0 50	+30	N86 22W	55 4	P.
115			15 8.5	0 54	+28.4	N89 31W	55 20	P.
116			15 4.5	0 49	+30.1	N86 5W	54 54	P.
117			15 8.5	0 54	+29.1	N88 22W	55 34	P.
118			16 23	2 13.5	+ 7.3	S39 22W	56 23	P.
119			16 27.5	2 17.5	+ 6.0	S36 40W	55 45	P.
120			16 36.5	2 25	+ 3.8	S32 3W	54 39	P.
121			16 42	2 28	+ 2.5	S29 58W	53 47	P.
122			16 47	2 36	− 0.5	S25 4W	51 46	P.
123			16 57	2 40	− 1.5	S23 6W	51 9	P.
124		Kashiwara	19 15 4	24 48	+32	N82 6W	55 13	V.
125			16 54	2 35	+ 1	S26 41W	53 30	V.

Table 2. (continued)

No.	Date	Team	Time	R.A.	Declination	Azimuth	Altitude	Remarks
			h m s	h m				
126	Jan. 25, '58	Kashiwara	19 18 57	3 43	−23°	S 1°4′ E	32°30′	V.
127		Kanaya	19 15 11	0 56	+34	N78 49W	57 40	V.
128			15 57	1 52	+19	S62 51W	62 49	V.
129			16 55	2 40	+ 3	S25 19W	56 25	V.
130			18 8	3 32	−15	S 1 17W	40 55	V.
131			19 9	3 59	−24	S 5 54E	31 42	V.
132			20 25	4 30	−32.5	S11 45E	22 20	V.
133		Hiroshima	19 16 30	3 24	+ 9	S 0 25E	64 38	V.
134		Miyazaki	19 17 39.6	4 26	+ 1.3	S30 8E	55 40	V.
135			17 57.6	4 33	− 3.4	S29 21E	49 48	V.
136			19 39.9	5 4.4	−22.1	S27 41E	30 42	V.
137		Tadotsu	19 17 43	3 43	−10	S 4 43E	45 37	V.
138		Yokkaichi	19 18 39	3 29	−22	S 3 38W	32 55	V.
139	Jan. 27, '58	Miyazaki	19 4 23.0	22 28	+49.8	N48 34W	35 10	V.
140			4 27.9	22 36	+49.3	N49 26W	36 21	P.
141			5 6.5	23 30	+44.1	N57 32W	44 52	P.?
142			5 38.9	0 12	+37.6	N68 18W	52 9	P.?
143			6 3.5	0 42	+31.9	N79 33W	57 24	P.
144			6 8.0	0 47	+30.5	N82 31W	58 9	P.
145			8 30.1	2 48.2	− 9.9	S11 15W	47 32	V.
146			9 2.0	3 7	−16.3	S 4 1W	41 41	V.
147		Kanaya	19 4 35	22 8	+32	N66 38W	24 19	V.
148			4 38	22 52	+30	N73 12W	32 1	V.
149			5 4	23 8	+28	N77 1W	34 20	V.
150			5 32	23 36	+23	N85 53W	37 50	V.

Table 2. (continued)

No.	Date	Team	Time	R.A.	Declination	Azimuth	Altitude	Remarks
			h m s	h m				
151	Jan. 27, '58	Kanaya	19 6 14	0 15	+14°	S 78°8′W	41°19′	V.
152			7 13	1 46	−13	S 33 2W	36 30	V.
153		Yokkaichi	19 6 43	0 33	+ 4	S 64 51W	37 13	V.
154		Tadotsu	19 5 8	23 30	+28	N 79 30W	40 2	V.
155	Jan. 28, '58	Kobe	~18 9 25	—	—	-	~90	V.&
156	Jan. 30, '58	Yokkaichi	17 54 12	0 3	+27	S 87 7W	56 13	V.
157		Osaka	17 54 18	—	—			V.
158	Mar. 13, '58	Kashiwara	5 26 19	23 44	+60	N 31 54E	23 10	V.
159			29 53	21 38	+ 8	S 86 0E	19 57	V.
160	Mar. 14, '58	Miyazaki	5 18 30	22 27	+32	N 62 10E	16 26	V.?
161	Mar. 15, '58	Kanaya	5 3 10	21 30	+37	N 63 46E	30 54	V.?
162	Mar. 16, '58	Kanaya	4 50 41	21 6	+16	N 86 50E	24 42	V.
163	Mar. 17, '58	Kanaya	4 31 25	21 45	+49	N 47 58E	28 30	V.
164		Kashiwara	4 32 51	20 55	+25	N 78 0E	28 58	V.
165	Mar. 18, '58	Miyazaki	19 33 21	5 45	− 3	S 30 52W	50 42	V.
166			33 31.6	6 0.6	+ 5.8	S 31 37W	60 18	V.
167	Mar. 19, '58	Kwasan	3 52 41.4	21 12.40	+44.18	N 53 43E	27 55	P.
168			52 46.4	21 9.20	+43.20	N 55 0E	28 5	P.
169			54 17.4	20 31.25	+18.30	N 84 3E	24 21	P.
170			54 24.4	20 29.20	+16.40	N 86 7E	23 49	P.
171		Miyazaki	5 28 48	12 51	+46	N 54 29W	41 15	V.
172			28 54	12 58	+45.5	N 55 19W	42 24	P.
173			28 58.9	13 7	+44.1	N 57 25W	43 51	P.
174			30 34.1	15 24	+13.7	S 55 46W	61 30	P.?
175			31 58.4	16 39	−13.6	S 7 33W	44 10	P.?

Table 2. (continued)

No.	Date	Team	Time	R.A.	Declination	Azimuth	Altitude	Remarks
			h m s	h m				
176	Mar. 19, '58	Miyazaki	5 32 6.8	16 47.5	−16.°7	S 4°25′W	41°16′	P.?
177			32 11.7	16 51	−17.9	S 3 15W	40 15	P.
178			32 17.1	16 54	−19.2	S 2 17W	38 51	P.?
179		Kanaya	5 29 34	13 25	+17	S 86 38W	36 18	V.
180		Miyazaki	19 11 28.3	6 0	−26	S 11 18W	31 11	P.
181			12 5.6	7 31.2	+10.8	S 30 7E	66 11	V.
182			13 1	11 52.1	+55.3	N 41 22E	32 59	P.
183		Kochi	19 12 48	6 48	+34	N 65 3W	88 56	V.
184		Tadotsu	19 12 50	6 30	+16.5	S 18 6W	71 27	V.
185		Kashiwara	19 12 55	4 23	+15.4	S 71 58W	49 36	V.
186			13 17	4 45	+47	N 53 36W	61 27	V.
187		Yokkaichi	19 13 2	4 0	+12.0	S 72 58W	42 14	V.
188		Kwasan	19 13 9.5	4 47.5	+24.8	S 79 53W	59 16	P.
189			13 11.5	4 51.0	+28.9	S 86 50W	61 39	P.
190			13 23	5 0	+45	N 57 24W	64 43	V.
191		Osaka	19 13 17	5 14	+47	N 50 21W	66 28	V.
192		Shizuoka	19 14 46	19 16	+76	N 0 7W	20 58	V.
193	Mar. 20, '58	Miyazaki	5 3 57.5	9 8	+56	N 32 23W	14 59	V.?
194			5 31	11 0	+57.3	N 38 2W	29 11	V.
195			5 57.8	11 46.4	+55.4	N 41 37W	35 5	V.
196			6 14.8	12 15	+54.4	N 43 16W	39 4	P.
197			6 22.3	12 30	+53.4	N 44 38W	41 14	P.
198			6 47.5	13 20	+48.9	N 50 26W	49 13	P.?
199			7 11	14 7	+42.7	N 59 17W	57 59	P.?
200			7 22	14 21	+39.6	N 64 52W	60 53	P.

Table 2. (continued)

No.	Date	Team	Time	R.A.	Declination	Azimuth	Altitude	Remarks
			h m s	h m				
201	Mar. 20, '58	Miyazaki	5 7 25.4	14 26	+38.°5	N67°1′W	61°54′	P.
202			7 36	14 45	+33.9	N77 27W	65 42	P.
203			7 39.7	14 51	+32.5	N81 11W	66 50	P.
204			7 49	15 4	+28.9	S88 6W	68 55	P.?
205			8 19.6	15 43.9	+15.6	S42 5W	69 4	V.
206			8 57.4	16 22	+ 0.1	S 9 28W	57 49	P.?
207			9 10.2	16 32.5	− 4.4	S 4 7W	53 36	P.
208			9 13.5	16 35	− 5.7	S 3 0W	52 20	P.
209			9 26.4	16 46	− 9.9	S 1 16E	48 10	P.?
210			9 29.5	16 46.6	−10.7	S 1 26E	47 22	V.
211			9 52.6	17 3	−17.1	S 6 18E	40 45	P.?
212			10 4	17 9	−19.5	S 7 45E	38 13	P.
213			10 8	17 12	−20.3	S 8 29E	37 20	P.
214			10 51.1	17 32.5	−27.7	S12 19E	29 16	P.?
215		Kochi	5 7 36	14 11	+19	S77 38W	51 59	V.
216		Kanaya	18 49 5	5 35	− 9	S22 38W	44 17	V.
217			50 15	11 0	+65	N30 28E	41 4	V.
218		Kashiwara	18 49 14	5 22	−12	S25 50W	39 45	V.
219			49 26	5 44	+ 7	S29 24W	59 23	V.
220			50 25	11 5	+67.83	N26 58E	40 51	V.
221			50 52	13 18	+64.5	N28 42E	27 30	V.
222		Osaka	18 49 38	6 35	+16	S 4 46W	71 15	V.
223		Shizuoka	18 49 53	3 45	+23.7	S87 35W	47 53	V.
224			50 49	0	+88.7	N 1 32W	34 40	V.
225		Kwasan	18 49 54.3	7 10.6	+33.4	S76 27E	84 2	P.

Table 2. (continued)

No.	Date	Team	Time	R.A.	Declination	Azimuth	Altitude	Remarks
			h m s	h m				
226	Mar. 20, '58	Kwasan	18 49 56.3	7 17.7	+36.°05	N79 3′E	82°50′	P.
227			50 16.2	9 17.64	+57.66	N36 26E	55 47	P.
228			50 24.1	10 14.68	+62.32	N33 16E	47 32	P.
229			50 38.5	11 49	+64.22	N31 55E	36 54	P.
230			50 42.3	12 13.02	+63.9	N31 51E	34 16	P.
231			50 49.0	12 43.12	+63.71	N31 6E	31 1	P.
232		Yokkaichi	18 50 0	5 59	+46	N35 33W	75 50	V.
233			50 58	12 32	+71	N23 5E	34 4	V.
234	Mar. 21, '58	Kanaya	4 43 24	13 55	+19	S77 32W	51 20	V.
235			45 33	16 1	−21	S10 26W	34 15	V.

P.: photographic
*: no field star because of cloudy
&: observed at Kobe
V.: visual
§: no trail because of sky fog
?: reported as uncertain.

The position is given by the right ascension (R.A.) and by the declination of the satellite referred to field stars. The Skalnate Pleso Atlas was used for reference. The Moon Watch teams reported also the observational time and the position at which a good observation was carried out. Table 1 gives the data for the observing teams; the first column gives the current number, the second the place of the observing team, the third the longitude, the fourth the latitude, and the fifth the altitude. The observational data are compiled in Table 2; the first column gives the current number, the second the observational date, the third the observing team, the fourth the observation time, the fifth the right ascension, the sixth the declination, the seventh and the eighth the azimuth and the altitude converted from the right ascension and the declination respectively, and the ninth gives remarks. Hereafter time is referred to the Japanese Standard Time.

II. ORBIT

In this part, we shall describe the method of determining the orbital elements of 1957 β and find them by using the observational data obtained in the Western Japanese territories. According to the Russian communication the orbit of 1957 β is nearly circular, and we can observe only a small part of its orbit on any day. With

further allowance for the observational errors, it is difficult and rather disadvantageous to apply straightforwardly the usual orbital theory to the determination of the orbit of 1957 β. Therefore, we have confined ourselves to the favourable opportunities for us to determine the orbital elements and have treated the subject *graphically*.

3. Basic relations

Under the inverse-square law in the central-force field of the Earth's gravitation, the orbit of satellite is given by the well-known equation for an ellipse:

$$r = p(1+\varepsilon\cos v)^{-1}, \quad \text{with} \quad p = a(1-\varepsilon^2), \quad r = R_\phi + H, \tag{1}$$

where r is the radius vector from the Earth's center to the satellite, a the semi-major axis, ε the eccentricity, v the true anomaly, R_ϕ the radius of the Earth at the latitude ϕ, and H is the height of the satellite above the sea level. r/a is illustrated in Fig. 3, taking ε as a parameter.

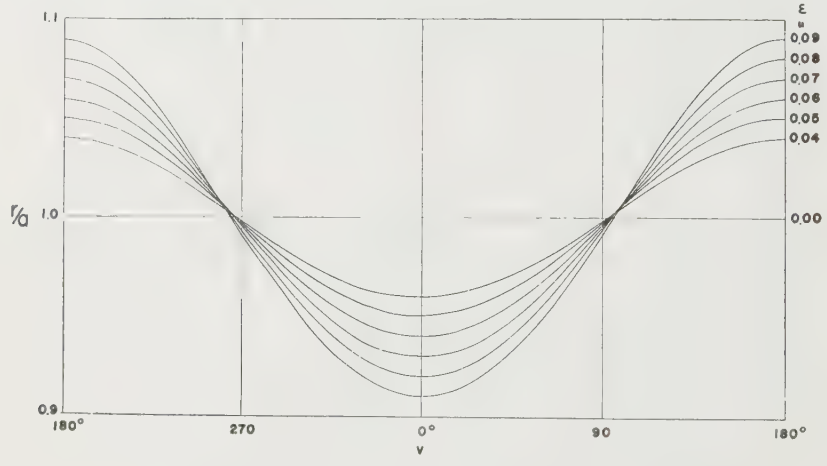

Fig. 3. The behavior of r/v *versus* v, taking ε as a parameter.

It is useful also to give the Keplerian expressions for the period T and for the orbital velocity V of an elliptical orbit;

$$\left.\begin{aligned} T &= 2\pi(GM)^{-1/2}a^{3/2}, \\ V &= (GM)^{1/2}\left(\frac{2}{r}-\frac{1}{a}\right)^{1/2}, \end{aligned}\right\} \tag{2}$$

where G is the gravitational constant and M is the mass of the Earth. R_ϕ decreases by several kilometers from 30°N to 40°N. In Fig. 4 are shown the relations (2), taking H above the 35°N sea level as a parameter.

Let h be the observed altitude of the satellite and θ the angle with which the

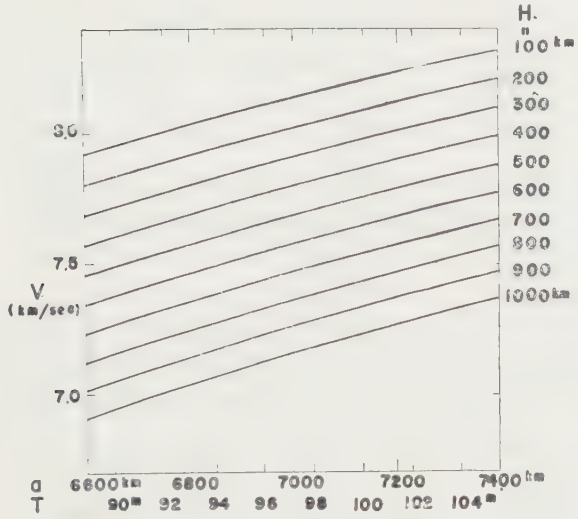

Fig. 4. The behavior of V *versus* a or T, taking H above the 35°N sea level as a parameter.

observer and the satellite subtend at the Earth's center. Then h is safely connected with θ and H by the relation:

$$\tan h = \cot\theta - \frac{R\phi}{r}\operatorname{cosec}\theta\,, \quad (3)$$

in which it is assumed that the altitude of the observatory is not too high and that the latitude of the observed point of the satellite is not too different from that of the observatory. The relation (3) is illustrated in Fig. 5, taking H above the 35°N sea level as a parameter.

Lastly it is convenient to

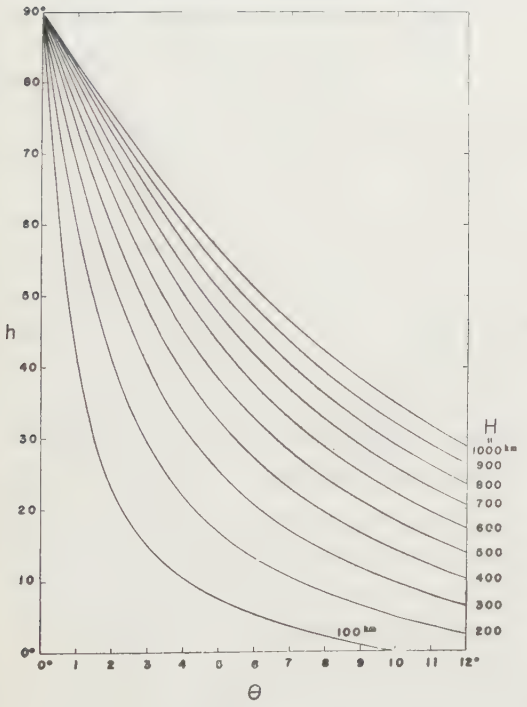

Fig. 5. The behavior of h *versus* θ, taking H above the 35°N sea level as a parameter.

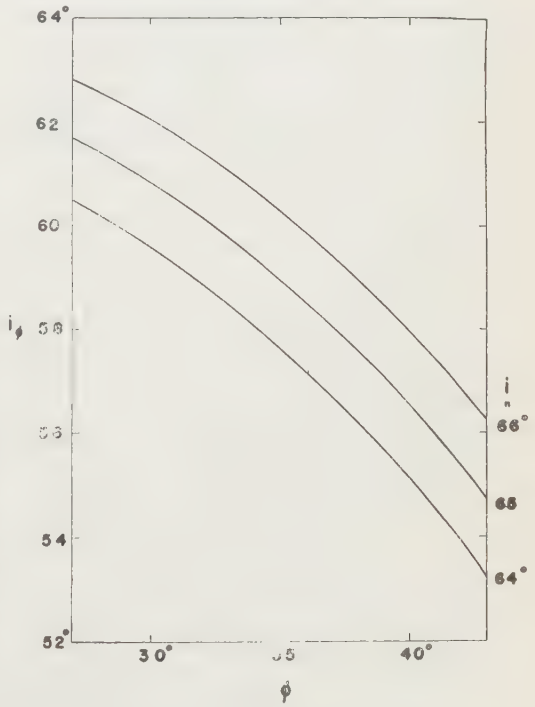

Fig. 6. The behavior of i_ϕ *versus* ϕ, taking i as a parameter.

have the inclination i_ϕ of the orbit projected on the surface of the Earth to any latitude line. Let i be the inclination of the orbit to the equatorial plane, then i_ϕ is given by

$$\cos i_\phi = \cos i \sec \phi\,, \quad |\phi| \leqslant i\,. \tag{4}$$

The relation (4) is shown in Fig. 6, taking i as a parameter. Corresponding to $i=64°$, 65° and 66°, we have prepared three curved measures drawn on a transparent celluloid sheet so as to fit the scale of the chart (**1**).

4. Determination of height

As is seen from the relation (3), the observed altitude is a function of θ and H. In other words, we cannot plot the observational data on the chart without knowing H. Moreover, (1) and (2) show that H is a fundamental quantity which determines the orbital elements. Then we shall take a glance at methods of fixing H.

a) It is obvious that the trigonometric survey is the most useful and precise method of determining H.

b) The orbital velocity of the satellite is connected with H by the relation (2). We may find out H from pass length of the satellite orbit projected on the chart, taking H as a parameter. H is, of course, variable when the time interval of the observations is too long, whereas change of the pass length due to that of H is negligible for $\Delta v \leqslant 5°$ for 1957 β with $\varepsilon \leqslant 0.1$. Namely, the pass length on the chart is approximated by R_ϕ/r times that in space. It is to be noted, however, that this method of determining H is such as to estimate the mean height over the time interval of observations.

c) We may employ a new trial of determining H from the observations at only *one* place in the absence of trigonometric survey. By means of the one place observations of the successive crossings of the east-west line for three days, we can simultaneously fix the mean height for three days at that latitude and $\Delta\Omega$, the retrograde rate of orbit per day. Let t_i and λ_i be the time and the longitude of the crossing of the east-west line for the i-th day, respectively. Then t_i and λ_i are connected with those in the following day by the relation:

$$\lambda_{i+1} - \lambda_i = (t_i - t_{i+1}) - \left(1 - \frac{t_i - t_{i+1}}{\text{one day}}\right)(\Delta\Omega + \Delta\Phi)\,, \tag{5}$$

where $\Delta\Phi$ is the rate of revolution of the Earth around the Sun per day and is put nearly as 0.°986. Using the relation (5) we derive for λ_2 and λ_3

$$\left.\begin{aligned} \lambda_2 &= \lambda_1 - \left(1 - \frac{t_1 - t_2}{1440}\right)\Delta\Omega + \frac{1}{4}(t_1 - t_2) - \left(1 - \frac{t_1 - t_2}{1440}\right)\Delta\Phi\,, \\ \lambda_3 &= \lambda_1 - \left(2 - \frac{t_1 - t_3}{1440}\right)\Delta\Omega + \frac{1}{4}(t_1 - t_3) - \left(2 - \frac{t_1 - t_3}{1440}\right)\Delta\Phi\,, \end{aligned}\right\} \tag{6}$$

where $t_i - t_j$ is expressed in minutes of time, each term in degrees of arc, and $\Delta\Omega$ is assumed not to change during those days.

Now, we shall apply the relations (6) to the evening observations on March 18, 19 and 20 in 1958. Of course, the crossing longitudes λ_i's depend apparently on H. Using each observational time and λ_1 which depends on H, we shall compute λ_i $(i=2, 3)$ from (6) taking $\Delta\Omega$ as a parameter, and shall plot λ_i in Fig. 7. On the other hand, we know λ_i $(i=2, 3)$ from the observations as the function of H, and plot λ_i in Fig. 7. Then, we can uniquely fix $H=255$ km and $\Delta\Omega=3.°18$, assuming that H has not changed during three days. The observation on March 18 was considerably apart from our east-west line, and so we are obliged to extrapolate its data to this line (see §5). Hence the values of H and $\Delta\Omega$ fixed above might be somewhat incorrect.

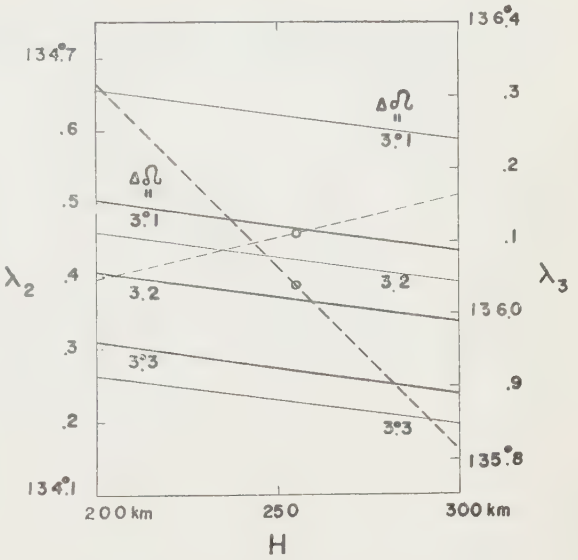

Fig. 7. The computed behaviors of λ_2 and λ_3 *versus* H taking $\Delta\Omega$ as a parameter are expressed by the solid curves, and the observed ones for λ_2 and λ_3 *versus* H by the dashed. λ_2 in thick curve is read by the left-hand ordinate scale, and λ_3 in thin by the right-hand one.

The change of H per day might be of the order of several kilometers and that of $\Delta\Omega$ per day of the order of a few thousandths of degree for 1957 β. Therefore, in treating the subject, the said assumptions may be admissible particularly for the observations in the perigee regions, with allowance for the observational errors. If we are able to have successive observations day by day, we may find the daily changes for H and $\Delta\Omega$. The present method is, however, not so effective with the exception of such a case that the observing place lies between the successive crossings.

5. Period and retrograde rate of orbit

If we can observe the times of the successive crossings of the east-west line of the observing place, we can find the period in which the satellite revolves around the Earth. It is, however, of rare occurrence to observe the successive passages within a day. Moreover, we have not always the east-west line observations. Therefore it

is necessary to extrapolate the observed points to one latitude line. We shall fix that line to the 35°N one passing near Kwasan Observatory. After finding H by means of such methods in the preceding section, we can plot the observed points on the chart using the data given in Table 2. When the observed point is apart from the 35°N line, it is extrapolated to that line along the curved measure mentioned in § 3. The observed point for the extrapolation should be such as more close to the 35°N line and more precise in observations. Until the inclination i is determined, it is assumed as 65° according to the Russian announcement. Then, we can find the time and the longitude at which the satellite crosses the 35°N line. Of course, the rotation of the Earth for the time interval between the two successive observations must be taken into account. From the successive crossings for two days, the mean period over about one day, T_ϕ, may be obtained in general by the following relation:

$$1440 = NT_\phi + \tau\,, \quad T_\phi > \tau\,, \tag{7}$$

where τ is the time in minutes by which N revolutions fall short of one day. $\Delta\Omega$, the retrograde rate of orbit per day, is directly obtained from the relation (5).

In Table 3 are listed the several quantities reduced as above with exception of those obtained from observations unfavourable for reductions. The first column in Table 3 gives the date of observation, the second the mean height for the two or three days, the third the crossing time, the fourth the crossing longitude, each on the 35°N line, the fifth the date on which the mean period is fixed, the sixth the mean period over about one day, and the seventh the retrograde rate of orbit per day. The explanation as to the figure in the bracket in the sixth column will be postponed to § 9. The errors estimated are such as incurred through the uncertainty of H and partly through those of the observation time, the inclination, the operations of plotting the observational data and of extrapolating to the 35°N line, and so on.

6. Eccentricity

The orbit of 1957 β is nearly circular and we can observe only a small part of its orbit within one day. Practically we had not so precise observation of heights as to determine the orbital elements, only by the Western Japanese territory observations for one day. However, it we have successive observations evening after morning or morning after evening, we can determine the eccentricity of the orbit, provided that the orbital elements do not change for those intervals. For we can observe considerably separate parts of the orbit on the morning and on the evening. We had such a case on March observations.

Now we shall determine the eccentricity on March 20.000 by using the observational data on March 19 evening and on March 20 morning. Let the quantities of

Table 3.

Date	35° N			Date	T_ϕ (T)	$\Delta\Omega$
	H	t	λ			
		h m				
Nov. 6, '57		5 10.841	138.°97			
		m ±0.100	±0.°04			
					m	
	295 km			Nov. 6.720	103.610	2.°19
	±20 km				m ±0.009	0.°26
					m (103.600)	
Nov. 7, '57		5 21.383	133. 13			
		±0.020	±0. 19			
Dec. 15, '57		5 39.357	132. 06			
		±0.010	±0. 09			
				Dec. 15.730	101.688	2. 68
					±0.003	0. 19
					(101.679)	
Dec. 16, '57	870	5 22.992	132. 53			
	±20	±0.025	±0. 09			
				Dec. 16.718	101.635	2. 68
					0.004	±0. 18
					(101.626)	
Dec. 17, '57		5 5.879	133. 19			
		0.030	±0. 08			
Dec. 23, '57		17 53.181	134. 20			
		±0.012	±0. 12			
	212			Dec. 24.237	101.232	2. 57
	±5				±0.002	±0. 16
					(101.223)	
Dec. 24, '57		17 30.433	136. 38			
		±0.013	±0. 03			

Table 3. (continued)

Date	35° N			Date	T_ϕ (T)	$\Delta\Omega$
	H	t	λ			
		h m				
Jan. 23, '58		19 21.233	136.°21			
		m				
		±0.020	±0.°05			
					m	
				Jan. 24.288	99.144	2.°79
					m	
					±0.002	±0.°26
					m	
					(99.135)	
Jan. 24, '58	895 km	18 29.245	145. 57			
	±20 km	±0.010	±0. 20			
				Jan. 25.286	99.063	2. 84
					±0.002	±0. 33
					(99.054)	
Jan. 25, '58		19 15.185	130. 13			
		±0.010	±0. 13			
Mar. 18, '58		19 34.673	133. 13			
		±0.017	±0. 03			
				Mar. 19.308	94.569	3. 18
					±0.002	±0. 08
					(94.561)	
Mar. 19, '58	254	19 13.212	134. 39			
	±5	±0.010	±0. 05			
				Mar. 20.293	94.447	3. 19
					±0.001	±0. 08
					(94.439)	
Mar. 20, '58		18 49.922	136. 11			
		±0.010	±0. 03			
Mar. 19, '58		5 29.010	125. 73			
		±0.039	±0. 10			
				Mar. 19.721	94.520	
					±0.004	
					(94.512)	
Mar. 20, '58	715	5 6.812	127. 01			
	±20	±0.017	±0. 08			
				Mar. 20.705	94.399	
					±0.003	
					(94.391)	
Mar. 21, '58		4 42.790	128. 83			
		±0.021	±0. 16			

the former be denoted by suffix e and those of the latter by suffix m. From the data in Table 3 we may find for the difference of the true anomalies $v_m - v_e$ between the 19 evening and the 20 morning, in an approximation of no motion of the perigee along the orbit:

$$\left.\begin{aligned} \cos(v_m - v_e) &= 1 - \cos^2 35^\circ + \cos^2 35^\circ \cos\Theta\,, \\ \text{then} \qquad & \\ v_m - v_e &= 101.^\circ 83\,, \end{aligned}\right\} \tag{8}$$

where

$$\Theta = \left(1 - \frac{t_e - t_m}{\text{one day}}\right)(360^\circ + \Delta\Omega + \Delta\Phi) - (\lambda_e - \lambda_m) = 142.^\circ 74\,,$$

with

$$\Delta\Omega = 3.^\circ 18\,.$$

On the other hand, we have $a = 6871$ km from the mean period $T \simeq T_\phi = 94.^m 485$ (see § 9), and have $r_e = 6625\,\text{km} \pm 5\,\text{km}$ and $r_m = 7086\,\text{km} \pm 20\,\text{km}$ corresponding to $H_e = 254\,\text{km} \pm 5\,\text{km}$ and $H_m = 715\,\text{km} \pm 20\,\text{km}$ respectively. Then we have

$$\left.\begin{aligned} r_e/a &= 0.9642 \pm 0.007\,, \\ r_m/a &= 1.0313 \pm 0.029\,. \end{aligned}\right\} \tag{9}$$

By applying (8) and (9) to Fig. 3, we find out graphically, for the mean eccentricity ε and also for v_e:

$$\varepsilon\ (\text{Mar. } 20.000) = 0.043 \pm 0.0020\,, \tag{10}$$

and

$$v_e\ (\text{Mar. } 20.000) = 35.^\circ \pm 4.^\circ 0\,. \tag{11}$$

The latitude of the perigee on those days may be found about 3°N with the value (11) and that of the apogee about 3°S, by assuming the inclination i as 65°. Then, we can obtain, by (10), for the heights of the perigee and the apogee:

$$\left.\begin{aligned} H_P\ (\text{Mar. } 20.000) &= 195\,\text{km} \pm 14\,\text{km}\,, \\ H_A\ (\text{Mar. } 20.000) &= 791\,\text{km} \pm 14\,\text{km}\,, \end{aligned}\right\} \tag{12}$$

where the suffixes P and A are referred to the perigee and the apogee, respectively.

7. Inclination

From the analysis in the preceding section we have found the dimensions and the direction of the orbit with respect to the Earth from March 19 to 20. Therefore we can compute the heights of 1957 β at every latitude of the Earth, assuming at first that the inclination i is equal to 65°. In fact, the heights computed above are seen hardly dependent on i as long as the uncertainty for i is of the order of $\pm 1^\circ$. We shall apply these heights to the photographic and comparatively precise observations

on March 20 morning obtained by Miyazaki Team and find the height for every observation, which is listed in Table 4. The 1st column of Table 4 gives the current number in Table 2, the 2nd the latitude of the observed point which is estimated from the azimuth and from the first approximation height, and the 3rd the height computed corresponding to the 2nd column latitude. Using the heights ih Table 4 we can plot the observational data on the chart, of course, with allowance for the rotation of the earth corresponding to the observation times. This determines the orbit projected on the earth's surface. By making the curved measures quoted in §3 slide on this orbit we may find for the inclination

Table 4.

No.	ϕ	H
196	36.°7N	707 km
197	36. 3	709
200	33. 3	721
201	33. 1	722
202	32. 5	724
203	32. 3	725
305	30. 2	732
207	27. 6	741
208	27. 4	742

$$i = 65.°5 \pm 0.°2 . \tag{13}$$

Without all these valuable data which were put at our disposal by Miyazaki Team, it would have been impossible to make this determination.

8. Motion of the perigee along the orbit

It is known by the perturbation theory that the perigee is in motion along the orbit corresponding to the retrograde motion of the orbit. We shall seek for the rate of the perigee motion.

It is probable that the change of the perigee height with time is very slow compared to that of the apogee one, so we can say from the values in Table 3 and in (12) that we had the observation near the perigee regions on December 23 evening. Therefore, it may be permissible to extrapolate the height on December 23 to that on December 16. Namely, on December 16, 1957 β might have crossed with $H_e \simeq 232$ km or more* near evening while with $H_m = 870$ km $\pm$ 20 km on the morning. As we have, however, no informations on the time and the longitude of the evening crossing, we cannot evaluate $v_m - v_e$. Assuming a circular orbit with $i = 65.°5$ we shall estimate $v_m - v_e$ nearly as 102°. Then, following the procedure as in §6 we may find for ε and v_e:

$$\varepsilon \ (\sim \text{Dec. } 16) \simeq 0.088 , \tag{14}$$

and

$$v_e \ (\sim \text{Dec. } 16) \simeq 354° \ (= -6°) . \tag{15}$$

The latitude of the perigee may be found with (15) near 40°N and that of the apogee

* This will be justified in a later analysis.

near 40°S. Then we get, by (14), the heights of the perigee and the apogee as:

$$\left.\begin{aligned} H_P\ (\sim\text{Dec. } 16) &\simeq 210\,\text{km}\,, \\ H_A\ (\sim\text{Dec. } 16) &\simeq 1480\,\text{km}\,. \end{aligned}\right\} \tag{16}$$

In the first approximation of its linear motion, we may find, for the motion of the perigee along the orbit per day from Debember 16 to March 20,

$$\Delta\omega \simeq \frac{-6-35.8}{94} = -0.44 \text{ degrees per day}. \tag{17}$$

That is, the perigee might retrograde along the orbit at the mean rate of 0.44 degrees per day. When we extrapolate, with (17), linearly back to the launching days, we may guess that the latitude of the perigee for those days was near 55°N.

As will be shown later, the period and the retrograde motion of the orbit do not change linearly with respect to time. The retrograde motion of the orbit seems further to be in some relation to the period. The perigee motion is connected with the retrograde motion of the orbit, so the former must, in fact, have a dependency like that of the latter on the period.

Up to the preceding section we have neglected the perigee motion in describing the orbit. In the next section we shall briefly consider an influence of the present motion on the period and shall give the period in its true sense.

III. RESULTS

We shall derive some results from the orbital elements and their changes of 1957 β obtained in the preceding part.

9. Period in the true sense and its acceleration rate

Owing to the perigee motion along the orbit, the period in the true sense T is expected to be different from T_ϕ, the period between the successive crossings of 35°N line. T may be connected with T_ϕ by the relation:

$$T = T_\phi\left(1+\frac{\Delta\omega\, T_\phi}{360\times 1440}\right). \tag{18}$$

With (17), as for 1957 β, it is found that T is shorter by about $0.^{m}01$ than T_ϕ in the first appro ximation. The period in the true sense is bracketed in the sixth column of Table 3.

As a result of the transformation of T_ϕ into T, the semi-major axis introduced in §§ 6 and 8 should be made smaller by about 0.5 km and, consequently, the results in sections from 6 to 8 must suffer some changes. However these are included within the errors, so we shall leave the results as they were.

Next we shall estimate the acceleration rate of the period. The mean rate per day may be approximated by a rough formula:

$$\Delta T = \frac{\delta T}{\delta t}, \tag{19}$$

where δt means the difference of time in days on which T's are fixed, and δT the increment of the period for that interval. The data made use of for determining ΔT are listed in Table 5 with reference to Table 3. The first column of Table 5 gives the date on which T is fixed, the second the period, the third δT, the fourth δt, the fifth the mean date on which ΔT is determined, and the sixth the acceleration rate of the period per day obtained from (19).

Table 5.

Date	T	δT	δt	Date	ΔT
	m	m	d		m
Nov. 6.720	103.600	−1.830	37.032	Nov. 25.236	−0.0494
Dec. 13.752	101.770*	−0.144	2.966	Dec. 15.235	−0.0485
Dec. 16.718	101.626	−0.403	7.519	Dec. 20.478	−0.0536
Dec. 24.237	101.223	−2.088	31.051	Jan. 8.762	−0.0672
Jan. 24.288	99.135	−0.385	5.978	Jan. 27.313	−0.0644
Jan. 30.266	98.750*	−3.908	45.430	Feb. 21.981	−0.0860
Mar. 16.696	94.842*	−0.451	4.009	Mar. 18.701	−0.1124
Mar. 20.705	94.391				

* Less certain data which are not listed in Table 3.

The behaviors of T and ΔT with respect to date are illustrated in Fig. 8 with reference to Table 3 and to Table 5. The behavior of ΔT is very curious. The discussions on this erratic orbital acceleration were given partly by L. G. Jacchia (**2**). We shall, however, have no comment on this interesting subject only from our observations.

10. Dependency of the retrograde rate of orbit on the period

The retrograde motion of the orbit is due to the non-central field of terrestrial gravitation, so the retrograde rate is expected to depend on the mean height of the satellite. From Table 3 it is found that the retrograde per day tends to increase in fact with the period decreasing We shall now seek for an empirical formula between $\Delta\Omega$, the retrograde rate of the orbit per day, and the period in the true sense T.

In treating the subject we shall make use of a mean value of the retrograde motion, for its daily rate tabulated is considerably incorrect due to the uncertainty of the

crossing longitude. We shall define for its mean value from the i-th day to the $(i+n)$-th day which belongs to the next observation series and corresponds to the cycle with the same true anomaly, apart form the perigee motion

$$\overline{\Delta\Omega} = \frac{1}{\delta t'}\{(\lambda_i - \lambda_{i+n}) + (t_i - t_{i+n})\} - \Delta\Phi\,, \tag{20}$$

with

$$\delta t' = (n-1) - \frac{t_i - t_{i+n}}{\text{one day}}\,, \tag{20}$$

where $t_i - t_{i+n}$ in the right-hand side of (20) is always to be positive, making allowance for the retrograde rate of the oribit from the i-th day to the $(i+n)$-th day. The data for determining $\overline{\Delta\Omega}$ and the dependency of $\Delta\Omega$ on T are compiled in Table 6 with reference to Table 3. The data in the first, the second and the third columns of Table 6 are those in Table 3, while the fourth gives the difference of time in days between the neighbouring dates, the fifth the mean rate of the retrograde motion per day obtained, and the sixth the period for each date in the first column, extrapolated using the data in Table 3. The seventh will be explained later.

Table 6.

Date	t	λ	$\delta t'$	$\overline{\Delta\Omega}$	T	T
	h m		d		m	m
Nov. 7, '57	5 21.383	133.°13	46.522	2.°689	103.577	102.446
Dec. 23, '57	17 53.181	134. 20	87.040	2. 965	101.250	98.079
Mar. 20, '58	18 49.922	136. 11			94.378	
Dec. 16, '57	5 22.992	132. 53	39.546	2. 817	101.652	100.464
Jan. 24, '58	18 29.245	145. 57	54.443	3. 040	99.093	96.998
Mar. 20, '58	5 6.812	127. 01			94.451	
*Mar. 19.9, '58				3. 18		94.486

* Direct observational datum on March 18, 19 and 20 evenings in 1958.

Now we shall empirically set forth the relation between $\Delta\Omega$ and T in the form:

$$\Delta\Omega = KT^k\,, \tag{21}$$

where K and k are constants. The mean rate of the retrograde motion with respect to the period from the i-th day to the $(i+n)$-th day is

$$\frac{1}{T_{i+n} - T_i}\int_{T_i}^{T_{i+n}} \Delta\Omega\, dT = \frac{K}{k+1}\,(T_{i+n}^{k+1} - T_i^{k+1})\,. \tag{22}$$

As is seen from Fig. 8 the period does not vary linearly with respect to time, so the mean value (20) is not strictly equal to the mean value (22). As a rough approximation, however, we shall seek for the constants K and k by equating (20) to (22).

The empirical formula between $\Delta\Omega$ and T thus obtained by using the data for four intervals in Table 6 may be given as follows:

$$\Delta\Omega = (4.49 \pm 0.01) \times 10^4 T^{-2.1 \pm 0.1}, \tag{23}$$

where $\Delta\Omega$ is in degrees of arc, and T in minutes of time. Further $\Delta\Omega$ is known linearly dependent on $\cos i$, so we get with (13) and (23)

$$\Delta\Omega = (1.08 \pm 0.01) \times 10^5 \cos i \; T^{-2.1 \pm 0.1}. \tag{24}$$

Fig. 8 shows that the period considerably deviates from the linearity with respect to time for such intervals as given in Table 6. The longer the intervals, the errors of $\overline{\Delta\Omega}$ incurred through the uncertainties of longitudes are smaller, whereas the permissibility of equating (20) to (22) is broken. Then we shall take $\overline{T}$, the mean period

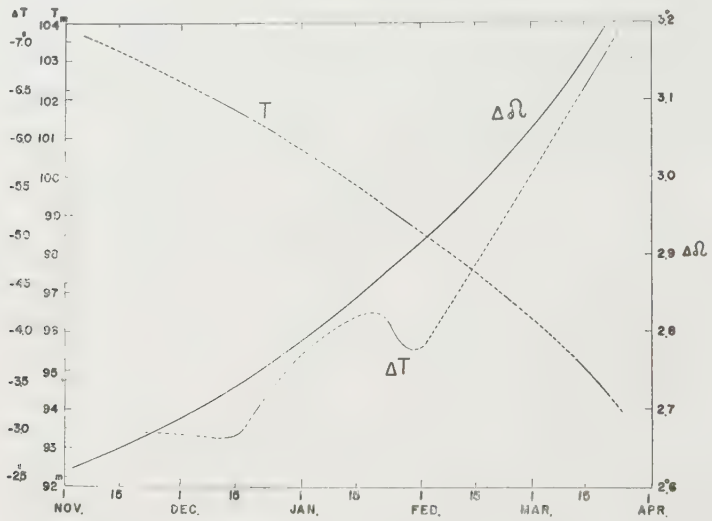

Fig. 8. The behaviors of T and ΔT *versus* date: T in minutes of time, ΔT in seconds of time; the solid curve is such as obtained directly from the observations, the dashed curve as intercombined smoothly. The behavior of $\Delta\Omega$ *versus* T or date (see § 10).

with respect to long time, approximating T by the quadratic curve with respect to time from the i-th day to the $(i+n)$-th day. $\overline{T}$ thus obtained is given in the seventh column of Table 6. As an alternative approximate method for finding out the relation (21), we shall make $\overline{\Delta\Omega}$ correspond, one to one, to $\overline{T}$ for each interval. By means of the method of least squares with five data in Table 6 we derive other formulae:

$$\Delta\Omega = 4.36 \times 10^4 T^{-2.093 \pm 0.01}, \tag{25}$$

and

$$\Delta\Omega = (1.05 \pm 0.01) \times 10^5 \cos i \; T^{-2.093 \pm 0.01}. \tag{26}$$

Numerically the value (25) is larger than (23) by about 0.°01 throughout the period of 1957 β. The empirical formulae (23) and (24) are illustrated respectively in Figs. 8 and 9, by taking the inclination i as a parameter.

Since the air resistance to the satellite may be expected to have the same component of force as that due to non-central terrestrial gravitation in accordance with the shape and with the flying mode of the satellite the relation (24) or (26) is not universal.

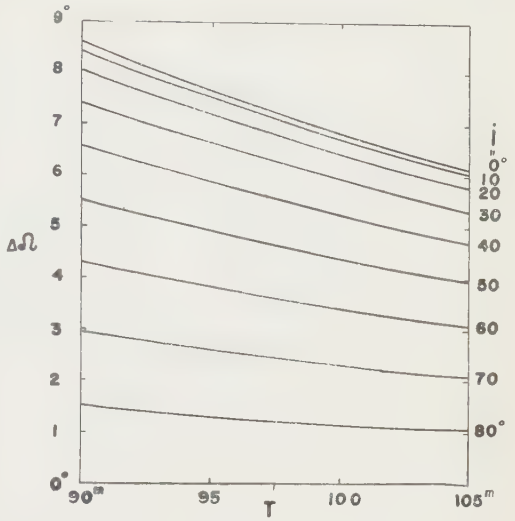

Fig. 9. The behavior of $\Delta\Omega$ *versus* T, taking i as a parameter.

11. Atmospheric density

The work performed by air resistance to the satellitc diminishes its total energy, and the dimensions of the orbit progressively decrease. In other words, we may be able to determine the atmospheric density by observing the changes of the orbital elements.

We shall treat the subject following the analysis given by I. M. Yaçunski (**3**). He confines himself to the plane orbit problem. Namely, no perturbations of the node or of the inclination occur. Likewise he takes no account of the secular perturbations of perigee. Therefore his treatment reduces to calculating merely the secular perturbations of the parameter p and thd eccentricity ε of the orbit.

For the acceleration Γ due to air resistance we may have

$$\Gamma = \frac{C\sigma_s}{2m_s}\rho V^2 = \frac{1}{2}b\rho V^2, \tag{27}$$

with

$$b = \frac{C\sigma_s}{m_s}, \tag{28}$$

where ρ is the air density, C the coefficient of air resistance, V the orbital velocity, σ_s the frontal cross-sectional area and m_s the mass of the satellite.

On the basis of the plane orbit problem, we shall have the differential equations for determining p and ε as functions of v as:

$$\frac{dp}{dv} = \frac{r^2}{GM}\cdot 2rY, \tag{29}$$

and

$$\frac{d\varepsilon}{dv} = \frac{r^2}{GM}\left\{X \sin v + \left(1+\frac{r}{p}\right) Y \cos v + \varepsilon \frac{r}{p} Y\right\}, \tag{30}$$

where X and Y are the projections of the perturbing acceleration on the radius vector and on the perpendicular to the radius vector in the plane of the ellipse, respectively. X and Y may be given by

$$\left.\begin{aligned} X &= -\frac{\Gamma}{V}\left(\frac{GM}{p}\right)^{1/2} \varepsilon \sin v = -\frac{1}{2} b\rho \frac{GM}{p} \varepsilon \sin v (1+2\varepsilon \cos v+\varepsilon^2)^{1/2}, \\ Y &= -\frac{\Gamma}{V}\left(\frac{GM}{p}\right)^{1/2}(1+\varepsilon \cos v) = -\frac{1}{2} b\rho \frac{GM}{p}(1+\varepsilon \cos v)(1+2\varepsilon \cos v+\varepsilon^2)^{1/2}. \end{aligned}\right\} \tag{31}$$

Substituting the expressions (31) into (29) and (30), we get

$$\frac{dp}{dv} = -b\rho p^2 (1+2\varepsilon \cos v+\varepsilon^2)^{1/2}(1+\varepsilon \cos v)^{-2}, \tag{32}$$

and

$$\frac{d\varepsilon}{dv} = -b\rho p(\varepsilon+\cos v)(1+2\varepsilon \cos v+\varepsilon^2)^{1/2}(1+\varepsilon \cos v)^{-2}. \tag{33}$$

For the density distribution, we shall assume the exponential function of the type

$$\rho = Ae^{-\alpha H}, \tag{34}$$

where A and α are constants. Substituting (34) into (32) and (33) with the relations (1) and expanding these into power series and retaining terms of order ε^2 with allowance for the smallness of ε, we get, instead of (32) and (33),

$$\begin{aligned} \frac{dp}{dv} = Abp^2 e^{-\alpha(p-R_\phi)} e^{x\cos v} &\left(1-\varepsilon x \cos^2 v+\frac{\varepsilon^2}{2} x^2 \cos^4 v\right) \\ &\times\left\{\left(1+\frac{\varepsilon^2}{2}\right)-\varepsilon \cos v+\frac{\varepsilon^2}{2}\cos^2 v\right\}, \end{aligned} \tag{35}*$$

and

$$\begin{aligned} \frac{d\varepsilon}{dv} = -Abpe^{-\alpha(p-R_\phi)} e^{x\cos v} &\left(1-\varepsilon x \cos^2 v+\frac{\varepsilon^2}{2} x^2 \cos^4 v\right) \\ &\times\left\{\varepsilon+\left(1-\frac{\varepsilon^2}{2}\right)\cos v-\varepsilon \cos^2 v+\frac{\varepsilon^2}{2}\cos^3 v\right\}, \end{aligned} \tag{36}$$

with

$$x = \alpha p \varepsilon. \tag{37}$$

Let η denote the number of revolutions around the Earth. We shall integrate (35) and (36) with respect to v between the limits 0 and $2\pi\eta$, assuming that the changes of p and ε are negligibly small in this interval. Then we have approximately

$$p-p_0 = -2\pi\eta Abp_0^2 e^{-\alpha(p_0-R_\phi)} F_p(x), \tag{38}$$

and

$$\varepsilon-\varepsilon_0 = -2\pi\eta Abp_0 e^{-\alpha(p_0-R_\phi)} F_\varepsilon(x), \tag{39}$$

* Hereafter, we have somewhat different expressions from those given by YAÇUNSKI (3).

with

$$F_p(x) = \left\{(1+\varepsilon_0^2) - \varepsilon_0 x + \frac{\varepsilon_0^2}{2} x^2\right\} I_0(x) - \frac{\varepsilon_0^2}{2x} I_1(x) + \frac{\varepsilon_0^2}{2} I_2(x)\,, \tag{40}$$

and

$$F_\varepsilon(x) = \left\{\frac{\varepsilon_0}{x} + (1-\varepsilon_0^2) - \varepsilon_0 x + \frac{\varepsilon_0^2}{2} x^2\right\} I_1(x) + \\ + \left(\frac{5\varepsilon_0^2}{2x} + \varepsilon_0 - \varepsilon_0^2 x\right) I_2(x) + \frac{3\varepsilon_0^2}{2} I_3(x)\,, \tag{41}$$

where $I_i(x)$'s $(i=0, 1, 2, 3)$ are modified Bessel functions and the suffix zero denotes the initial values. Eliminating A from (38) and (39) we get

$$\frac{p-p_0}{p_0} \Big/ (\varepsilon - \varepsilon_0) = \frac{F_p(x)}{F_\varepsilon(x)}\,. \tag{42}$$

Now we shall find out the constant α for those days in March observations. As the starting data March 19.308 will be taken, and as the ending March 20.705. We shall assume, in the first approximation, that the increment of eccentricity for short time interval may be equal to $\frac{2}{3}\frac{\delta T}{T_0}$. Then, from the data in Table 3 and from the value given in (10) we have

$$\left.\begin{aligned} \varepsilon_0 &= 0.0440\,, \quad p_0 = 6862\,\text{km}\,, \quad \text{for Mar. } 10.308\,, \\ \varepsilon &= 0.0428\,, \quad p = 6854\,\text{km}\,, \quad \text{for Mar. } 20.705\,. \end{aligned}\right\} \tag{43}$$

Using the values (43) we evaluate the right-hand side of (42) for the probable range of x. This is given in Table 7. The second column of Table 7 is the scale height calculated from (37) and (43), for x in the first column. As is seen from Table 7, $F_p(x)/F_\varepsilon(x)$ decreases very slowly with increasing x and is close to unity for a considerable range of x. On the other hand, the value of the left-hand side of (42) is nearly equal to unity in the first approximation. Consequently we cannot uniquely fix x unless there are very precise and successive observational data for the parameter p and the eccentricity ε.

Table 7.

x	$1/\alpha$	$F_p(x)/F_\varepsilon(x)$
1	293 km	2.125
2	147	1.378
3	98	1.189
4	73	1.115
5	59	1.078
6	49	1.056
7	42	1.041
8	37	1.031
9	33	1.024
10	29	1.018

In order to limit x to a narrower range the following procedure may be taken, though this is not substantially different from the above. The left-hand side of (42) is analytically given, retaining terms of order ε, by

$$\frac{p-p_0}{p_0} \Big/ (\varepsilon - \varepsilon_0) = 1 + 2\frac{\delta H_P}{\delta H_A} - \varepsilon\,, \tag{44}$$

where $\delta H_P/\delta H_A$ is the ratio of the increment of the perigee height to that of the

apogee one. We cannot, however, know this reliable value by March observations. From (12) and (16) we may estimate the mean value of $\delta H_P/\delta H_A$ to be about 0.02 from December 16 to March 20. On the other hand, if a supposition that 1957 β burnt out for example in a circular orbit at 150 km altitudes on April 14 is admissible, we may estimate the mean value of $\delta H_P/\delta H_A$ to be about 0.07 from March 20 to April 14. Then we shall roughly assume that $\delta H_P/\delta H_A$ near on March 20 is bounded by

$$0.03 < \frac{\delta H_P}{\delta H_A} < 0.06\,, \tag{45}$$

from which we have for (44)

$$1.017 < \frac{p-p_0}{p_0} \Big/ (\varepsilon - \varepsilon_0) < 1.077. \tag{46}$$

Then, from (42), (46) and Table 7, we get finally for $1/\alpha$

$$29\ \mathrm{km} < \frac{1}{\alpha} < 59\ \mathrm{km}\,. \tag{47}$$

Next we shall return to Eq. (38). b may be estimated as $1.18\times10^{-2}\ \mathrm{m^2kg^{-1}}$ with C 2, σ_s 3 $\mathrm{m^2}$ and m_s 508.3 kg. Using (43), η 21.29 and $R_\phi = R_{3^\circ\mathrm{N}} - 6378$ km we have for A

$$A = 10^{-10} \times \frac{e^{4.84\times10^2\alpha}}{F_p(x)}\ \mathrm{kg\ m^{-3}}\,. \tag{48}$$

The restriction (47) and the expression (48) will determine a probable range for the density distribution (34). This is illustrated in Fig. 10.

In short, what we can say about the density distribution at about 195 km altitudes above the equatorial regions is no more than that, corresponding to 30 km < scale height < 60 km, the air density lies between $10\times10^{-10}\ \mathrm{kg\ m^{-3}}$ and $6\times10^{-10}\ \mathrm{kg\ m^{-3}}$. Further the lack of reliable information on b will make the above values uncertain by factor two.

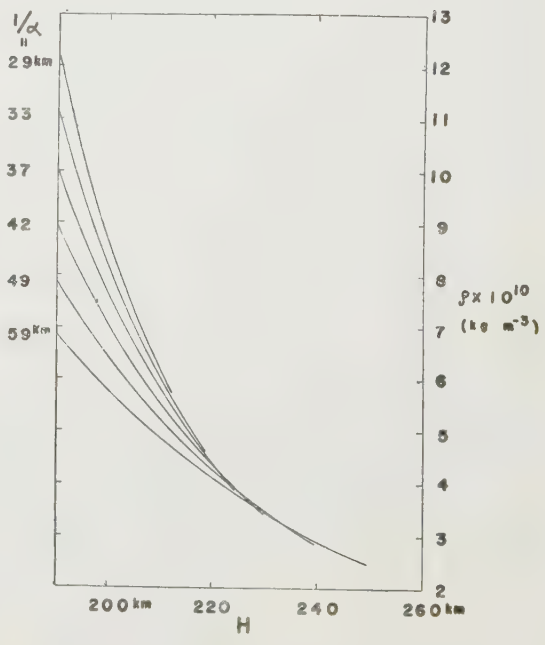

Fig. 10. The behavior of ρ *versus* H, taking $1/\alpha$ as a parameter.

12. Acknowledgement

We wish to express our sincere

thanks to Professor S. Miyamoto, who planned this work and encouraged us throughout the observations.

Our thanks are due to Press the Osaka Yomiuri for financial supports and for communications that made this investigation possible; to Kotobukiya Co., Ltd. under whose sponsorship the Schmidt cameras were constructed; to Osaka Industrial Research Institute (Ikeda Station) for making a 60 cm mirror gratis; and to Fuji Photo Film Co., Ltd. for technical advices and for furnishing photographic materials.

In particular, we are grateful to Western Japanese Moon Watch teams, especially to Miyazaki Team headed by Dr. M. Inaba and also to Kanaya Team headed by Dr. K. Komaki who placed many valuable data at our disposal.

Lastly it is our pleasure to thank Messrs. I. Kawaguchi, S. Tominaga, J. Kubota, T. Inada and others at Kwasan Observatory for their co-works, M. T. Osaki for his helpful discussion, and Dr. J. Jugaku for reading the manuscript.

REFERENCES

1. Surveys of the Japanese Hydrographic Bureau, *Chart No. 1009, Japan and the Adjacent Seas*, $\frac{1}{3,000,000}$ (Lat. 35°N).
2. L. G. Jacchia, Sky and Telescope, **17** (1958), No. 6.
3. I. M. Yaçunski, Uspekhi Fiz. Nauk, **63** (1957), 1, 59-71.

Memoirs of the College of Science, University of Kyoto, Series A,
Vol. XXIX, No. 2, Article 2, 1959.

ABSOLUTE MEASUREMENT OF γ-QUANTA

BY

Teruo NAKAMURA, Kiyoji FUKUNAGA, Kunio TAKAMATSU
and **Shinjiro YASUMI**

(*Received December 6, 1958*)

ABSTRACT

Absolute measurement of γ-quanta from the Li-p reaction was performed by Hough's method. By using this result, the efficiency of the γ-monitor was calibrated and the Pb thick-walled G-M counter was also calibrated which was previously used in our laboratory.

Discussions are given on the determination of the absolute number of γ-quanta with the previous γ-counter as well as on the absolute cross section values of (γ, n) reactions.

1. Introduction

Up to the present, several measurements on the cross sections of photo-nuclear reaction by Li-p γ-ray have been performed in our laboratory (**1**), in which the absolute number of the γ-ray flux was measured with Pb thick-walled G-M counter (**2**) whose efficiency was calculated theoretically (**3**).

In the present work we determined the absolute number of Li-p γ-ray flux by using Hough's method (**4**), and then calibrated the efficiency of the γ-monitor counter, with which we measured (γ, n) cross sections of Cu^{63}, Zn^{64} and Ag^{109} for Li-p γ-ray. Furthermore, using this result, we evaluated experimentally the efficiency of the Pb thick-walled G-M counter for Li gamma ray (hereafter we shall call this the 'previous γ-counter') and tried to correct the photo-nuclear cross sections obtained by the previous experiments (**1**).

2. Experimental method and apparatus

Hough's method may be summarized as follows: When a thin metal foil is placed in front of a Geiger counter on the passage of γ-rays, the counting rate of the counter will increase due to secondary electrons from metal foil produced by γ-rays. From this excess counting rate and the electronic cross section of γ-ray for a converter material, we can obtain the γ-ray flux at the position of the converter foil. Fig. 1 shows schematic view of the apparatus used in the present measurement.

We can expect that a G-M counter can count almost all the secondary electrons

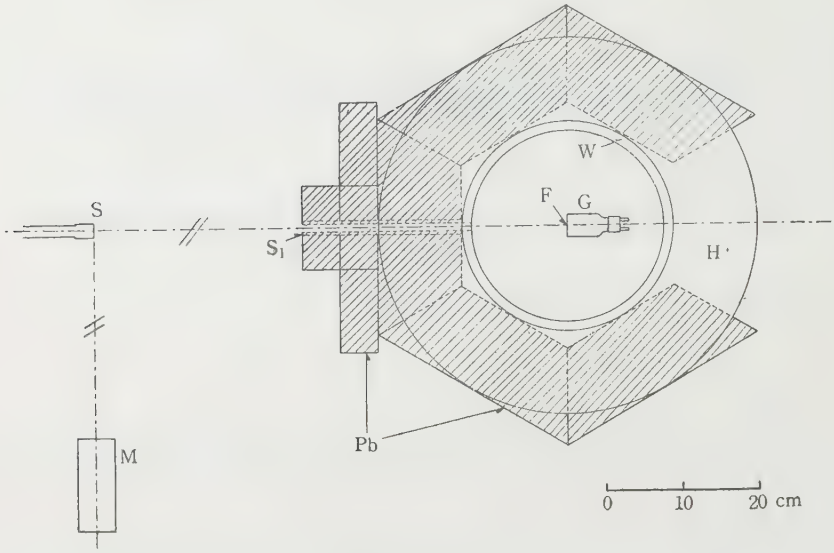

Fig. 1.

G : GM counter for converting electron
S1 : γ-ray slit
Pb : lead shield for γ-ray
H : Helmholtz coil
F : converter foil
S : γ-ray source
W : inner shield of wood
M : monitor counter

produced at Pb converter foil if the latter foil is sufficiently thin and the counter window is also sufficiently thin and wide*.

In this case, the count of the counter is given as follows:

$$N_c(w) = N_{c0} + n_\gamma \frac{A_0}{M} w \bar{\sigma}_e , \qquad (1)$$

where

$N_c(w)$: count of the counter with Pb foil of w gram,
N_{c0} : count of the counter without Pb foil,
n_γ : number of γ-quanta per cm^2 at the position of the Pb foil,
$\bar{\sigma}_e$: electronic absorption cross section of Pb for Li-p γ-ray (averaged over 17.6 Mev and 14.8 Mev γ-rays),
w : weight of the Pb converter foil (gram),
A_0 : Avogadro number,
M : molecular weight of Pb.

The γ-monitor counter to be calibrated was in operation together with the converter counter, and we measured the ratio of $N_c(w)$ to the count of γ-monitor counter N_M for various weights of the converter. Then, Eq. (1) becomes

$$N_c(w)/N_M = N_{c0}/N_M + (n_\gamma/N_M)(A_0/M) w \bar{\sigma}_e . \qquad (2)$$

* For this point, see Appendix.

We used end-window type G-M counters whose mica windows are about 2 mg per cm^2 thick for both the converter counter and a β-counter in the γ-monitor counter. The construction of the latter is shown in Fig. 2.

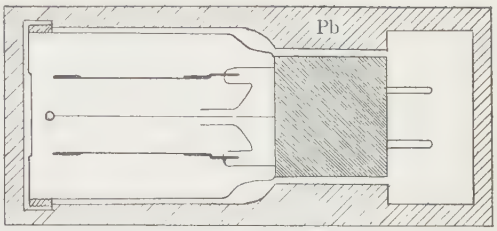

Fig. 2. γ monitor counter.

The ratio N_{c0}/N_M should be as small as possible to ensure the accuracy of measurements. For this purpose special care was taken for arrangements of the apparatus as follows: (1) The dimension of the slit in Fig. 1 was so chosen that the γ-ray flux through it sufficiently covered the converter foil (1 cmϕ) and did not collide the G-M counter wall, (2) Helmholtz coils and Pb blocks were arranged as shown in Fig. 1 and Pb blocks were hollowed at the backward of the counter, (3) the magnetic field of the Helmholtz coils was used to remove secondary electrons from the surrounding materials, the intensity of which was about 1,600~2,000 gauss at the center of the coils, and so all electrons of energy of about 5 Mev or less were deflected and could not reach the β-counter tube, (4) the inside surface of the shield was covered with wood of 2 cm thick, so that the secondary electrons from it were fewer than Pb (low Z) and also the secondary electrons from the inside surface of the shields were partly absorbed, and (5) the converter was held with 'cello tape' in front of the mica window of the G-M converter counter.

In this experiment, the alignment of γ source-slit-converter-counter system is very important and so we ascertained these alignment in every run by a special jig. The slit of 5 mmϕ was placed just before the Li-target in order to define the position of the γ source as well as possible.

3. Results

The ratio $N_c(w)/N_M$ is plotted against various thicknesses (w=0, 0.1881, 0.2640, 0.3533 and 0.4989 grams) of the converter foils in Fig. 3, in which a solid line is a best fit by the method of least squares using Eq. (2). From this slope of the straight line, we find

$$n_\gamma/N_M = (5.12 \pm 0.62) \times 10^{-1},$$

where we have used $\bar{\sigma}_e = (19.6 \pm 0.12)$ barn as the electronic absorption cross section of Pb for Li-p γ-ray, averaged over 17.6 Mev and 14.8 Mev γ-rays (**5**).

Consequently, the total number of γ-quanta, $N_\cdot$, emitted from a target is given as follows for one count of the monitor counter placed at a distance of 31.7 cm from the γ-source:

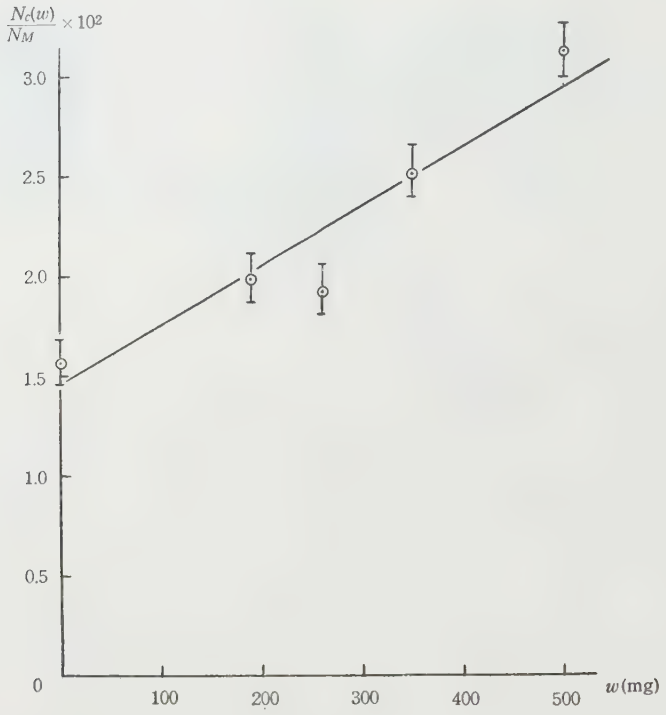

Fig. 3.

$$\frac{N_\gamma}{N_M} = \frac{n_\gamma}{N_M} 4\pi R^2 = (1.63 \pm 0.20) \times 10^4 .$$

We examined the variation of $N_M(d)/N_0$ against d^2, by changing the distance between the γ-monitor counter and the γ-ray source, where N_0 is the count of another fixed γ-monitor counter. This result indicates that the inverse square law holds nearly well.

The error of the result is considered to come from several origins: namely, w, $\bar{\sigma}_e$, R, counting-losses of electrons from the converter foil, the absorption of the γ-ray by the converter foil, and the statistical error of the β-counting. For w, $\bar{\sigma}_e$ and R, each error is one per cent or less respectively and can be neglected. The counting-loss of electrons is negligible for Li-p γ-rays as shown in Appendix. The absorption of γ-ray by the converter foil is about 3 per cent for Pb foil of 500 mg/0.8 cm^2, but the correction for this was not done. After all, the statistical error is the largest source of errors. Thus the errors of the measured values as shown in Fig. 3 are only the statistical ones of the β-counting. The counting stability of each counter was checked in every measurement with constant γ-source placed at the fixed position.

It is an essential defect of Hough's method that some degraded γ-rays may exist

among the incident γ-rays at the position of converter foil. For the case of Li–p γ-ray, most of them are produced in the forward direction by Compton scattering, and so we tried to reduce them by using the sloped slit.

Another attention was paid to make use of a fresh Li metal target every day, because the contamination of the carbon on the target produces the C^{12}–p γ-ray. Further, we measured the spectrum of the Li–p γ-ray by a NaI crystal scintillation counter with the dimensions of 5 inch$\times$4 inch immediately after the experiment and it was found that the contamination of C^{12}–p γ-ray was negligibly small throughout the experiment.

4. The cross sections of Cu^{63}, Zn^{64}, Ag^{109} (γ, n) reactions

Using the results for the γ-ray flux thus obtained, we measured the cross sections of Cu^{63}, Zn^{64}, Ag^{109} (γ, n) reactions for Li–p γ-rays.

Li metal targets of thickness of 0.5 mm were bombarded with magnetically analysed protons which were accelarated to 500 Kev by a Cockcroft generator and whose intensities were about 50 μA$\sim$100 μA. These γ-rays were irradiated to sample discs made of copper, zinc and silver respectively, and the (γ, n) cross sections of these nuclei were determined by the activation method.

The size of the proton beam spot was about 8 mm in diameter, and the distance between the sample disc and the γ-ray source was 14.5 mm, the former having been fixed on the target box with an aluminium jig as shown in Fig. 4.

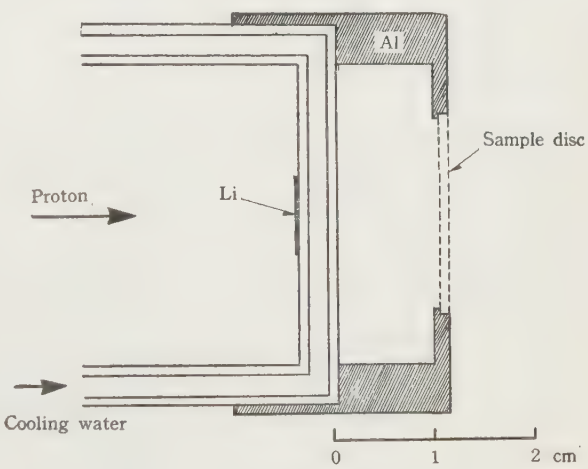

Fig. 4. γ source and sample holder.

The sample discs used are all of diameter of 20 mm, and 1 mm thick for copper and silver and 0.6 mm thick for zinc respectively. These dimensions were the same as the monitor disc's, which had been used by one of the present authors in the measurement of the 14 Mev neutron reaction cross section (**6**). In the β counting we also used the same counting system as that used in the previous measurement by means of the 14 Mev neutron (see Fig. 5).

The cross sections obtained are shown in Table I. In this table λ is decay constant, S is specific activity, C_G is geometrical correction factor and C_k is correction

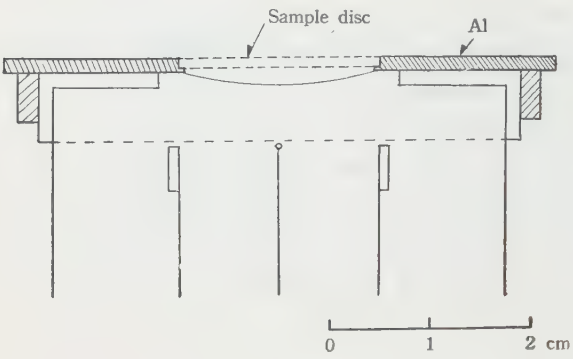

Fig. 5. β counting jig.

factor concerning the branching ratio between the positron emission and the orbital electron capture. The error of the cross section values mainly comes from the error in the determination of γ-ray flux which is about 13%. In the estimation of the cross section by the 17.6 Mev γ-rays only, we adopted Walker and

Table I.

Reaction	λ min^{-1}	S	C_θ	C_k	(Li-pγ) mb	(17.6 Mev) mb
$Cu^{63}(\gamma, n)Cu^{62}$	0.0695	2.84± 3%	4.79±2%	1.043	37.7±15%	42.5
$Zn^{64}(\gamma, n)Zn^{63}$	0.018	3.80±10%	4.80±4%	1.075	20.7±18%	23.3
$Ag^{109}(\gamma, n)Ag^{108}$	0.295	5.03± 7%	4.72±3%	1.00	54.6±16%	61.5

McDaniel's data (**5**) as the intensity ratio of the 17.6 Mev line to the 14.8 Mev line in the Li-p γ-rays, and used the averaged value of several experimental data by the bremsstrahlung (**7**) as the (γ, n) cross section ratio of the 17.6 Mev line to 14.8 Mev line: $\sigma(17.6\ \text{Mev})/\sigma(14.8\ \text{Mev}) = 1.76$.

5. The efficiency of the previous γ-counter

The previous γ-counter which had been used in our laboratory has been constructed to be suitable for high energy γ-ray counting (**2**). Its construction is shown in Fig. 6. Whenever this counter was used as a γ-monitor, it was shielded by 10.5 mm thick lead and its center wire was placed vertically to γ-rays.

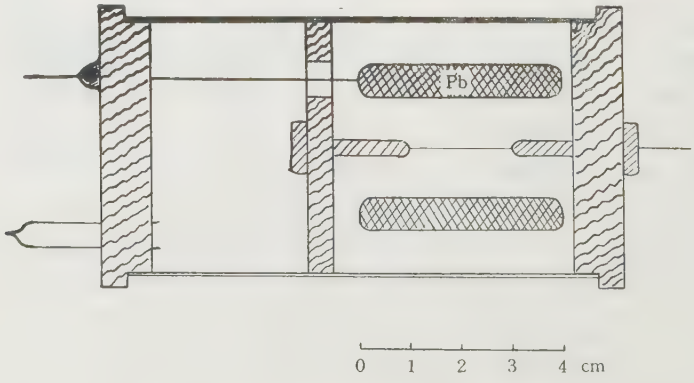

Fig. 6. Reconstructed previous γ counter.

The number of γ-quanta, N_γ, emitted from a target in 4π-steradian has been obtained from the following equation :

$$N_\gamma e^{-\mu x} \frac{a}{4\pi r^2} \eta = N_{\text{prev}} , \qquad (3)$$

where

N_{prev} : count of the previous γ-counter,
η : efficiency of the previous γ-counter,
a : sensitive area of the previous γ-counter,
r : distance between the γ-source and the previous γ-counter*,
μ : practical absorption coefficient of lead, which was determined experimentally to be $0.53\ \text{cm}^{-1}$,
x : thickness of the X-ray shield (being 10.5 mm).

We tried to reconstruct carefully the previous γ-counter as well as possible.

Thus, the plateau slope was about 6% per 100 volts and the applied voltage was 1150 V.

Using the result for N_γ as given in § 3 and assuming a to be $2\,\text{cm} \times 2\,\text{cm}$, we have calculated by Eq. (3) the efficiency of the previous γ-counter, η, for Li-p γ-rays, obtaining

$$\eta = 15.3 \pm 0.2\% ,$$

the error indicated arising mainly from the measurement of N_γ.

So far we have adopted the value of 22% for η which was calculated by Sonoda. No agreement is found between these two values of η within experimental errors. Now, if the present value of 15.3% is used for the efficiency, the cross section value of $Cu^{63}(\gamma, n)Cu^{62}$ reaction for Li-p γ-rays obtained by Shimizu (**1**), for example, is reduced from 77.5 mb to 33 mb. This corrected value is not inconsistent with our experimental value obtained by the present work (see § 4).

The discrepancy between the calculated and experimental values for the efficiency of the previous γ-counter seems to be at least partly due to the X-ray Pb-shield.

In Eq. (3), the effect of the X-ray shield for the γ-ray counting is represented only by a multiplication factor $e^{-\mu x}$, in which μ is the practical absorption coefficient which was obtained by changing the thickness of lead shield. If, however, the Pb thick walled G-M counter is used as a monitor with X-ray shield, it seems to be reasonable that the similar calculations to that for the Pb thick wall must be also made for the X-ray shield. Further, the spectra of gamma rays filtered through the X-ray shield will become quite different from the spectra of the original γ-rays. Hence it is considered to be unreasonable that the calculated value for original γ-rays has been adopted as the value of η in Eq. (3) in the previous works.

* $r = 29.5$ cm for the previous arrangement (see ref. (**1**)) and $r = 30.2$ cm for the present case.

On the other hand, the experimental efficiency of 15% corresponds to the theoretical one for 13.5 Mev γ-quanta by Sonoda's calculation (**3**). This estimation is qualitatively reasonable from the viewpoint of degraded gamma rays, but the more quantitative discussions for this point seem to be impossible at this stage of experiment.

From the same reason as mentioned above, the experimental check of the calculation of the efficiency itself cannot be done too.

But it was found that the efficiency of the calibrated γ-monitor counter (Fig. 2) was 25.4% by Hough's method, and agrees well with the calculated value of 23% for Li-p γ-rays within experimental error. It must be noted here, however, that we assumed all secondary electrons from the area of 20 mm in diameter of the lead converter to have entered into the sensitive volume of the G-M tube (Fig. 2).

The comparison between the experimental and theoretical efficiencies of a thick walled γ-ray counter is useful not only for the correction of the cross sections of the photo-nuclear reaction so far studied in our laboratory, but also for obtaining some informations about the interaction of photons and electrons with matter in bulk. More accurate measurements are now in progress with improved arrangements.

Acknowledgements

The authors wish to express their cordial thanks to Professor K. Kimura for his continual interest and encouragement. They are greatly indebted to Professor M. Sonoda of Kyusyu University, Professors S. Shimizu and Y. Uemura of Kyoto University for valuable discussions, and also to Mr. M. Yata for his cooperative efforts. Further they are grateful to Miss T. Hirata for preparing the manuscript.

APPENDIX

Angular Distribution of Secondary Electrons by Li-p γ-rays

The angular distribution of the pair electrons is given by Heitler (**8**) as follows:

$$
\begin{aligned}
d\Phi = -\frac{Z^2}{137}\frac{e^4}{2\pi}\frac{P_+P_-dE_+}{k^3}\frac{\sin\theta_+\sin\theta_-d\theta_+d\theta_-d\phi_+}{q^4} \\
\times\Big\{\frac{p_+^2\sin^2\theta_+}{(E_+-p_+\cos\theta_+)^2}(4E_-^2-q^2)+\frac{p_-^2\sin^2\theta_-}{(E_--p_-\cos\theta_-)^2}(4E_+^2-q^2) \\
+\frac{2p_+p_-\sin\theta_+\sin\theta_-\cos\phi_+}{(E_--p_-\cos\theta_-)(E_+-p_+\cos\theta_+)}(4E_+E_-+q^2-2k^2) \\
2k^2\frac{p_+^2\sin^2\theta_++p_-^2\sin^2\theta_-}{(E_--p_-\cos\theta_-)(E_+-p_+\cos\theta_+)}\Big\}, \qquad (4)
\end{aligned}
$$

with

$$q^2=(\boldsymbol{k}-\boldsymbol{p}_+-\boldsymbol{p}_-)^2.$$

Integrating this with respect to θ_+ and ϕ_+, and using following approximations:

$$
\begin{aligned}
&(\mu/E_-)^2\ll 1, \qquad (\mu/E_+)^2\ll 1, \\
&p_-=E_-, \qquad p_+=E_+, \\
&\theta_-^2\ll 1, \qquad k-E_+=E_-,
\end{aligned}
$$

we obtain a simple formula as

$$\left.\begin{aligned} d\Phi &= A\frac{\theta_-}{\{(\mu/E_-)^2+\theta_-\}^2}, \\ \text{with}\quad A &= \frac{Z^2e^4}{137k^3}\frac{E_+}{E_-}dE_-\,d\theta_-, \end{aligned}\right\} \qquad (5)$$

where

Z: atomic number, $\mu=m_0c^2$, k: γ-ray energy,

E_+: positron energy, E_-: electron energy,

p_+: positron momentum$\times c$, p_-: electron momentum$\times c$.

By the use of the above equation the angular distributions for $E_-/\mu=10, 17, 25$ are plotted in Fig. 7.

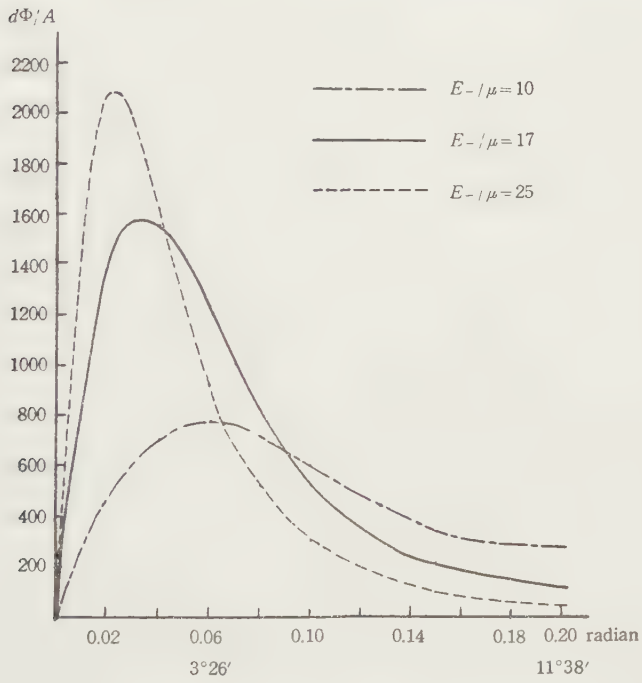

Fig. 7. Angular distribution per unit scattering angle of pair electron.

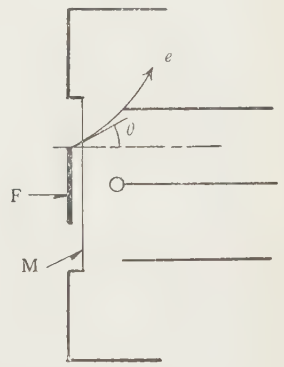

Fig. 8. Counter for converting electron.
F : converter foil
M : mica window
e : path of 8 Mev electron
θ : maximum angle of 8 Mev electron (or positron) entering into the counter

Integrating Eq. (5) with respect to E_- and θ_- over the ranges $2\,\mu\sim33\,\mu$ and $0\sim0.2$ radian (equals to 11°38′) for E_- and θ_- respectively, we obtain an approximate value of 17×10^{-24} cm^2 and hence it is found that 95 per cent of the electrons produced by the pair creation are included in this angular range. When electrons of the energy of 8 Mev or more are emitted at most within 30° in the forward direction in the magnetic field, they are expected to enter into the sensitive volume of end-window counter and can be counted (see Fig. 8).

Since, furthermore, either of pair electrons must have the energy of about 8 Mev or more, almost all electrons produced by the pair creation can be counted by the converter counter.

On the other hand, about 13 per cent of the secondary electrons are produced by the Compton scattering and also in this case it is shown by the theory that the majority of them are emitted within about 14° with the energy of 8 Mev or more (see Fig. 9).

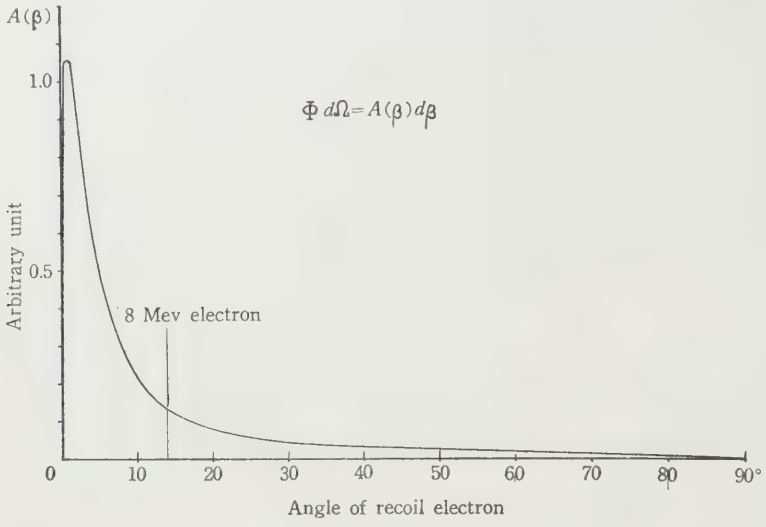

Fig. 9. Recoil electron angular distribution per unit scattering angle of compton scattering by 17.5 Mev γ-rays.

Finally, since for the 14.8 Mev line of Li-p γ-rays the similar considerations seem to be valid, it may be considered that almost all secondary electrons produced by Li-p γ-rays are counted with converter counter.

REFERENCES

1. B. Arakatsu, Y. Uemura, M. Sonoda, S. Shimizu, K. Kimura and K. Muraoka, Proc. Phys.-Math. Soc. Japan, **23** (1941), 440.
B. Arakatsu, M. Sonoda, Y. Uemura and S. Shimizu, Proc. Phys.-Math. Soc. Japan, **23** (1941), 633.
B. Arakatsu, M. Sonoda, Y. Uemura, S. Shimizu, and K. Kimura, Proc. Phys.-Math. Soc. Japan, **25** (1943), 173.
B. Arakatsu, S. Shimizu, T. Hanatani and J. Muto, J. Phys. Soc. Japan, **1** (1946), 24.
S. Shimizu, Mem. Coll. Sci. Kyoto Univ., **A25** (1949), 193.
S. Shimizu, S. Yasumi, Y. Saji and J. Muto, Mem. Coll. Sci. Kyoto Univ., **A26** (1950), 85.
B. Arakatsu, M. Sonoda, Y. Uemura, S. Yasumi and Y. Saji, Mem. Coll. Sci. Kyoto Univ., **A26** (1950), 97.
J. Muto, E. Takekoshi, T. Nakamura, A. Imamura and Y. Tsuneoka, J. Phys. Soc. Japan, **12** (1957), 109.

2. M. Sonoda, Mem. Coll. Sci. Kyoto Univ., **A25** (1949), 175.
3. M. Sonoda, J. Phys. Soc. Japan, **5** (1950), 53, 403, 408.
4. P.V.C. Hough, Phys. Rev., **80** (1950), 1069.
5. R. L. Walker and B. D. McDaniel, Phys. Rev., **74** (1948), 315.
   R. L. Walker, Phys. Rev., **76** (1949), 527.
6. S. Yasumi, J. Phys. Soc. Japan, **12** (1957), 443.
7. H. E. Johns, L. Katz, R. A. Douglas and R. N. H. Haslam, Phys. Rev., **80** (1950), 1062.
   B. C. Diven and G. M. Almy, Phys. Rev., **80** (1950), 407.
   P. R. Byerly and W. E. Stephens, Phys. Rev., **83** (1951), 54.
   V. F. Krohn and E. F. Shrader, Phys. Rev., **87** (1952), 685.
   R. Montalbetti, L. Katz and J. Goldemberg, Phys. Rev., **91** (1953), 659.
   A. I. Berman and K. L. Brown, Phys. Rev., **96** (1954), 83.
8. W. Heitler, *The Quantum Theory of Radiation*, p. 257.

Memoirs of the College of Science, University of Kyoto, Series A,
Vol. XXIX, No. 2, Article 3, 1959.

FERROMAGNETIC RESONANCE IN Ni-Cd FERRITE SYSTEM AT MICROWAVE FREQUENCIES*

BY

Susumu TAKEMOTO**

(*Received December 18, 1958*)

ABSTRACT

Ferromagnetic resonance experiments on spherical polycrystalline specimens of Ni-Cd ferrite system $Ni_{1-x}Cd_xFe_2O_4$ at frequencies of 9700 MC and 24000 MC were performed at room temperature.

The purpose of this paper is to give a brief description of the experimental method and to discuss the variation of the g-factor (g), the line width (ΔH), the damping constant (λ), and the relaxation time (T), as functions of composition. The results show that the values of the effective g-factor are from 2.15 to 2.00 and those of the internal field are from 260 oersteds to about zero, and it was also found that in the magnetic region $0 < x < 0.7$, $3.0\times10^{-10} < T < 10\times10^{-10}$ sec, $0.3\times10^{8} < \lambda < 1.4\times10^{8}$ rad/sec, and $130 < \Delta H < 330$ oersteds at 9700 MC; and $1.9\times10^{-10} < T < 5.0\times10^{-10}$ sec, $0.20\times10^{8} < \lambda < 1.1\times10^{8}$ rad/sec, and $230 < \Delta H < 600$ oersteds at 24000 MC.

1. Introduction

The phenomenon of ferromagnetic resonance was first observed by Griffiths (**1**) in 1946 and many theoretical and experimental investigations have since been performed on this subject. It has been much used as a powerful means for investigating the magnetic properties of magnetic materials. We can determine important ferromagnetic quantities such as the crystalline anisotropy constant, the spectroscopic splitting factor or g-factor, the line width of resonance, and the relaxation time by using the ferromagnetic resonance method.

The resonance experiments on polycrystalline binary ferrite specimens $Ni_{1-x}Cd_xFe_2O_4$ ($x=0, 0.1, 0.2, \cdots, 1.0$) were performed at frequencies of 9700 MC and 24000 MC at room temperature, and a discussion was made on the results of measurement concerning the g-factor (g), the damping constant (λ), the line width (ΔH), and the relaxation time (T) at each Cd-concentration.

The points which have important relations to the ferromagnteic resonance in polycrystalline specimens will be considered in the discussion. A new field of the

* Communicated by Professor I. TAKAHASHI. Read before the annual meeting of the Physical Society of Japan, October 16, 1958.

** Department of Physics, Faculty of Science and Literature, Shimane University.

solid state electronics up to microwave frequencies was opened by the development of the ferrites among materials with spinel structure and recently of ferromagnetic semiconductors with garnet structure which are transparent and have extremely narrow line width.

At present various commmercial ferrites are in most cases made of polycrystalline ferrites and it is very important in practice to investigate various electric and magnetic properties of polycrystalline ferrites and to compare the properties among them.

Particularly it is of much interest from the theoretical and practical points of view that the material is utilized at or near ferromagnetic resonance. We discuss the domain rotation in a sintered polycrystalline ferrite, whose principal differences from a crystalline are summed up in three respects as follows (**2**). First, sintered crystallites must be considered to be randomly oriented; second, they will interact magnetically with each other somewhat in the manner of coupled oscillators; and third, the magnetic properties of the polycrystalline are different from grain to grain according to chemical purity, shape, dimensions, porosity and internal stress. Owing to these complicated circumstances the theory of resonance phenomena in polycrystalline ferrite at microwave frequencies have not yet completely settled.

2. Theory of experiment

The power transmission coefficient T of the cavity is (**3, 4**):

$$T = \frac{4Q_L^2}{Q_1 Q_2} \cdot \frac{\left(\frac{1}{2Q_L}\right)^2}{\left(\frac{\omega-\omega_0}{\omega_0}\right)^2 + \left(\frac{1}{2Q_L}\right)^2}, \qquad (1)$$

where Q_1, Q_2 and Q_L are the input, the output, and the loaded Q, respectively, ω is the angular frequency of the incident microwave, and ω_0 the resonant frequency of the cavity.

By definition,

$$\frac{1}{Q} = \frac{1}{Q_w} + \frac{1}{Q_1} + \frac{1}{Q_2} + \frac{1}{Q_d} + \frac{1}{Q_m}, \qquad (2)$$

where Q_w is the intrinsic Q due to Joule's heat in the cavity wall, Q_d due to the dielectric loss in the cavity space and the sample, and Q_m concerning the magetic resonance absorption in the sample.

When the cavity is completely at resonance, the transmission coefficient T becomes

$$T = \frac{4Q_l^2}{Q_1 Q_2}. \qquad (3)$$

We choose a reference point at very large magnetic field H_z where the loss consists

of lossess other than that due to the resonance absorption, since the ferromagnetic resonance absorption cannot occur.

If $Q_{L(0)}$ is used to denote the loaded Q at the reference point and $Q_{L(H)}$ is the loaded Q at the resonance field, the magnetic absorption loss becomes, from Eq. (2),

$$\frac{1}{Q_m} = \frac{1}{Q_{L(H)}} - \frac{1}{Q_{L(0)}} = \frac{1}{Q_{L(0)}}\left[\left(\frac{Q_{L(0)}}{Q_{L(H)}}\right) - 1\right],$$

and further by Eq. (3) it becomes

$$\frac{1}{Q_m} = \frac{1}{Q_{L(0)}}\left[\left(\frac{T_0}{T}\right)^{1/2} - 1\right], \tag{4}$$

where T_0 and T denote the power transmission coefficient at the reference point and that at the resonance respectively.

When the crystal detector shows square-law character, the detection current I is proportional to the power transmission coefficient T. As $Q_{L(0)}$ is independent of the dc magnetic field, Eq. (4) becomes

$$\frac{1}{Q_m} = \text{const} \cdot \left[\left(\frac{I_0}{I}\right)^{1/2} - 1\right], \tag{5}$$

where I_0 and I denote the detection current at the reference point and that at the resonance respectively. Consequently, we can determine the relative magnetic loss and the line shape at resonance by calculating $\left[\left(\frac{I_0}{I}\right)^{1/2} - 1\right]$ as functions of the dc magnetic field.

In the above theory, we assume that the microwave power incident to the input window of the cavity is always constant, whether the resonance absorption exists or not. But we should be careful of the fact that the frequency and the output of the microwave oscillator are generally affected seriously by the state of the load.

This tendency is particularly remarkable at shorter wavelengths.

The first two attenuators in Fig. 1 are inserted in order to prevent the oscillator from the fluctuation due to the reaction from the load.

3. Experimental method

The 97000 MC and 24000 MC microwave apparatuses used for the measurenments are shown schematically in Fig. 1.

A small ferrite specimen is placed on the bottom wall of a rectangular transmission resonance cavity which is excited in the NE_{10n} mode, n being varied from 6 to 10. The resonance of the cavity is attained by driving the choke piston which composes the upper wall of the cavity by screw micrometer.

The signal oscillator consists of a low-power ($\sim$30 mW) reflex klystron, which is a 2K25 at 9700 MC and a 2K33 at 24000 MC.

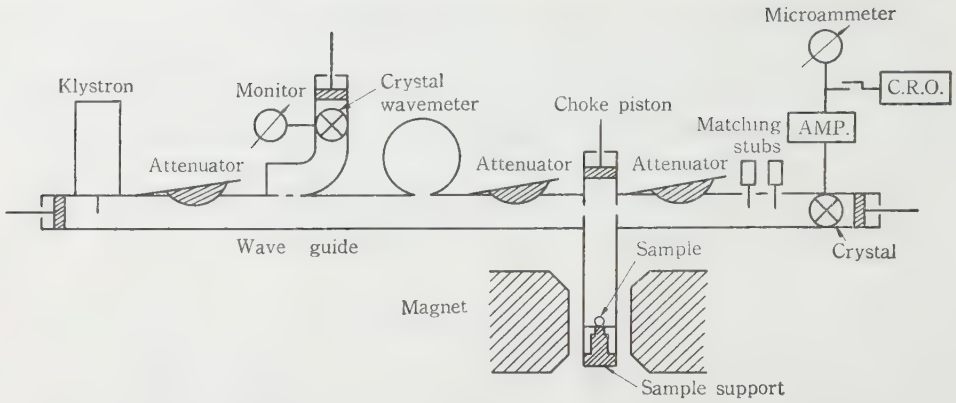

Fig. 1. Schematic diagram of microwave apparatus used at 9700MC and 24000MC.

The oscillator is amplitude modulated by a 6 KC rectangular wave and the output is always monitored by a precision wavemeter in order to keep its intensity and frequency constant.

All measurements are made, of course, with the cavity tuned to the resonance. The cavity is placed between the pole pieces of an electromagnet (10 cm dia.) in such a way that the rf magnetic field is orthogonal to the external dc magnetic field H_z.

The electromagnet used is one designed for investigating the nuclear magnetic resonance. The magnetic field at the sample position was measured by proton resonance method.

The field can be determined with an accuracy of 1% by this method.

A current of 10 amp. through the field coils provided a field of about 14000 oersteds. As shown in Fig. 1, we measured the variation in the signal transmitted through the cavity as the dc magnetic field was changed.

After detection, the signal was amplified by a narrow-band amplifier which was tuned to 6 KC modulation frequency.

Since the fluctuation of frequency and output of the oscillator limits the sensitivity and accuracy of experiment, we should carefully design the voltage regulated power supply to the klystron. In order to achieve greater stability and sensitivity of the present experiment, it is not sufficient only to stabilize the dc voltage supplied to the oscillator, but it is necessary that the very frequency of the oscillator is stabilized by the use of a feed-back circuit system, for example, Pound frequency stabilizer. The polycrystalline specimens made by a sintering and pressing process were prepared spherical by a method developed by Bond (**6**).

In order to obtain the result free from the size effect, the measurements should be done, though it is a tedious work, on very many samples of different diameters which were chosen between 0.3 mm and 1.5 mm.

When the sample diameter becomes larger than about 1 mm, several subsidiary absorption peaks generally appear on the true absorption curve (**7, 8**), due to the dimensional resonance and the resonance caused by the non-uniformity of rf magnetic field in the sample, making it difficult to analyze the resonance curve.

4. Results and discussion

Since the line width, g-value, relaxation time and damping constant of ferrite are in close relation with each other, they cannot be treated independently. However, we shall here discuss the experimental results, dividing them into the following four parts.

A) *The g-factor and the internal field*

The g-values in polycrystalline nickel ferrites have hitherto been found to be from 2.12 to 2.25. This fact shows the presence of spin-orbit coupling. In mixed ferrites the g-value depends remarkably upon composition and temperature.

Although the g-value should be independent of both the applied dc field and the frequency used, it shows, as is well known, conspicuous size effect and frequency dependence according to the results of microwave resonance experiments (**9, 10, 11**). The size effect is avoided by using the dc resonance field H_z which is determined by extrapolating the sample diameter to zero in the resonance experiments. However, the apparent g-factor, g_{app} calculated from Kittel's resonance formula (**12**) :

$$\omega_0 = \gamma H_z , \qquad (6)$$

for a spherical sample, shows marked frequency dependency, as seen in Fig. 3.

To avoid the discrepancy between curves (a) and (b) in the figure, T. Okamura (**13**) proposed the corrected resonance condition :

$$\omega_0 = \gamma (H_z + H_i) , \qquad (7)$$

where H_i is the ad hoc internal field which is a material constant independent of frequency, and H_z the same as in Eq. (6). Therefore, we can determine the effective g-factor (true g-factor)g_{eff} and the internal field H_i from Eq. (7) by the resonance experiments performed at two or more different frequencies. The experimental values of the internal field H_i and the effective g-factor of Ni-Cd ferrite system are given in Figs. 2 and 3 respectively.

The theoretical formula of the effective g-factor in ferrimagnetics was derived by Tuya (**14**) and Wangsness (**15**) and it is found to be in good agreement with expesiments (**10, 16**). The size effect has generally been considered to depend upon the dimensional resonance, the non-uniformity of the rf magnetic field in the sample, and the skin effect. The value of internal field H_i is about 260 oersteds at the composition of $x=0$ (nickel ferrite) and it gradually decreases with richer Cd content, becoming almost 0 in the non-magnetic region ($x>0.7$).

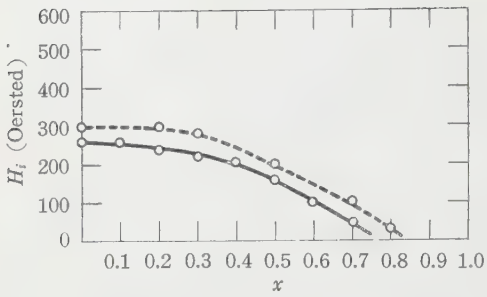

Fig. 2. Solid line : internal field in Ni–Cd ferrite system *versus* Cd content. Dotted line : that in Ni–Zn ferrite system *versus* Zn content.

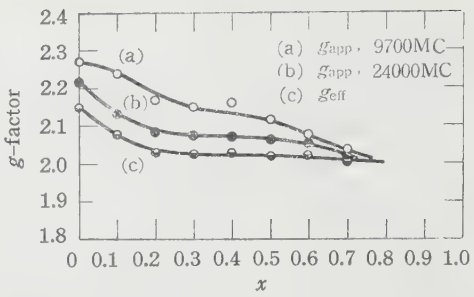

Fig. 3. Apparent g-factor, g_{app} and effective g-factor, g_{eff} of Ni–Cd ferrite system as functions of composition observed at 9700MC and 24000MC.

The dotted line in Fig. 2 shows the internal field in Ni–Zn binary ferrites as a function of Zn concentration. Though many theoretical and experimental investigations (**17**, **18**) have been carried out, the theory of mechanism of the internal field in ferrite has still been unsatisfactory because of the complicated circumstances in polycrystalline material. However, it has been found experimentally (**10**) that the internal field depends upon the porosity or density in the material and decreases with it.

B) *Relaxation time*

The rf magnetic field in the cavity at resonance decays exponentially with time according to $\exp(-\omega_0 t/2Q)$, and consequently the magnetization changes in the same manner. Therefore, the relaxation time associated with the resonance is given by

$$T = \frac{2Q}{\omega_0} = \frac{2H_{res}}{\omega_0 \Delta H}, \qquad (9)$$

where H_{res} denotes the resonance field, Q is the Q-value of the cavity and ΔH the full width between half power points of the absorption curve.

The variation of the relaxation time as a function of Cd content is seen in Fig. 4.

The value of T is of the order of 10^{-10} sec, and is larger at 9700 MC than at 24000 MC, showing frequency dependence. The relaxation time of a single crystal of nickel ferrite is found to be 1.5×10^{-10} sec (**8**), a larger value than that of the present polycrystalline sample.

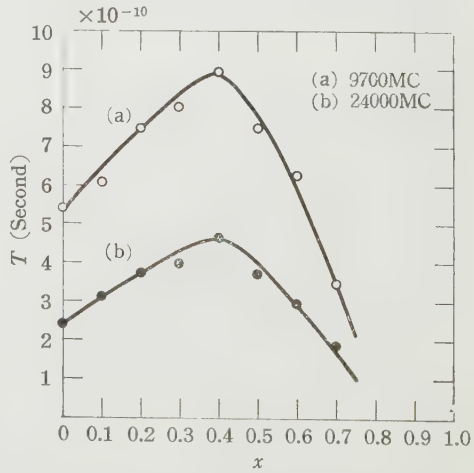

Fig. 4. Variation with composition of relaxation time of Ni–Cd ferrite system observed at 9700 MC and 24000MC.

The reason for this seems to originate in the increase of the line width due to the increase of the anisotropy energy in polycrystalline specimen. The relaxation time T is maximum at $x=0.4$ and shows a remarkable reduction at $x=0.7$ at both frequencies, as shown in Fig. 4.

This fact is also considered to be due to the variation of line width with composition. The relaxation time T of commercial ferrite relates to the figure of merit F as $F=\omega T$ (**19**), which is an important quantity describing the quality of the microwave gyrator.

C) *Line width*

It is known that the line width of the resonance which has hitherto been measured is as broad as several hundreds oersteds and tends to a constant value at very low temperatures.

The physical mechanisms which can explain the two experimental results mentioned above are not well understood. As mentioned in the previous section, the true line width is superposed by the spurious line width owing to the dispersion of the resonance frequency in the individual crystal grain in polycrystalline specimen.

The latter broadening is expected to be about one fourth of the anisotropy field $H_a = \frac{2K_1}{M_s}$, provided that $H_a \ll H_{res}$.

The chemical impurities, vacancies, and lattice defects seem to contribute to the line width, but this effect will probably be small.

As the magnetic ions on the octahedral site are randomly distributed in ferrites with inverted spinel structure, the fluctuation of the magnetic interaction in the lattice as a whole occurs and is also effective to the line width. Eddy currents are rather unimportant to the line width in ferrites.

Fig. 5 shows the variation of the line width of Ni-Cd ferrite system as a function of composition.

It is of interest that the line width at 97000 MC is about two times larger than that at 24000 MC. It is experimentally known that the line width varies linearly with frequency.

Although many experimental and theoretical studies have been continued,

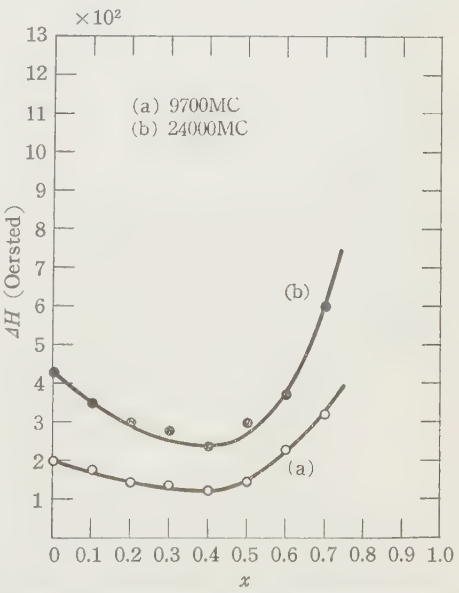

Fig. 5. Line width of Ni-Cd ferrite system as function of composition observed at 9700 MC and 24000 MC.

the microscopic mechanism of the line width of the resonance line in the ferrimagnetics such as ferrite is still not clear.

However, the line width theory developed by Clogston *et al.* (**20**, **21**) will hereafter be a strong clue to the source of line width in ferrimagnetics.

D) *Damping constant*

To account for the line width acutually observed, it is necessary to correct the Kittel's equation of motion by adding a term representing dissipation of energy. The shape of resonance line can be estimated by this damping term which is determined by the line width.

Since the microscopic mechanism of line width has still been obscure, the damping term is also doubtful. Several damping terms (**22**, **23**) have been introduced in a phenomenological way.

We used the equation of motion for the magnetization vector $\boldsymbol{M}$ of the ferromagnetic material in the form, first introduced by Landau-Lifshitz (**22**) :

$$\frac{d\boldsymbol{M}}{dt} = \gamma[\boldsymbol{M} \times \boldsymbol{H}] - \frac{\lambda}{\boldsymbol{M}^2}[\boldsymbol{M} \times (\boldsymbol{M} \times \boldsymbol{H})], \tag{10}$$

where $\boldsymbol{H}$ denotes the effective magnetic field at resonance, γ is the effective gyromagnetic ratio for the two-lattice system, and λ the damping constant responsible for the damping of magnetic energy, which has a dimension of frequency and is called the damping frequency or the damping constant.

The second term of the right-hand side of Eq. (10) is a vector expressing the damping and rotates the vector $\boldsymbol{M}$ toward the field vector $\boldsymbol{H}$ and leaves the magnitude of $\boldsymbol{M}$ a constant of the motion. Hence, Eq. (10) is valid only when the small amplitude of the rf field is used.

The other form of damping is the Bloch-Bloembergen form (**23**, **24**) which has two characteristic parameters but does not conserve M. It has been shown experimentally that we should use the damping form of the Bloch-Boembergen type in the case using the microwave of high energy. The value of damping constant λ is determined by measuring the line width ΔH.

The relation between λ and ΔH is given by (8)

$$\lambda = \frac{\gamma M_s \Delta H}{2H_{\mathrm{res}}}, \tag{11}$$

where M_s denotes the saturation magnetization and H_{res} is the magnetic field required for resonance.

In the case of polycrystalline material λ in Eq. (11) is considered to express not the intrinsic damping constant but the effective damping constant which includes the spurious damping as mentioned above.

Fig. 6 gives the results of measurement of λ.

The value of λ seems to depend somewhat upon the frequency, taking larger value as the frequency decreases and is of the order of about 10^8.

It is remarkable in these expriments that first, the relaxation time T appears to be more dependent upon the frequency than the damping constant λ is; second, at the composition of $x=0.4$, the saturation magnetization M_s (**25**) and the relaxation time T have both maximum values and λ becomes minimum, and third, at $x=0.7$ the line width ΔH shows sharp increase and λ sharp decrease on the contrary.

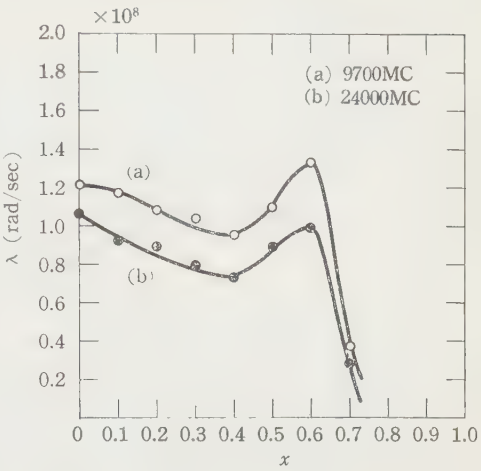

Fig. 6. L-L type damping constant as function of composition of Ni-Cd ferrite system observed at 9700MC and 24000 MC.

It is reasonable that at the composition of $x=0.4$, the dissipation of energy takes a minimum value which just coincides with the maximum relaxation time.

The increase of ΔH at $x=0.7$ seems to be mainly due to the decrease of exchange force and the increase of the anisotropy energy, and the decrease of λ at the same composition is due more to the large decrease of M_s than to the increase of ΔH.

On the other hand, the damping constant is determined by the experiment of domain wall motion (**26**).

It is difficult, however, to determine the damping constant of metals accurately owing to the effect of eddy currents.

The values of λ of various ferrites are listed in Table I below.

Table I. Measured values of damping constant λ of various ferrites.

Material	Frequency (MC)	λ (ferrom. res.)	λ (wall motion)
Fe_3O_4 (single crystal)	24000	9×10^8 rad/sec*	3.5×10^8 rad/sec*
$NiFe_2O_4$ (single crystal)	24000	2.1×10^7 „ *	2.2×10^7 „ *
	9000	7.2×10^7 „ *	—
$NiFe_2O_4$ (polycryst.)	24000	1.0×10^8 „ †	—
	9700	1.2×10^8 „ †	—
$Ni_{0.5}Cd_{0.5}Fe_2O_4$ (polycryst.)	24000	0.90×10^8 „ †	—
	9700	1.1×10^8 „ †	—

* The values by J. K. Galt, J. Andrus, and H. G. Hopper, reference **23**.
† The values by the author.

Acknowledgements

The author wishes to express his sincere thanks to Professor I. Takahashi of Kyoto University for his helpful advices and discussions. He is also indebted to Lecturer M. Oka of Shimane University for his assistance in the measurements and to Messrs. M. Igeta and T. Tokue of Tokyo-Rika-Kogyo Co. for their supply of ferrite samples used in the present work.

REFERENCES

1. J. H. E. Griffiths, Nature **158** (1946), 670.
2. D. Park, Phys. Rev., **97** (1955), 60.
3. J. C. Slater, Rev. Mod. Phys., **18** (1946), 441.
4. S. Tomonaga, J. Phys. Soc. Japan, **2** (1947), 158.
5. S. Takemoto, Rep. Shimane Univ. (Natural Sci.), No. **6** (1956), 26.
6. W. L. Bond, Rev. Sci. Instr., **22** (1951), 344.
7. R. L. White and I. H. Solt, Phys. Rev., **104** (1956), 56.
8. W. A. Yager, J. K. Galt, F. R. Merritt, and E. A. Wood, Phys. Rev., **80** (1850), 744.
9. W. A. Yager, F. R. Merritt, and C. Guillaud, Phys. Rev., **81** (1951), 477.
10. Y. Kojima, Sci. Rep. RITU, **A6** (1954), 614.
11. G. H. Belijers and D. Polder, Nature **165** (1950), 800.
12. C. Kittel, Phys. Rev., **73** (1948), 155.
13. T. Okamura, Y. Torizuka and Y. Kojima, Phys. Rev., **88** (1952), 1425.
14. N. Tuya, Prog. Theor. Phys., **7** (1952), 263.
15. R. K. Wangsness, Phys. Rev., **91** (1954), 1085.
16. E. W. Gorter, Philips Res. Rep., **9** (1954), 321.
17. M. Date, Sci. Rep. RITU, **A6** (1954), 109.
18. R. M. Bozorth *et al.*, Phys. Rev., **99** (1955), 1896.
19. D. Lax, Proc. I.R.E., **44** (1956), 1368.
20. A. M. Clogston, H. Suhl, L. R. Walker and P. W. Anderson, Phys. Rev., **101** (1956), 903.
21. A. M. Clogston, H. Suhl, L. R. Walker and P. W. Anderson, J. Phys. Chem. Solid, **1** (1956), 129.
22. L. Landau and E. Lifshitz, Phys. Z. Soviet Union, **8** (1935), 153.
23. F. Bloch, Phys. Rev., **70** (1946), 460.
24. N. Bloembergen, Phys. Rev., **78** (1950), 572.
25. S. Takemoto, Memoirs Coll. Sci. Kyoto Univ., **A28** (1958), 333.
26. J. C. Galt, J. A. Andrus, and H. G. Hopper, Rev. Mod. Phys., **25** (1953), 93.

Memoirs of the College of Science, University of Kyoto, Series A,
Vol. XXIX, No. 2, Article 4, 1959.

ON LOCAL CHARACTER OF POISSON'S RATIO IN THE EARTH'S CRUST

BY

Akira KAMITSUKI

(*Received February 4, 1959*)

ABSTRACT

Instead of the usual time-distance curve, the *P–S* diagram method is effectively employed to detect any area of anomalous value of Poisson's ratio, if existent, in the earth's crust. In the present article, the anomalous Poisson's ratio in the crust of Kyushu District is discussed in some detail, and it hints at the possibility of existence of local magmatic reservoir in the crust.

1. Introduction

It was found by the seismometric investigation that within the earth's crust, there exist two or more distinct layers which are characterized mainly by the seismic wave velocities. In the various regions of the world the seismic wave velocities transmitted through these layers, the thickness of each individual layer and the depth of the Mohorovičić discontinuity have been investigated. From the numerous results hitherto obtained, the earth's crust may be considered to have distinct local character.

Theoretically, the velocity of longitudinal wave V_p and the velocity of transverse wave V_s transmitted through the infinite homogeneous isotropic medium are related to the density and the elastic constants of the medium in the following forms:

$$V_p = \sqrt{\frac{k+\frac{4}{3}\mu}{\rho}} \quad \text{and} \quad V_s = \sqrt{\frac{\mu}{\rho}},$$

ρ being the density, and k and μ being the incompressibility and the rigidity of the medium respectively. The ratio of V_p to V_s is the function of the elastic constants only. Namely,

$$\frac{V_p}{V_s} = \sqrt{\frac{k+\frac{4}{3}\mu}{\mu}} = \sqrt{\frac{k}{\mu}+\frac{4}{3}} = \sqrt{1+\frac{1}{1-2\sigma}},$$

and

$$\sigma = \frac{1}{2}\left(1-\frac{1}{\left(\frac{V_p}{V_s}\right)^2-1}\right),$$

σ being Poisson's ratio. At relatively shallow depths σ is slightly less than 0.25 and

in the lower layers of the crust it is about 0.25, and in the deeper parts of the mantle about 0.30. Inside the core, σ seems to be close to 0.50 (**1, 2**). For example, various values of Poisson's ratio were found in some regions (**3, 4, 5, 6**). Some recent results are tabulated below (**7**).

The velocities of P- and S-waves, velocity ratio and Poisson's ratio in some regions.

Region	Author	V_p km/sec	V_s km/sec	V_p/V_s	σ	Depth km	Remarks
Quincy granite	Don Leet and Maurice Ewing	4.96 ± 0.02	2.48 ± 0.03	2.00	0.33	Very shallow	Using the waves generated by dynamite explosion.
Rockport granite	Don Leet	5.08 ± 0.01 5.14 ± 0.05	2.70 ± 0.02	1.90_4	0.31	Shallow	
Sudbury norite		6.22 ± 0.003	3.49 ± 0.006	1.78_3	0.27		
Southern California	B. Gutenberg	5.55	3.23	1.70	0.24	0–14	Natural earthquakes
		6.05	3.39	1.79	0.27	14 26	
		6.83	3.66	1.86	0.30	26–30	
		7.6	4.24	1.80	0.27	30–39	
		7.9_4	4.45	1.78	0.27	>39	
Europe	H. Jeffreys	P_g=5.57±0.02	S_g=3.36±0.01	1.65_8	0.215		Natural earthquakes
		P^*=6.50±0.03	S^*=3.74±0.03	1.73_8	0.252		
		P_n=7.76±0.03	S_n=4.36±0.02	1.78_0	0.269		
Southern California	B. Gutenberg	P=5.58±0.01	S=3.26	1.71_2	0.241		Natural earthquakes
		P_y=6.05	S_y=3.65	1.65_8	0.215		
		P_m=6.95±0.18	S_m=4.10	1.69_5	0.233		
		P_n=8.06±0.11	S_n=4.45	1.81_1	0.280		

The values of Poisson's ratio in the weathering or sedimentary layers are determined to be very much complex from the observation of artificial explosions. This should be investigated in the near future, but in the present state, it is rather a difficult problem as the generation and identification of S-waves in the artificial explosion are comparatively difficult (**8**). Setting aside the problem of sedimentary layer, Poisson's ratio of the earth's crust as a whole is considered to have a nearly constant value from 0.23 to 0.27 as seen in the annexed tables.

On the other hand, numerous experiments have been made for the comparison of elastic properties of rock with those obtained from the seismometric observations. Elastic constants obtained by the laboratory experiments have the diverse values (see, e.g. **9, 10, 11**), but it is recently ascertained by the experiment of high pressure and temperture that the standard errors of these diversities become smaller with the increase of pressure and temperature. The average values of pressure and temperature within the crust can be reproduced in the laboratory and the variation of elastic properties under high pressure and temperature are discussed.

Some recent data based on natural earthquakes and artificial explosion.

Region	Author	V_p km/sec			V_s km/sec			V_p/V_s			σ			Depth km		
Based on natural earthquakes.																
SW. Germany	Hiller (1953)	5.6	6.4	8.1	3.3	3.7	4.7	1.69_7	1.73_0	1.72_3	0.23_4	0.25_0	0.24_5	10～15	～30±	>30±
Italy, Cansiglio	Caloi (1952)	5.7	6.61	8.00	3.36	3.64	4.44	1.69_6	1.81_6	1.80_2	0.23_1	0.28_2	0.27_7	10～15	35	>35
Italy, NW Apennines	Caloi (1952)	5.25	6.63	8.16	3.06	3.57	4.44	1.71_5	1.85_7	1.83_8	0.24_4	0.29_1	0.29_0			
Italy, Gran Sasso	Fillippo and Marcelli (1952)	5.46	6.38	8.19	3.01	3.63		1.81_4	1.75_7		0.28_1	0.26_0		～25	60	>60
S. California	Richter and Nordquist (1951)		6.34			3.67	4.55		1.72_7	1.79_1		0.24_7	0.27_4			
S. California	Gutenberg (1951)		6.35	8.1～8.2		3.6	4.6_2		1.76_4	1.75_3～1.77_5		0.26_3	0.25_9～0.26_8	～28	～35	>35
Based on artificial explosions.																
Heligoland to S. Germany	Schulze and Förtsch (1950)	6.18	6.60	8.3	3.67	3.87	—	1.68_4	1.70_5	—	0.23	0.24	—	6～9	9～27	>27
Black Forest	Förtsch (1951)	5.9±	6.55	8.34	3.4±	3.78	4.82	1.73_5	1.73_3	1.73_0	0.25	0.25	0.25	0–15	15–31	>31
Black Forest	Rothé and Peterschmitt (1950)	5.97	6.54	8.15	3.4±	3.65	—	1.75_3	1.79_1	—	0.26	0.27	—	2～20	20～30	>30
*N. New York toward W. and S.	Katz (1953)		6.4	8.2±		3.62	4.68		1.76_8	1.75_2		0.27	0.26±		0–35	>35
*Pennsylvania	Katz (1953)		6.3	8.07		3.60	4.7–		1.75_0	1.71_7		0.26	0.24		0～36	>36
*Canadian Shield	Hodgson (1953)		6.1	8.21		3.61	4.69		1.69_0	1.75_0		0.22	0.26		1–32	>32
			6.25	8.18		3.54	4.85		1.76_6	1.68_6		0.26	0.23		0–36	>36
			6.23	7.06		3.54	3.92		1.76_0	1.80_1		0.26	0.28		0–28±	28–40
Japan	Research Group for explosion seismology (1951, 52, 54)	6.1–	7.4	8.2	3.4	—	—	1.79_4	—	—	0.28			1～27	27–32	>32
*W. Transvaal	Willmore, Hales and Gane (1952)		6.09	8.22～8.27		3.68	4.80～4.83		1.65_5	1.71_2		0.21	0.24		5～34	>34
		6.09	6.83	8.22～8.27	3.68	3.89	4.80～4.83	1.65_5	1.75_6	1.71_2	0.21	0.26	0.24	5～23	23–38	>38

(Note: In regions marked with an asterisk the structure calculated by the analysis of P-waves is different from that of S-waves.)

Taking account of the constancy of Poisson's ratio in a certain limited region, the $P\sim S$ durations may linearly increase with the arrival times of P-wave (**12**). This method is emoloyed to research the origin time of deep earthquakes (**13**). In recent years, Yoshiyama (**14**) investigated the value of V_p/V_s and found that at the Mohorovičić discontinuity it increases abruptly from 1.67 to 1.78.

In the present case, Poisson's ratio in the earth's crust is investigated using the seismic wave velocities of natural earthquakes, especially in relation to the local character of the earth's crust.

2. The method of *P*-*S* diagram

In order to find the values of V_p/V_s, especially their local anomaly, the P–S diagram method is effectively employed. In this case, the following must be reasonably assumed. Namely, each earthquake has only one origin time at the hypocenter, being common for P- and S-waves, and the hypocenter at which P- and S-waves are emitted has a negligibly small domain compared with those of the earth's crust to be investigated. In the P–S diagram, the arrival time of P-wave, T_p, is taken as abscissa and that of S-wave, T_s, as ordinate. Observed value obtained at one station corresponds to one point in this diagram. The velocity ratio of P-wave to S-wave is represented by the following formula:

$$\frac{V_p}{V_s}=\frac{T_s-T_0}{T_p-T_0},$$

where T_0 is the origin time at the hypocenter. The gradient of the straight line connecting the origin to each point directly represents the mean value of V_p/V_s along the seismic wave path between the hypocenter and each station. If some points show any particular or systematic deviations, those points represent immediately their local anomaly of V_p/V_s. Comparing this method with the time-distance curve method, the former has some merits as mentioned below.

1) In order to construct the time-distance curves, the position and depth of the hypocenter must be determined accurately and in this case some assumptions about the subterranean structure must necessarily be made. Moreover, the velocities must be estimated from these curves by the troublesome treatments. On the contrary, the P–S diagram method need not any assumption and treatment. The one time T_0 only should be computed, being easily determined by the graphical method. Speaking in detail, T_0 is given at the intersection of the mean straight line tentatively drawn through the observed points with the straight line of 45° gradient. The error which will be produced in the process of constructing the time-distance curves will be excluded and any local anomaly of Poisson's ratio in the earth's interior will be easily found out and checked immediately.

2) The absolute values of P- and S-wave velocities and the thickness of the earth's crust and others have no influence upon the results obtained by the P-S method, and so the P-S diagram method is more effectively and accurately applied compared with that of time-distance curves for the study of local character of the elastic properties of the earth's interior.

The value of V_p/V_s estimated by the present method is the mean one, being estimated along the seismic wave path from the hypocenter to each station and so it is necessary to determine through which layer the waves are transmitted. The P-S diagram method is more useful in such a case as many earthquakes of various focal depths are observed with high time accuracy. It should be remarked that the origin time at the hypocenter is assumed to be only one, as stated previously. Yashima (**15**) estimated the magnitude of the hypocentral region of an earthquake from the difference between two times, one being the origin time of P-wave in time-distance curve analysis, the other the time at which $P \sim S$ duration is zero. Though this is a very interesting problem, its discussion will be postponed to another opportunity.

3. Application of the P-S diagram method

As will be mentioned in the next section, some definite deviations in the P-S diagram were found in the Kyushu district. Reflecting upon this effect, the accuracy of arrival times of P- and S-waves must be carefully discussed. Recently the time correction in seismograms has become very accurate by using the J.J.Y.-time signal. In the case of P-wave, the identification of phase is easy and the measurement of arrival time is accurate if they are those of direct P-wave. According to this reason, most of the earthquakes investigated in the treatment are rather deep ones, foci of which are situated below the Mohorovičić discontinuity, and the few that are shallow are investigated in the distances ranging within about 100 km. In the case of S-wave, the identification and measurement must carefully be considered. Theoretically, the wave transformed from S-type to P-type at the Mohorovičić discontinuity may appear before the arrival of direct S-waves. But these transformed SP-wave are correctly and safely discriminated from the direct S-wave considering the time-distance and amplitude relation. The S-waves have generally larger amplitudes and periods than P-waves, and it may be probable that the arrival times of S-wave have errors of one or more seconds.

In the present case, the original seismograms at the observatories of Aso, Abuyama and Kamigamo were investigated and the copied ones at twenty-five stations of the Japan Meteorological Agency were examined concurrently.

4. Anomaly of Poisson's ratio in the Kyushu district

The twelve earthquakes which occurred in or near the Kyushu district were selected. The epicenters and observation stations are shown in Fig. 1, and tabulated in Table 1.

Table 1. The earthquakes used in section 4.

No.	Origin time					Epicenter			
		d	h	m	s	Location	Latitude	Longitude	Depth
									km
1	53 Jan.	23	11	47	59	Bungo Channel.	33.3°*N*	132.2°*E*	40
2	56 Oct.	5	19	34	11	*E* part of Oita Pref., Kyushu.	33.1	131.6	100 ca.
3	50 Sept.	16	21	48		*N* part of Miyazaki Pref., Kyushu.	32.7	131.5	110
4	54 Feb.	24	3	28	17	*SE* part of Miyazaki Pref., Kyushu.	31.8	130.9	30
5	58 May	15	5	32	3	Off *E* coast of Kyushu.	32.7_5	132.2	30
6	53 Nov.	27	4	25	55	Off *E* coast of Kyushu.	32.0	131.9	30
7	56 Sept.	7	7	45	28	Off *SE* coast of Kyushu.	31.0	132.0	40
8	51 Apr.	26	3	30		Off Satamisaki, Kagoshima Pref., Kyushu.	30.8	130.7	130
9	55 Mar.	28	18	12	20	Off *S* coast of Kyushu.	29.4	130.1	60 ca.
10	55 Apr.	17	10	13	32	Saga Pref., Kyushu.	33.3	130.1	0～10
11	58 June	19	22	49	48	*W* coast of Kyushu.	32.9	130.4	0～10
12	56 Nov.	2	20	34	22	*W* part of Setonaikai.	33.8	132.3	<30

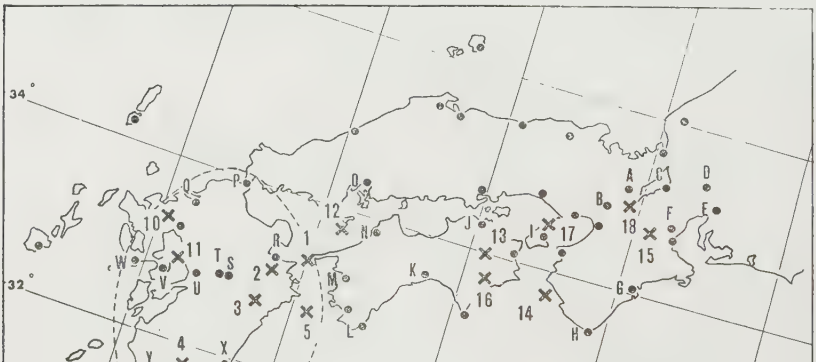

Fig. 1. The location of stations and epicenters.

Stations are as follows:

A: Kamigamo B: Abuyama C: Hikone D: Gifu E: Nagoya F: Kameyama
G: Owashi H: Shionomisaki I: Sumoto J: Takamatsu K: Kochi
L: Shimizu M: Uwazima N: Matsuyama O: Hiroshima P: Shimonoseki
Q: Fukuoka R: Oita S: Aso-san T: Aso-obs. U: Kumamoto V: Unzendake
W: Nagasaki X: Miyazaki Y: Kagoshima

Epicenters are listed in Tables 1 and 2.

Table of earthquake No. 1.
53 Jan. 23^d 11^h 47^m 59^s Bungo Channel.
(33.3°N, 132.2°E H=40 km)

	Station	P-wave		S-wave		Δ
		Phase	Time	Phase	Time	
			m s		m s	km
R	Oita	iP	48 10.3	iS	48 17.6	53.7
L	Shimizu	iP	13.7	iS	24.1	107.5
N	Matsuyama	iP	14.6	iS	25.7	81.5
T*	Aso-obs.	iP	16.3	iS	30.3	122.3
K	Kochi	iP	18.2	iS	31.2	127.9
P*	Shimonoseki	iP	18.3	iS	33.9	137.1
U*	Kumamoto	iP	19.5	iS	36.6	148.3
Q*	Fukuoka	iP	23.5	iS	43.2	172.4
X*	Miyazaki	eP	24.1	iS	44.0	166.8
J	Takamatsu	eP	29.6	iS	50.9	205.7
W*	Nagasaki	P	30.8	S	57.4	226.1
Y*	Kagoshima	P	35.9	S	49 8.3	246.5

Note: In the tables of earthquakes No. 1～No. 9 the stations marked with an asterisk have their deviations in the P–S diagram.

Table of earthquake No. 2.
56 Oct. 5^d 19^h 34^m 11^s E part of Oita Pref., Kyushu.
(33.1° N, 131.6 E H=100 km ca.)

	Station	P-wave		S-wave		Δ
		Phase	Time	Phase	Time	
			m s		m s	km
R*	Oita	eP	34 26.9	iS	34 36.6	14.8
T*	Aso-obs.	iP	29.5	iS	41.1	61.2
M*	Uwajima	eP	31.1	eS	44.4	90.8
U*	Kumamoto	iP	31.7	iS	44.8	87.1
*	Saga	iP	34.2	iS	49.6	122.3
L*	Shimizu	eP	34.3	iS	50.4	135.3
Q*	Fukuoka	iF	35.1	iS	51.1	124.2
X*	Miyazaki	iF	36.2	iS	52.7	111.2
N	Matsuyama	eP	38.6	iS	55.7	105.6
K	Kochi	iP	41.2	eS	35 1.4	187.2
	Murotomisaki	eP	47.8	eS	13.5	242.8
J	Takamatsu	eP	50.1	iS	16.3	265.0
	Tokushima	iP	53.9	eS	22.6	296.5
*	Yaku-shima	eP	55.4	eS	30.1	309.5
I	Sumoto	eP	59.5	iS	31.4	337.3

Table of earthquake No. 3.
50 Sept. 16^{d} 21^{h} 48^{m} *N* part of Miyazaki Pref., Kyushu.
(32.7°*N*, 131.5°*E* *H*=110 km)

	Station	*P*-wave		*S*-wave		Δ
		Phase	Time	Phase	Time	
			m s		m s	km
*U**	Kumamoto	*P*	49 2.6	*S*	49 17.5	74.1
*	Saga	*P*	4.7	*S*	22.8	127.9
X	Miyazaki	*iP*	6.0	*iS*	20.9	85.2
*Q**	Fukuoka	*iP*	6.1	*iS*	23.8	127.9
*Y**	Kagoshima	*iP*	4.0	*iS*	22.4	153.8
*L**	Shimizu	*iP*	8.1	*iS*	27.4	140.8
*P**	Shimonoseki	*P*	9.3	*S*	28.5	148.3
*N**	Matsuyama	*P*	11.2	*S*	32.8	176.1
*O**	Hiroshima	*P*	13.2	*iS*	36.0	203.8
K	Kochi	*P*	16.1	*S*	38.7	211.3
*	Izuhara	*P*	17.5	*S*	45.8	263.2
*	Tomie	*P*	18.9	*S*	45.7	255.8
*	Yoku-shima	*P*	19.2	*S*	46.9	265.0
	Murotomisaki	*P*	21.1	*S*	48.2	257.6
	Himeji	*P*	36.4	*S*	50 14.1	379.9
H	Shionomisaki	*iP*	38.7	*iS*	19.4	405.9
	Kobe	*P*	39.6	*S*	20.8	405.9
	Osaka	*P*	43.3	*S*	26.3	431.8
F	Kameyama	*eP*	52.7	*eS*	43.9	518.8
C	Hikone	*P*	55.2	*S*	47.9	522.5

Table of earthquake No. 4.
54 Feb. 24^{d} 3^{h} 28^{m} 17^{s} *SE* part of Miyazaki Pref., Kyushu.
(31.8°*N*, 130.9°*E* *H*=30 km ca.)

	Station	*P*-wave		*S*-wave		Δ
		Phase	Time	Phase	Time	
			m s		m s	km
X	Miyazaki	*iP*	28 28.0	*iS*	28 33.5	59.3
*Y**	Kagoshima	*eP*	29.3	*S*	39.0	40.8
*U**	Kumamoto	*iP*	35.8	*S*	50.8	114.9
*T**	Aso-obs.	*iP*	36.4	*iS*	52.2	120.5
*R**	Oita	*iP*	44.5	*eS*	29 6.9	174.2
	Yaku-shima	*P*	46.6	*S*	5.4	152.0
*Q**	Fukuoka	*eP*	49.2	*S*	11.8	203.8
*P**	Shimonoseki	*iP*	49.7	*S*	18.3	239.1
L	Shimizu	$eP_{\text{初}}$	53.2	S_{NE}	16.3	224.3
*	Tomie	*iP*	56.5	*S*	25.2	220.5
*N**	Matsuyama	*eP*	59.9	*iS*	32.9	289.1
*	Izuhara	*P*	29 4.7	*S*	43.8	305.8
*O**	Hiroshima	*eP*	6.—	*eS*	44.—	318.8
K	Kochi	*eP*	9.0	*eS*	41.4	315.0

Table of earthquake No. 5.

58 May 15^d 5^h 32^m 3^s Off *E* coast of Kyushu. ($32.7_5°N$, $132.2°E$ H=30 km)

	Station	*P*-wave Phase	*P*-wave Time	*S*-wave Phase	*S*-wave Time	Δ
			m s		m s	km
	Sukumo	*P*	32 17.0	*S*	32 23.0	50.0
*L**	Shimizu	*iP*	19.2	*S*	28.0	72.3
*R**	Oita	iP_Z	20.1	eS_{EZ}	30.0	76.0
*X**	Miyazaki	*P*	23.9	*S*	37.2	103.8
*S**	Aso-san	iP_E	25.3	S_N	40.4	105.6
*T**	Aso-obs.	*iP*	25.8	*iS*	41.4	113.0
N	Matsuyama	iP_E	26.6	eS_E	41.4	133.4
U	Kumamoto	iP_Z	31.4	*S*	49.1	139.0
K	Kochi	*iP*	34.4	*iS*	55.3	152.0
*P**	Shimonoseki	eP_N	34.4	eS_N	56.7	177.9
	Murotomisaki	*eP*	41.9	*iS*	33 8.4	194.6
J	Takamatsu	*eP*	46.5	*eS*	16.8	244.6

Table of earthquake No. 6.

53 Nov. 27^d 4^h 25^m 55^s Off *E* coast of Kyushu. ($32.0°N$, $131.9°E$ H=30 km)

	Station	*P*-wave Phase	*P*-wave Time	*S*-wave Phase	*S*-wave Time	Δ
			m s		m s	km
*X**	Miyazaki	*iP*	26 3.3	*S*	26 8.3	50.0
*S**	Aso-san	*iP*	16.4	*S*	30.9	127.9
*L**	Shimizu	iP_{NE}	16.6	*S*	32.1	137.1
*T**	Aso-obs.	*iP*	17.1	*iS*	33.2	133.4
*Y**	Kagoshima	*iP*	17.9	*S*	35.2	129.7
*U**	Kumamoto	iP_Z	18.5	*S*	35.9	148.3
*R**	Oita	*eP*	19.4	*S*	39.1	144.6
*V**	Unzendake	*P*	20.9	*S*	42.3	177.9
	Yaku-shima	*eP*	25.7	*S*	42.8	215.0
*Q**	Fukuoka	*iP*	28.7	*S*	56.3	229.8

Table of earthquake No. 7.

56 Sept. 7^d 7^h 45^m 28^s Off *SE* coast of Kyushu. ($31.0°N$, $132.0°E$ H=40 km)

	Station	*P*-wave Phase	*P*-wave Time	*S*-wave Phase	*S*-wave Time	Δ
			m s		m s	km
*X**	Miyazaki	P_Z	45 47.5	*S*	46 0.9	133.4
*Y**	Kagoshima	*P*	52.6	*eS*	11.4	152.0
	Yaku-shima	*P*	53.4	*S*	9.6	155.7
L	Shimizu	eP_{NE}	46 1.8	*eS*	22.9	220.5
*U**	Kumamoto	*eP*	2.7	*S*	32.3	235.4
*S**	Aso-san	eP_E	3.8	S_E	31.6	226.1
*T**	Aso-obs.	*iP*	4.7	S_Z	33.1	229.8
*W**	Nagasaki	eP_N	7.2	eS_N	34.0	278.0
*Q**	Fukuoka	eP_Z	14.4	S_E	49.6	324.3
N	Matsuyama	eP_E	17.8	eS_N	50.8	326.2

Table of earthquake No. 8.
51 Apr. 26^{d} 3^{h} 30^{m} Off Satamisaki, Kagoshima Pref., Kyushu.
(30.8°N, 130.7°E H=130 km)

	Station	P-wave		S-wave		Δ
		Phase	Time	Phase	Time	
			m s		m s	km
	Yaku-shima	P	31 25.3	S	31 41.6	53.7
Y	Kagoshima	iP	25.5	iS	41.8	87.1
X	Miyazaki	iP	29.4	iS	48.6	144.6
V*	Unzendake	iP	32.2	iS	55.9	218.7
W*	Nagasaki	iP	32.3	iS	55.4	228.0
U*	Kumamoto	P	33.6	S	58.1	224.2
R*	Oita	P	39.3	S	32 9.3	283.6
Q*	Fukuoka	P	41.5	S	12.2	311.3
P*	Shimonoseki	P	46.4	S	19.8	350.3
N*	Matsuyama	P	50.0	S	27.5	387.3
K	Kochi	P	55.2	S	33.3	405.9
	Murotomisaki	P	58.5	S	40.6	426.2
*	Hamada	P	32 0.2	S	46.9	472.5
J	Takamatsu	iP	7.6	iS	54.9	500.3
I	Sumoto	P	13.5	S	33 6.7	555.9
	Osaka	P	23.2	S	23.1	622.6
	Toyooka	P	24.3	S	25.3	650.4
B	Abuyama	eP	24.5	iS	26.2	641.1

Table of earthquake No. 9.
55 Mar. 28^{d} 18^{h} 12^{m} 20^{s} Off S coast of Kyushu.
(29.4°N, 130.1°E H=60 km ca.)

	Station	P-wave		S-wave		Δ
		Phase	Time	Phase	Time	
			m s		m s	km
	Yaku-shima	iP	12 40.5	iS	12 53.0	124.2
Y*	Kagoshima	iP	55.7	S	13 23.3	246.5
X*	Miyazaki	iP	13 3.9	iS	38.6	326.2
*	Tomie	$P_{明}$	9.6	$S_{明}$	57.2	379.9
W*	Nagasaki	eP	11.8	iS	57.6	370.7
V*	Unzendake	P	13.3	$S_{明}$	52.3	370.7
U*	Kumamoto	iP	14.4	iS	58.0	385.5
S*	Aso-san	P	16.5	S	14 3.7	398.5
R*	Oita	iP_{N}	21.7	$iS_{明}$	11.7	450.3
Q*	Fukuoka	iP	25.6	S	19.7	465.1
L	Shimizu	$eP_{N明}$	26.1	eS	8.0	465.1
P*	Shimonoseki	iP	32.4	S	26.8	511.4
N*	Matsuyama	P	34.9	S	31.2	555.9
K	Kochi	eP	35.9	eS	30.4	565.2
O*	Hiroshima	eP	39.3	eS_{Z}	38.4	594.8
*	Hamada	eP	44.1	eS	58.1	639.3
J	Takamatsu	eP	49.5	S	51.8	796.8

Table of earthquake No. 10.
55 Apr. 17^d 10^h 13^m 32^s Saga Pref., Kyushu.
($33.3°N$, $130.1°E$ $H=0\sim10$ km)

	Station	P-wave		S-wave		Δ
		Phase	Time	Phase	Time	
			m s		m s	km
Q	Fukuoka	iP	13 40.5	iS	13 44.8	40.8
V	Unzendake	iP	43.9	eS	53.1	64.9
	Saga	iP_N	44.1	iS_N	47.0	18.5
W	Nagasaki	iP_Z	44.4	iS_Z	53.0	66.7
U	Kumamoto	iP_Z	47.2	iS	2.0	77.8
P	Shimonoseki	iP	50.9	S	2.0	105.6
S	Aso-san	P	52.5	S	4.1	103.8
	Izuhara	iP	55.1	S_N	8.4	124.2
	Tomie	iP	59.5	S	18.4	146.4
R	Oita	eP_N	14 0.1	eS_{EW}	14.9	140.8
X	Miyazaki	P_Z	7.9	S_Z	35.9	181.6
Y	Kagoshima	P_N	12.7	S^N	39.0	194.6

Table of earthquake No. 11.
58 June 19^d 22^h 49^m 48^s W coast of Kyushu.
($32.9°N$, $130.4°E$ $H=0\sim10$ km)

	Station	P-wave		S-wave		Δ
		Phase	Time	Phase	Time	
			m s		m s	km
V	Unzendake	iP	49 56.7	S	49 59.4	24.1
U	Kumamoto	iP	57.9	S	50 2.4	31.5
	Saga	iP	58.1	iS	2.2	38.9
W	Nagasaki	iP	59.9	iS	6.7	51.9
S	Aso-san	iP	50 2.5	S	9.9	64.9
Q	Fukuoka	iP_Z	2.8	S_Z	10.6	76.0
P	Shimonoseki	iP	11.4	iS_N	24.9	126.0
R	Oita	iP_Z	11.4	eS_{NEW}	27.8	120.5
X	Miyazaki	P_Z	15.7	S	34.0	129.7
Y	Kagoshima	P	16.3	eS	35.3	146.4
	Tomie	P_Z	16.3	S_{NZ}	35.6	157.5
	Izuhara	eP_{NEW}	16.7	iS_N	37.9	176.1

Table of earthquake No. 12.
56 Nov. 2^d 20^h 34^m 22^s W part of Setonaikai.
($33.8°N$, $132.3°E$ $H=30$ km)

	Station	P-wave		S-wave		Δ
		Phase	Time	Phase	Time	
			m s		m s	km
N	Matsuyama	iP_{EW}	34 32.1	iS_{EW}	34 39.1	44.5
	Uwajima	iP	34.1	iS	42.0	66.7
O	Hiroshima	P	35.8	S	44.8	64.9
R	Oita	iP_Z	38.1	eS_{EW}	47.9	88.9
	Sukumo	eP	38.3	S	45.3	103.8
K	Kochi	iP	40.9	iS	52.8	116.8
L	Shimizu	eP	41.0	eS	57.4	127.9
T	Aso-obs.	iP / i	48.3 / 49.0	iS	35 4.9	157.5

(Note: At Aso the refracted wave is observed 0.7 sec before the direct wave.)

Most of these earthquakes have the foci situated below the Mohorovičić discontinuity. Three earthquakes Nos. 10, 11 and 12 are shallow ones.

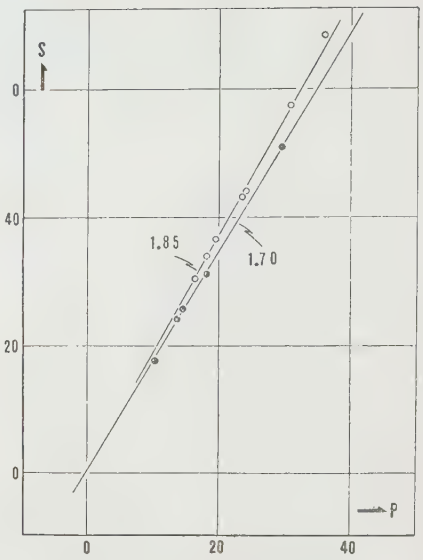

Figure for erathquake No. 1.

No. 1) In the P–S diagram, the points are separated into two groups. The lower group points are of the stations situated eastward from the epicenter (Shikoku and Chugoku districts) and upper group points are all of the stations situated west- and southwestward (Kyushu district). The lower group poitns are arrayed nearly on a straight line, the gradient of which is calculated as 1.70, being the normal value of V_p/V_s for the focal depth 40 km. The upper group points deviate upward from this straight line, thus representing the anomalously large value of V_p/V_s of nearly 1.85. The phases of P- and S-waves are tabulated in Table (No. 1) and it is favourable that all are sharp iP and iS.

Furthermore, the amplitudes and periods of P- and S-waves are measured. As

The amplitude ratio of S-wave to P-wave and their half periods.

	Station	Amplitude ratio $\frac{S}{P}$	Half period	
			P-wave	S-wave
R	Oita	1.2 (V)	0.4 (V)	0.3 (V)
L	Shimizu	50.0 (V)	0.5 (V)	0.5 (V)
N	Matsuyama	3.7 (V)	0.6 (N) 0.7 (E)	0.4 (V) 0.7 (N) 0.7 (E)
T	Aso-obs.	3.0 (V)	0.4 (V)	0.6 (V)
K	Kochi	10.0 (V)	0.6 (V) 0.7 (N) 0.7 (E)	0.5 (V) 0.7 (N) 0.7 (E)
P	Shimonoseki	——	0.3 (N) 0.2 (E)	0.2 (N) 0.3 (E)
U	Kumamoto	——	0.7 (N) 0.8 (E)	0.8 (N) 0.8 (E)
Q	Fukuoka	2.2 (V)	0.4 (V) 0.3 (E)	1.0 (V) 0.4 (E)
X	Miyazaki	12.5 (V)	0.2 (V)	0.4 (V)
J	Takamatsu	20.0 (V)	0.9 (N)	1.0 (N)
Y	Kagoshima	6.2 (V)	0.9 (V)	0.9 (V)

the general tendency, the amplitude ratio of S-wave to P-wave and the period of S-phase seem to be slightly larger concerning to the upper group points than to the lower group ones. As this problem is very essential in nature, a detailed study will be made after collection of exact data concerning suitable earthquakes.

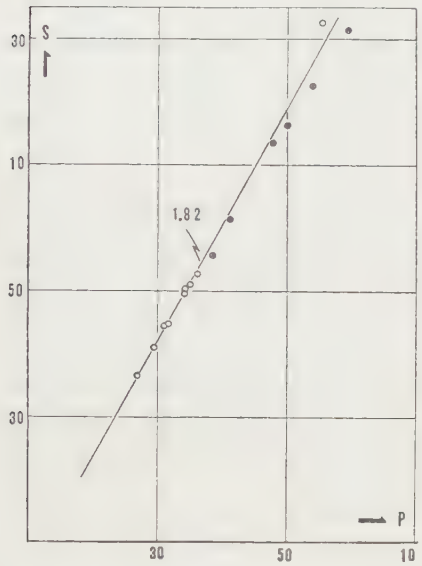

Figure for earthquake No. 2.

The seismograms recorded at Matsuyama and Kumamoto are shown in Figs. 2 and 3.

No. 2) The epicenter is situated on land in Kyushu. The value of V_p/V_s is calculated as 1.82 by drawing a straight line through the six stations in Kyushu and of Uwajima, Shimizu and Yaku-shima. The points of other stations deviate downward from this straight line.

No. 3) The epicenter of this earthquake is situated also on land. Excluding the points of stations in and near Kyushu, remaining points are arrayed on a straight line, the gradient of which is 1.76, being normal value for the focal depth of 110 km.

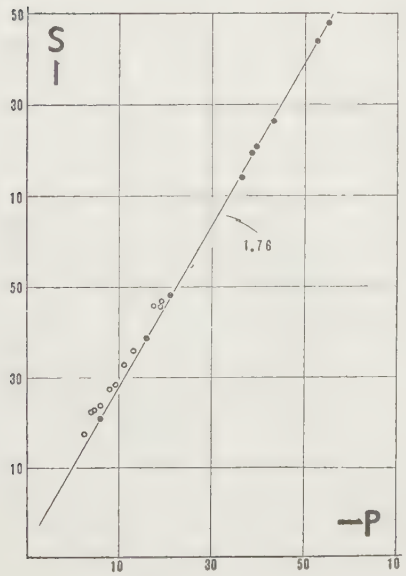

Figure for earthquake No. 3.

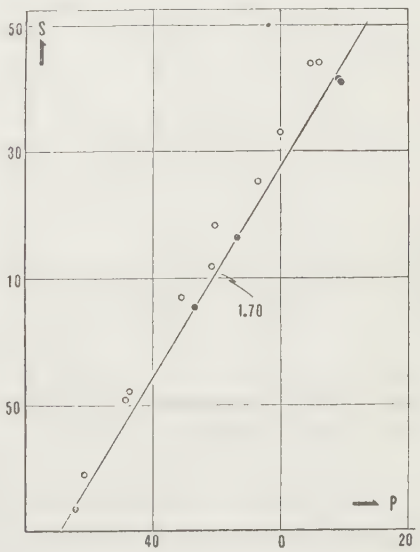

Figure for earthquake No. 4.

No. 4) The epicenter is situated more southward and the focal depth is shallower than that of No. 3. A straight line whose gradient is 1.70 is tentatively drawn. The points of stations in the Kyushu district deviate largely upward and the other points deviate downward.

No. 5) The epicenter is situated off the E coast of Kyushu. The mean straight line is drawn through the points of stations in and near Kyushu. The gradient of 1.83 is anomalously large for the focal depth of 30 km. The points of stations in Shikoku deviate downward.

No. 6) The epicenter is situated also off the E coast of Kyushu and more southward than that of No. 5. The mean straight line is drawn through the points of stations in Kyushu. The gradient of 1.86 is anomalously large for the focal depth of 30 km.

Because of the scantiness of nearer stations, drawing of time-distance curve is difficult. In the cases of earthquakes Nos. 4, 5 and 6, the apparent velocity is approximately 7 km/sec up to the distances of about 200 km, indicating that the focus is situated in the lower layer of the crust. At further distances the time-distance curve is largely diversed.

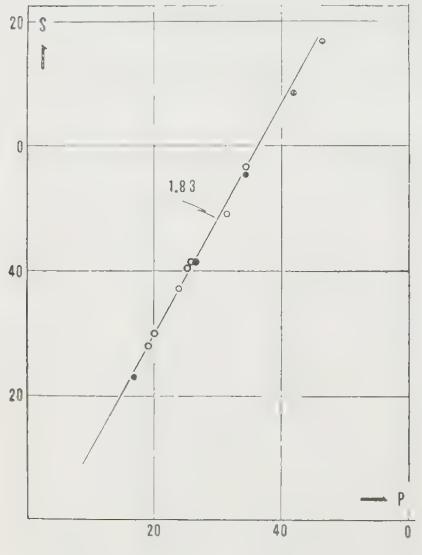

Figure for earthquake No. 5.

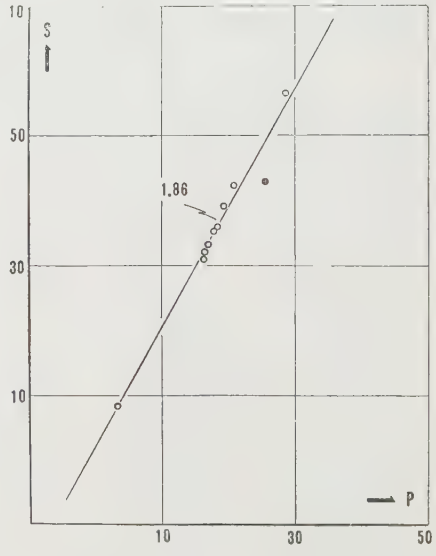

Figure for earthquake No. 6.

No. 7) The epicenter is situated more southward than that of No. 6 and below the Mohorovičić discontinuity. The points of stations in Kyushu deviate upward from the mean straight line whose gradient is 1.70.

No. 8) The epicenter of this earthquake is situated near off the *S* coast of Kyushu and the focal depth is 130 km. Excluding the points of stations in and near Kyushu, a straight line is drawn through the remaining points, its gradient being 1.76.

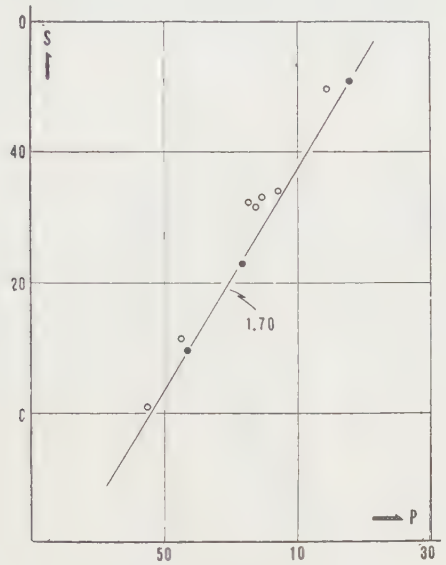

igure for earthquake No. 7.

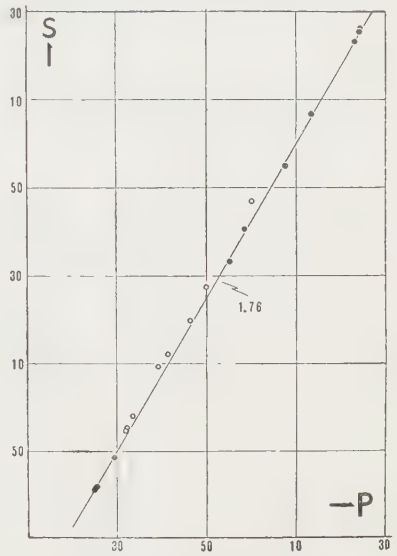

Figure for earthquake No. 8.

No. 9) The epicenter is situated far off the *S* coast of Kyushu and the focal depth is 60 km ca. The points deviate upward at first and then gradually return to the mean straight line, its gradient being 1.75.

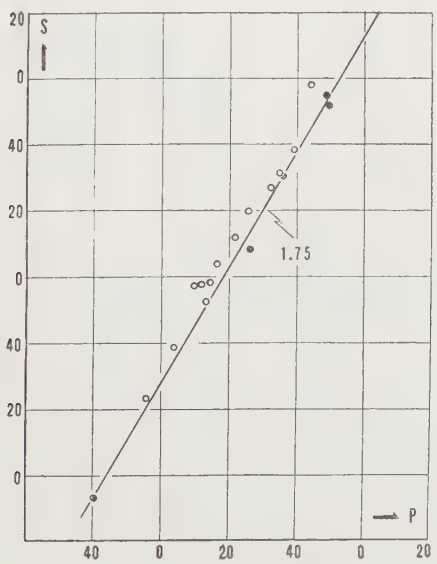

Figure for earthquake No. 9.

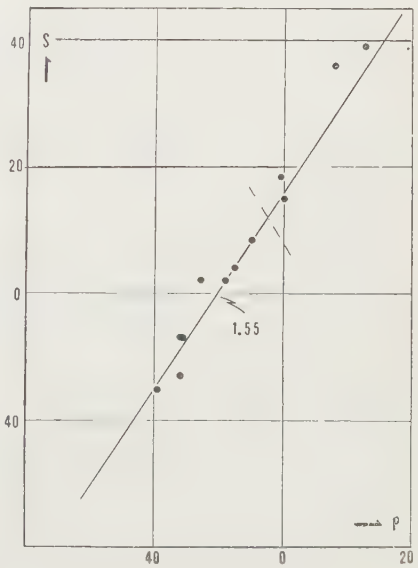

Figure for earthquake No. 10.

Nos. 10, 11 and 12) These earthquakes are shallow ones. Through the points of stations at the distances within about 100 km the mean straight lines are drawn. Their gradients are 1.55, 1.68 and 1.55 respectively. These values are normal for the shallow earthquakes whose foci are situated in the upper layer of the earth's crust.

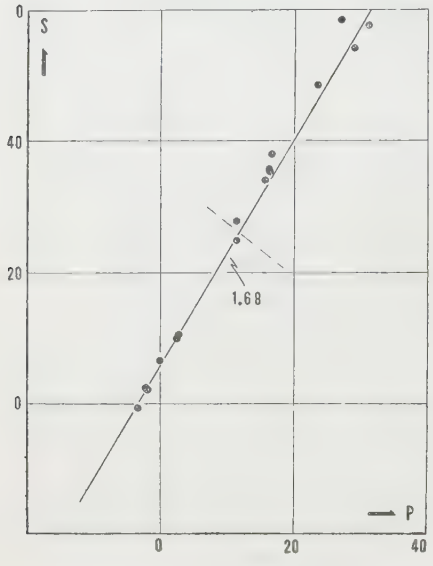

Figure for earthquake No. 11.

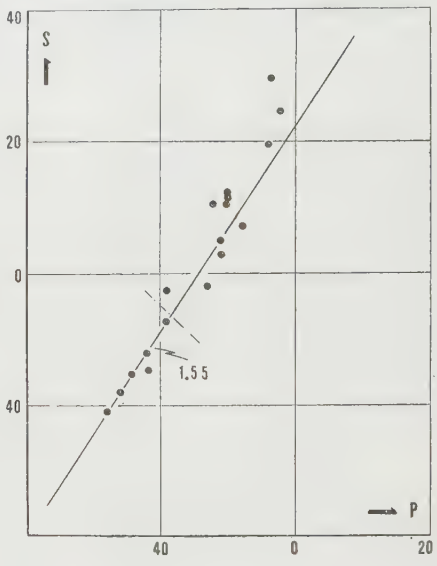

Figure for earthquake No. 12.

The values of V_p/V_s estimated in such a manner as mentioned above are compared with those of earthquakes discussed in the following sections and it is found that the points of the stations in and near the Kyushu district must be excluded owing to their deviation from the mean straight line and the correlation of the value of V_p/V_s to the focal depth is valid.

Putting together the results obtained above, the anomaly of the value of V_p/V_s, namely Poisson's ratio in the Kyushu district including the sea parts off the E and SE coast of Kyushu, is clarified. The horizontal contour of anomalous region is roughly represnted by the chain line shown in Fig. 1. The shallow earthquakes do not show any anomalous effect. The earthquakes whose foci are situated in the lower layer of the crust and immediately below the Mohorovičić discontinuity show the anomalously large values of V_p/V_s and rather deeper ones a little larger value. After all, the upper and lower boundaries of the domain in which Poisson's ratio is anomalously large are roughly estimated to be situated at depths from about 20 km and 40 km.

5. Poisson's ratio obtained in the Shikoku, Chugoku and Kinki districts.

The investigations by the same method are carried out in the adjacent region and the anomaly of Poisson's ratio found in the Kyushu district will be more clarified. The earthquakes used are tabulated in Table 2 and shown in Fig. 2.

Table 2. The earthquakes used in section 5.

No.	Origin time						Epicenter			
							Location	Latitude	Longitude	Depth
			d	h	m	s		°N	°E	km
13	57	Nov.	14	22	29	9	*E* part of Shikoku.	34.0	134.2	40
14	55	Dec.	18	15	27	42	Kii Channel, *W* Honshu.	33.7_5	135.1	40~50
15	57	Nov.	27	14	24	47	*NW* part of Mie Pref., *W* Honshu.	34.7	136.2	70
16	56	July	18	0	42	37	*S* part of Tokushima Pref., Shikoku.	33 3/4	134 1/4	0~10
17	58	June	17	16	20	12	Awaji-shima, *W* Honshu.	34.5	134.9	0~10
18	54	Dec.	21	19	31	58	Near Kyoto, *W* Honshu.	35.1	135.7	<20

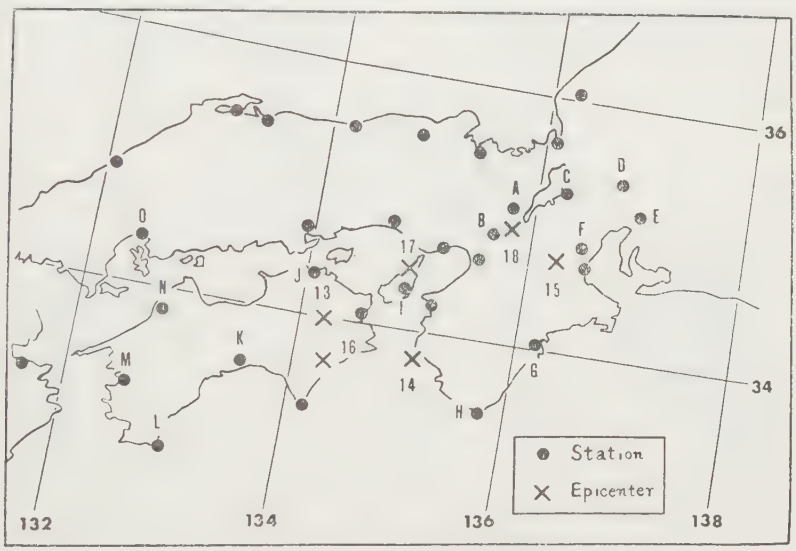

Fig. 2. The location of stations and epicenters:
Stations are as follows:
A: Kamigamo B: Abuyama C: Hikone D: Gifu E: Nagoya F: Kameyama
G: Owashi H: Shionomisaki I: Sumoto J: Takamatsu K: Kochi
L: Shimizu M: Uwazima N: Matsuyama O: Hiroshi
Epicenters are listed in Table 2.

In these regions, no conspicuous anomaly can be found. All points in the *P*-*S* diagrams are arrayed on a straight line within the time accuracy. The obtained values of V_p/V_s are 1.74, 1.76 and 1.75 in the cases of earthquakes Nos. 13, 14 and 15 respectively, whose foci are situated immediately below the Mohorovičić discontinuity. And in the cases of shallow earthquakes Nos. 16, 17 and 18, the values of V_p/V_s are 1.70, 1.68 and 1.70 respectively.

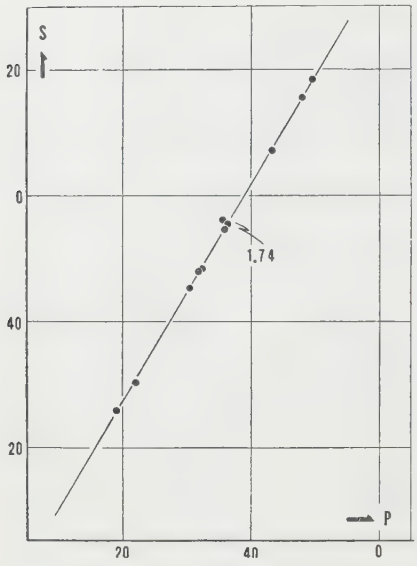

Figure for earthquake No. 13.

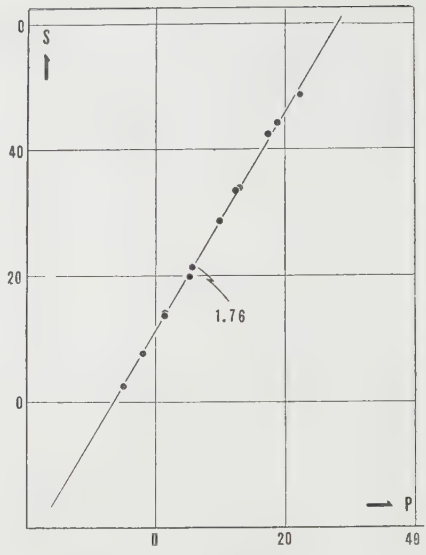

Figure for earthquake No. 14.

Table of earthquake No. 13.
57 Nov. 14^d 22^h 29^m 9^s E part of Shikoku.
($34.0°N$, $134.2°E$ H=40 km)

	Station	P-wave Phase	P-wave Time	S-wave Phase	S-wave Time	Δ
			m s		m s	km
J	Takamatsu	*iP*	29 19.1	*iS*	29 25.9	37.1
I	Sumoto	*iP*	22.1	*iS*	30.3	76.0
N	Matsuyama	*P*	30.5	*S*	45.3	131.6
H	Shionomisaki	*iP*	31.9	*iS*	48.0	157.5
B	Abuyama	*iP*	32.5	*S*	48.4	157.5
O	Hiroshima	*eP*	35.9	*eS*	54.6	166.8
A	Kamigamo	*iP*	36.4	*iS*	55.5	187.2
G	Owashi	*eP*	35.7	*iS*	56.2	185.3
C	Hikone	*iP*	43.3	*S*	30 7.1	235.4
D	Gifu	*eP*	48.0	*iS*	15.5	283.6
E	Nagoya	*iP*	49.6	*iS*	18.5	285.4

Table of earthquake No. 14.
55 Dec. 18^d 15^h 27^m 42^s Kii Channel, W Honshu.
($33.7_5°N$, $135.1°E$ H=40～50 km)

	Station	P-wave Phase	P-wave Time	S-wave Phase	S-wave Time	Δ
			m s		m s	km
I	Sumoto	*iP*	27 55.1	*iS*	28 2.6	66.7
H	Shionomisaki	*iP*	58.1	*iS*	7.7	70.4
G	Owashi	*iP*	28 1.4	*iS*	13.7	107.5
J	Takamatsu	*iP*	1.4	*iS*	14.1	114.9
A	Kamigamo	iP_{NS}	5.3	iS_{NS}	19.8	159.4
K	Kochi	*iP*	5.7	*iS*	21.3	146.4
F	Kameyama	*iP*	9.9	*iS*	28.6	176.1
C	Hikone	*iP*	12.4	*iS*	33.4	200.1
N	Matsuyama	*iP*	13.0	*iS*	33.8	215.0
E	Nagoya	*eP*	17.4	*eS*	42.3	233.5
O	Hiroshima	*iP*	18.8	*iS*	44.2	255.8
	Fukui	*iP*	22.4	*S*	48.6	276.1

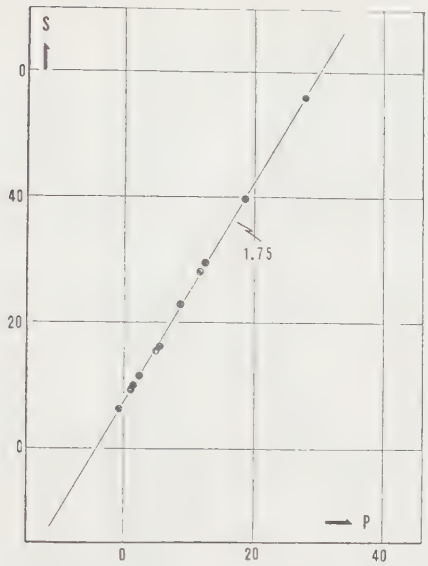

Figure for earthquake No. 15.

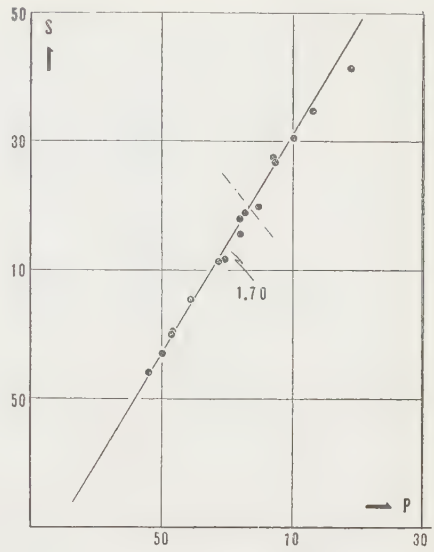

Figure for earthquake No. 16.

Table of earthquake No. 15.
57 Nov. 27^{d} 14^{h} 24^{m} 47^{s} *NW* part Mie Pref., *W* Honshu.
(34.7°*N*, 136.2°*E* *H*=70 km)

Station		*P*-wave		*S*-wave		Δ
		Phase	Time	Phase	Time	
			m s		m s	km
F	Kameyama	*iP*	24 59.3	*iS*	25 6.3	29.6
A	Kamigamo	*iP*	25 1.2	*iS*	9.4	57.4
B	Abuyama	*iP*	1.5	*iS*	10.0	61.2
C	Hikone	*iP*	2.4	*iS*	11.5	64.9
E	Nagoya	*eP*	5.0	*iS*	15.4	87.1
D	Gifu	*iP*	5.4	*iS*	16.1	94.5
I	Sumoto	*iP*	8.7	*iS*	22.8	124.2
H	Shionomisaki	iP_{E}	11.7	*iS*	28.1	144.6
	Fukui	*iP*	12.5	*iS*	29.4	150.1
J	Takamatsu	*iP*	18.7	*S*	39.6	202.0
K	Kochi	*eP*	27.9	*iS*	55.9	278.0
N	Matsuyama	*iP*	34.0	*iS*	26 6.5	328.0
O	Hiroshima	eP_{E}	36.7	*iS*	12.0	348.4

Table of earthquake No. 16.
56 July 18^{d} 0^{h} 42^{m} 37^{s} *S* part of Tokushima Pref., Shikoku.
(33 3/4°*N*, 134 1/4°*E* *H*=0～10 km)

Station		*P*-wave		*S*-wave		Δ
		Phase	Time	Phase	Time	
			m s		m s	km
	Tokushima	*iP*	42 48.2	*iS*	42 54.1	46.3
	Murotomisaki	*eP*	50.2	*iS*	57.0	55.6
J	Takamatsu	iP_{N}	51.6	*iS*	43 0.0	48.2
K	Kochi	*iP*	51.8	*iS*	0.5	70.4
I	Sumoto	*P*	54.5	*iS*	5.4	88.9
	Okayama	*eP*	58.8	*iS*	11.4	107.5
	Wakayama	*eP*	59.7	*eS*	11.7	100.1
N	Matsuyama	*iP*	43 1.9	eS_{Π}	17.9	135.3

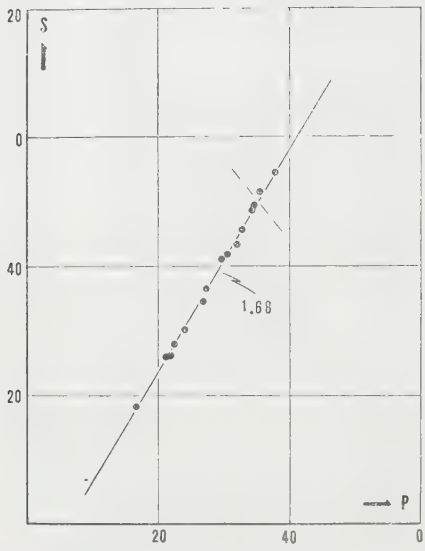

Figure for earthquake No. 17.

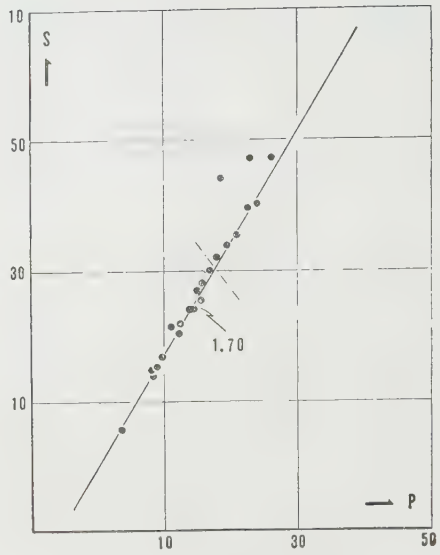

Figure for earthquake No. 18.

Table of earthquake No. 17.

58 June 17^{d} 16^{h} 20^{m} 12^{s} Awaji-shima, *W* Honshu.
(34.5°*N*, 134.9°*E* *H*=0~10 km)

	Station	*P*-wave		*S*-wave		Δ
		Phase	Time	Phase	Time	
			m s		m s	km
I	Sumoto	iP_{NE}	20 16.7	iS_{NEZ}	20 18.3	18.5
	Kobe	eP_{NEZ}	21.2	iS_{NEZ}	26.0	33.4
	Wakayama	iP	21.9	iS	26.2	38.9
	Himeji	iP_{NE}	22.5	iS_{NE}	28.0	40.8
	Tokushima	iP	24.1	iS	30.2	57.4
	Osaka	iP	26.9	iS	34.5	59.3
J	Takamatsu	iP	27.3	iS	36.5	81.5
	Okayama	iP	29.7	eS	41.1	92.6
	Nara	eP	30.6	iS	41.8	94.5
	Kyoto	eP	32.0	S	43.3	96.4
A	Kamigamo	iP_Z	32.8	iS_Z	45.7	100.1
	Toyooka	P_{NEZ}	34.3	iS_{NEZ}	48.6	105.6
	Maizuru	iP	34.7	iS	49.4	116.8
G	Owashi	P_{NE}	35.5	S_{NE}	51.4	127.9
H	Shionomisaki	eP_Z	37.8	eS_Z	54.4	142.7

Table of earthquake No. 18.

54 Dec. 21^d 19^h 31^m 58^s Near Kyoto, *W* Honshu.

(35.1°*N*, 135.7°*E* *H*=20 km)

	Station	*P*-wave		*S*-wave		Δ
		Phase	Time	Phase	Time	
			m s			km
	Kyoto	*eP*	32 3.7	*iS*	5.7	9.6
C	Hikone	*P*	7.9	*iS*	14.9	54.5
	Osaka	*eP*	8.2	*iS*	14.8	52.2
	Nara	*iP*	8.4	*iS*	13.6	47.9
	Maizuru	*iP*	8.9	*iS*	15.3	50.0
	Kobe	*eP*	9.8	*iS*	16.8	65.9
	Ibukiyama	eP_N	11.2	iS_N	21.6	69.7
	Tsuruga	*P*	12.3	*iS*	20.4	69.6
F	Kameyama	*iP*	12.6	*iS*	21.9	75.1
	Tsu	*P*	13.9	*S*	24.2	86.6
	Himeji	*iP*	14.6	$iS_{\text{扫}}$	24.2	95.6
	Wakayama	*eP*	15.1	*eS*	27.1	107.7
	Toyooka	*eP*	15.7	*iS*	25.6	93.8
I	Sumoto	*P*	15.8	*iS*	28.2	111.0
D	Gifu	*P*	17.0	*S*	30.0	102.7

6. Poisson's ratio obtained in other districts

The estimations of Poisson's ratio are carried out in other districts. Some earthquakes tabulated below are examined. The data of the second earthquake are those observed by S. Omote (**16**). The epicenter of the third earthquake is located near Yakedake Volcano in central Honshu.

Origin Time	Location of Epicenter	Focal Depth	V_p/V_s
57 Dec. 31^d 22^h 30^m 27^s	Fukui Pref., Central Honshu.	20 ca km	1.65
48 July 29 16 1	One of the Aftershocks of the Fukui Earthquake	Shallow	1.68
58 June 24 4 51	Local Earthquake near Yakedake, Central Honshu.	Very shallow	1.58
55 Mar. 2 7 17 16	E part of Yamanashi Pref., Central Honshu.	20 ca	1.76

The values of V_p/V_s are normal in the cases of the first three earthquakes, but that of the fourth is considered to be anomalously large, being similar to the case of the Kyushu district. Namely, in the Yamanashi Prefecture, the value of V_p/V_s is larger than in the neighbouring region. It should be pursuited by a more detailed test using more abundant seismic data.

7. Some considerations on the low-velocity layer

Recently, Gutenberg stated that there are so-called low-velocity layers in the earth's crust and the upper mantle. In these layers, the P-velocity variation with depth is considerably different from the S-velocity variation and the rate of decrease in S-velocity is larger than in P-velocity (**7**).

In some regions, the depth of discontinuity estimated from the S-velocity is found to be greater than that estimated from the P-velocity. Katz represented the alternative explanation that the existence of layer with an increase of Poisson's ratio results in the different depths of discontinuity as mentioned above (**17**).

By the present investigation, it is ascertained that the layer with an anomalously large Poisson's ratio exists in the particular regions such as the Kyushu district. But the correlation between such anomaly of Poisson's ratio and the velocity variation with depth should be more investigated in future.

8. Summary

Poisson's ratio in the earth's crust is investigated, especially in relation to their local character. The P-S diagram method is effectively employed. Considering the correlation of the value of V_p/V_s with the focal depth of each earthquake, the mean straight lines in this diagram are drawn respectively and the anomalously large value of V_p/V_s which is calculated as from about 1.80 to 1.85 was found in the Kyushu district. The anomalous domain is considered to be situated at depths from about 20 km to 40 km in the earth's crust. The amplitude and period of seismic waves transmitted through this anomalous domain, the velocity variation with depth in this domain and others should be investigated in near future.

Moreover, the secular variation of seismic wave velocities are reported by some investigators. The value of V_p/V_s may probably vary with time. From those stand-points of view, further research of V_p/V_s is considered to be one of the effective and important methods to increase our knowledge on the nature of the earth's crust.

Acknowledgments

The writer wishes to express his hearty thanks to Prof. E. Nishimura for his kind guidance and encouragement throughout the present study and also to Prof. K. Sassa for his generous permission for analysis of seismograms obtained at the Abuyama and Aso observatories. The writer is also deeply indebted to the Directors and Members of the Japan Meteorological Agency for their generous permission for copying seismograms obtained at their observatories. The cost of the present study was partly defrayed by a grant-in-aid for scientific research of the Ministry of Education.

REFERENCES

1. J. B. MACELWANE, Evidence on the interior of the earth derived from seismic sources, *Internal Constitution of the Earth*, 2nd ed., Dover Publ., 1951, 227–304.
2. B. GUTENBERG, The elastic constants in the interior of the earth, *ibid.*, 364–381.
3. L. DON LEET and W. MAURICE EWING, Velocity of elastic waves in granite Physics **2** (1932), 160–173.
4. L. DON LEET, Velocity of elastic waves in granite and norite, Physics **4** (1933), 375–385.
5. B. GUTENBERG, Travel time curves at small distances, and wave velocities in southern Carifornia, Gerl. Beitr. z. Geophys., **35** (1932), 16–50.
6. K. E. BULLEN, Seismology and the earth's upper layers, *An Introduction to the Theory of Seismology*, 2nd ed., Cambridge Univ. Press, 1953, 187–205.
7. B. GUTENBERG, Wave velocities in the earth's crust, *Crust of the Earth*, Geol. Soc. America, Special Paper, **62** (1955), 19–34.
8. K. TAJIME and H. OKADA, Observation of the velocity of *S*-waves near the surface of the earth, Geophysical Exploration, **11** (1958), 65–7 (in Japanese).
9. K. IIDA, Measurements of elastic constants of rocks, Zisin, **13** (1941), 299–314 (in Japanese).
10. L. H. ADAMS, Elastic properties of materials of the earth's crust, *Internal Constitution of the Earth*, 2nd ed., Dover Publ., 1951, 50–80.
11. F. BIRCH, Physics of the crust, *Crust of the Earth*, Geol. Soc. America, Special Paper, **62** (1955), 101–117.
12. H. KAWASUMI, Study on the propagation of seismic waves (the first paper), Bull. Earthq. Res. Inst., **10** (1932), 94–129.
13. K. WADATI, On the velocity ratio of seismic waves of *P* and *S*, and its application to the determination of focal depth, J. Meteor. Soc. Japan, 2nd series, **10** (1932), 540–551 (in Japanese).
14. R. YOSHIYAMA, The ratio of the velocity of *P* and *S* waves, Bull. Farthq. Res. Inst., **35** (1957), 627–640.
15. R. YOSHIYAMA, The hypocentral region of the earthquake, Bull. Seism. Soc. America, **39** (1949), 187–188; **43** (1953), 153–158.
16. S. OMOTE, On the aftershocks of the Fukui Earthquake (Part 2), Bull. Farthq. Res. Inst., **28** (1950), 311–319.
17. S. KATZ, Seismic study of crustal structure in Pennsylvania and New York, Bull. Seism. Soc. America, **45** (1955), 303–326.

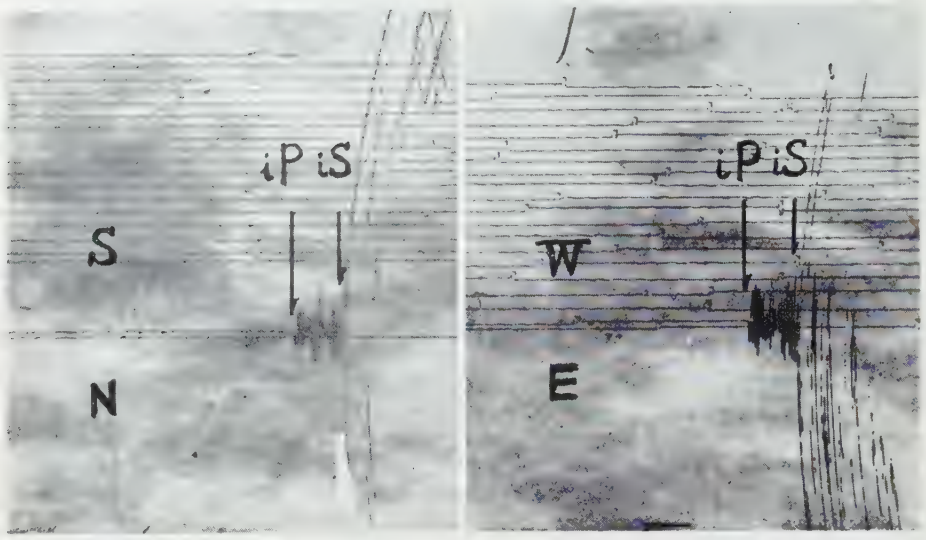

Fig. 3. The horizontal seismograms of earthquake No. 1 recorded at Matsuyama (△=81.5 km, in Shikoku). The constants of Wiechert seismograph are as follows (Magnification=70, Period=5.0 s Damping ratio=5).

(By the courtesy of the Matsuyama Meteorological Observatory)

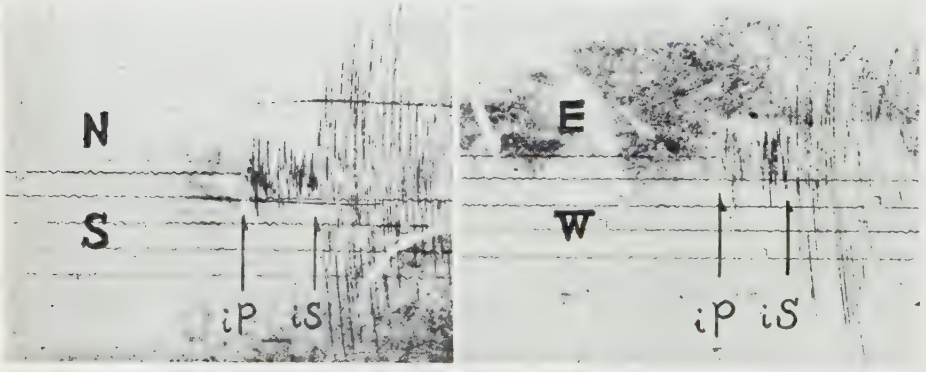

Fig. 4. The horizontal seismograms of earthquake No. 1 recorded at Kumamoto (△=148.3 km in Kyushu). The constants of Wiechert seismograph are as follows (Magnification=80, Period=4.8 s, Damping ratio=6).

(By the courtesy of the Kumamoto Meteorological Observatory)

Memoirs of the College of Science, University of Kyoto, Series A,
Vol. XXIX, No. 2, Article 5, 1959.

ADIABATIC COMPRESSIBILITY OF AQUEOUS SOLUTION OF INORGANIC ACID*

BY

Yoshio ISHIDA**

(*Received January 20, 1959*)

1. Introduction

The author recently investigated the ultrasonic sound velocity and the adiabatic compressibility of aqueous solution of H_2SO_4 (**1**, **2**). This time the ultrasonic velocities of the aqueous solutions of HCl and HNO_3 were measured and the adiabatic compessibilities were computed from them. We report here the procedure to derive an empirical formula for adiabatic compressibility of inorganic acid by the use of Gucker-Bachem's theory (**3**, **4**).

2. Outline of Gucker-Bachem's theory

We define *the apparent molal volume* by the following equation:

$$\phi(V_2) = \frac{V - V_1}{n_2}, \tag{1}$$

where V_1 [cm^3] is the volume of pure water and V the volume of the solution when n_2 mole of a solute is dissolved in V_1. If c is the molal concentration of the solution, we have

$$V = \frac{n_2}{c} \times 1000. \tag{2}$$

If d and d_1 are the density of the solution and that of the water respectively and M_2 is the molecular weight of the solute, we get, by the relation between masses,

$$V_1 d_1 = Vd - n_2 M_2. \tag{3}$$

Substituting V and V_1 as obtained from (2) and (3) in Eq. (1), we get

$$\phi(V_2) = \frac{1000}{c}\left(1 - \frac{d}{d_1}\right) + \frac{M_2}{d_1}. \tag{4}$$

The right-hand side of this equation consists of measurable quantities.

---

* Communicated by Professor I. Takahashi. Read before the symposium on acoustic chemistry at Nagoya University, Nov. 17, 1958.

** Department of Physics, Faculty of Education, Shimane University, Matsue.

Next, we define *the apparent molal compressibility* by

$$\phi(K_2) = \frac{\left(-\frac{\partial V}{\partial p}\right) - \left(-\frac{\partial V_1}{\partial p}\right)}{n_2}, \qquad (5)$$

where p denotes pressure. If β and β_1 are the adiabatic compressibilities of the solution and the water respectively, they are defined as:

$$\beta = -\frac{1}{V}\left(\frac{\partial V}{\partial p}\right), \quad \beta_1 = -\frac{1}{V_1}\left(\frac{\partial V_1}{\partial p}\right).$$

So, Eq. (5) can be converted into the form:

$$\phi(K_2) = \frac{\beta V - \beta_1 V_1}{n_2}.$$

By the use of Eqs. (2) and (3), we obtain

$$\phi(K_2) = \beta\frac{1000}{c} - \frac{\beta_1}{d_1}\left(\frac{1000\,d}{c} - M_2\right). \qquad (6)$$

The right-hand side of this equation consists also of measurable quantities.

By Gucker, Bachem and others, the following formulae were empirically established for aqueous solutions of strong electrolytes:

$$\phi(V_2) = \phi^0(V_2) + S_v c^{1/2}, \qquad (7)$$
$$\phi(K_2) = \phi^0(K_2) + S_k c^{1/2}. \qquad (8)$$

Here, $\phi^0(V_2)$, $\phi^0(K_2)$, S_v and S_k are constants.

From Eqs. (4), (6), (7) and (8), we can get the expression for the adiabatic compressibility as:

$$\beta = \beta_1 + Ac + Bc^{3/2}, \qquad (9)$$

with

$$\left.\begin{aligned} 10^3 A &= \phi^0(K_2) - \beta_1\phi^0(V_2), \\ 10^3 B &= S_k - \beta_1 S_v. \end{aligned}\right\} \qquad (10)$$

Our problem is to ascertain whether Eqs. (7) and (8) hold for aqueous solutions of inorganic acids and, if so, to obtain an experimental formula for β by calculating the constants A and B.

3. Treatment of experimental data

The ultrasonic velocities V and the densities d of $(HCl)_{aq}$, $(HNO_3)_{aq}$, and $(H_2SO_4)_{aq}$ at 30°C were measured at several concentrations, and the adiabatic compressibilities were calculated by $1/dV^2$. The results are tabulated in Appendix.

I. Case of HCl

The apparent molal volume $\phi(V_2)$ and the apparent molal compressibility $\phi(K_2)$

were calculated by Eqs. (4) and (6), and are plotted against $\sqrt{c}$ in Fig. 1 (a) and (b). Although the points in the figure are somewhat scattered, we can obtain respective straight lines by the method of least squares. Namely,

$$\phi(V_2) = 18.06+1.062\,c^{1/2}, \tag{11}$$

and

$$10^{12}\phi(K_2) = -1028+409.7\,c^{1/2}. \tag{12}$$

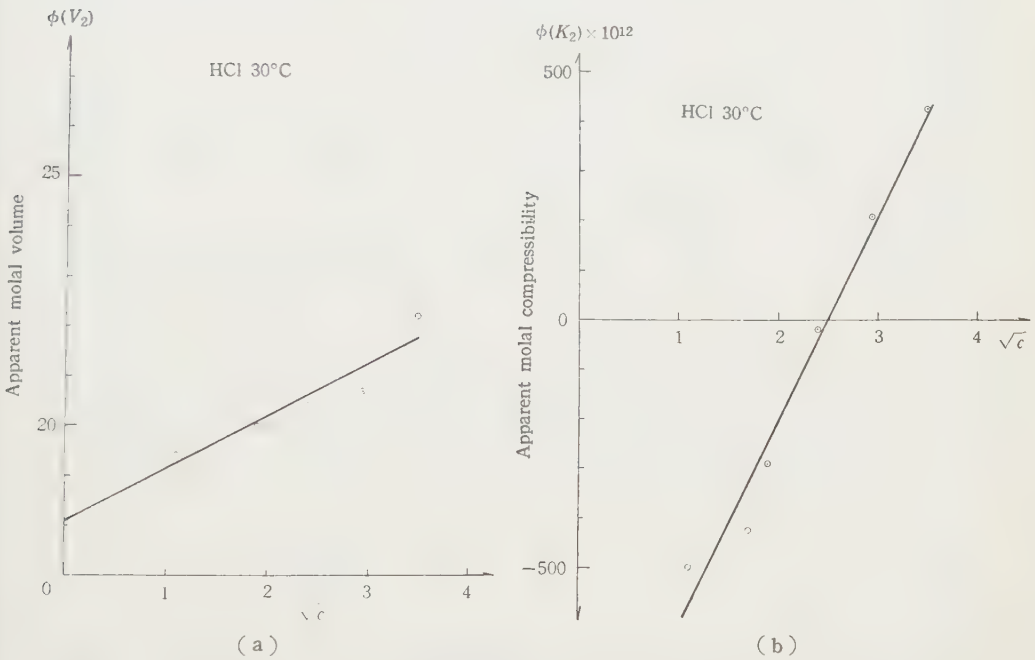

Fig. 1. Apparent molal volume and apparent molal compressibility *versus* square root of concentration in the case of $(HCl)_{aq}$.

Calculating the constants A and B by (10) using four coefficients in Eqs. (11) and (12), we obtain

$$10^{12}\beta = 44.11-1.825\,c+0.3629\,c^{3/2}. \tag{13}$$

In Fig. 2 the compressibility-curve is drawn by the use of this formula. The measured values of β (as calculated from $1/dV^2$) are also shown and it will be seen that they coincide well with the calculated curve, the mean deviation being 0.5%. The velocity-curve is also drawn in the same figure. It has a maximum at about 4 mole.

II. Case of HNO_3

The $\phi(V_2)-\sqrt{c}$ curve and the $\phi(K_2)-\sqrt{c}$ curve of $(HNO_3)_{aq}$ are shown in Fig. 3 (a) and (b). $\phi(V_2)$ is constant when $\sqrt{c}<2.2$ and varies linearly with $\sqrt{c}$ when $\sqrt{c}>2.2$. Namely,

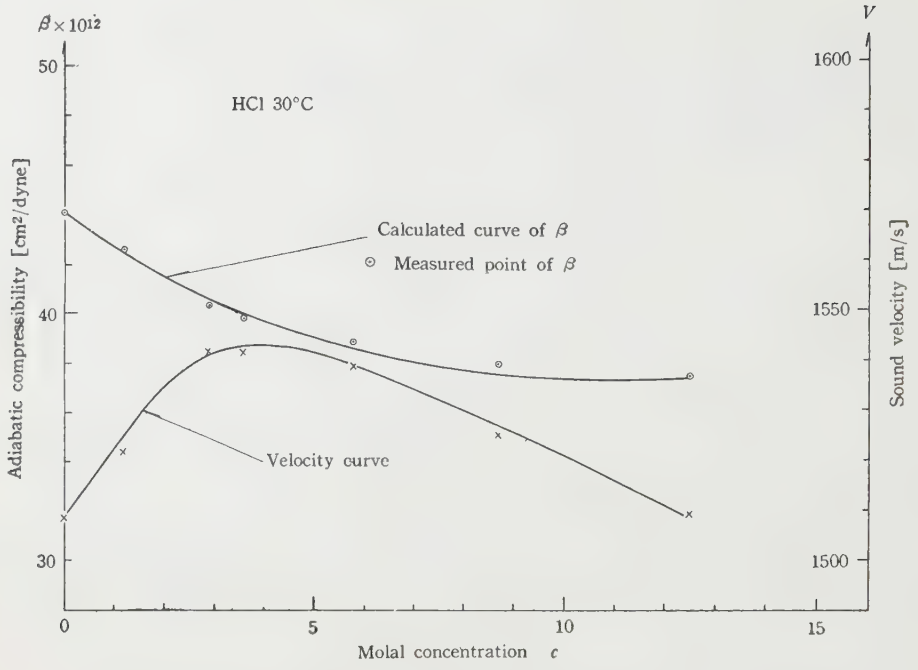

Fig. 2. Adiabatic compressibility and ultrasonic sound velocity *versus* concentration in the case of $(HCl)_{aq}$.

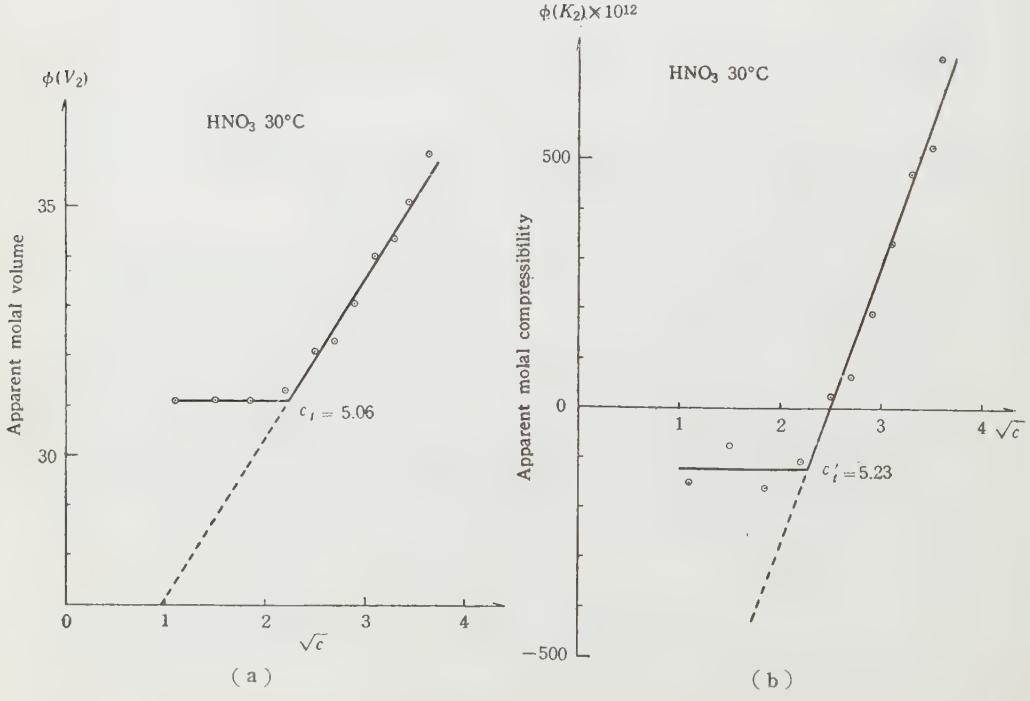

Fig. 3. Apparent molal volume and apparent molal compressibility *versus* square root of concentration in the case of $(HNO_3)_{aq}$.

$$\phi(V_2) = 33.10 \qquad \text{when } \sqrt[4]{c} < 2.2\,, \tag{14a}$$

and

$$\phi(V_2) = 23.87 + 3.223\, c^{1/2} \qquad \text{when } \sqrt[4]{c} > 2.2\,. \tag{14b}$$

The concentration c_t at the transition point has been calculated to be 5.06 mole by equating (14a) and (14b).

$\phi(K_2)$ is considered to be constant when $\sqrt[4]{c} < 2.3$ and varies linearly with $\sqrt[4]{c}$ when $\sqrt[4]{c} > 2.3$. That is,

$$10^{12}\phi(K_2) = -121.7\,, \tag{15a}$$

and

$$10^{12}\phi(K_2) = -1401 + 559.2\, c^{1/2}\,. \tag{15b}$$

And the concentration c_t' at the transition point has been obtained as 5.23 mole.

Calculating A, B by using coefficients in Eqs. (14b) and (15b), we get

$$10^{12}\beta = 44.11 - 2.454\, c + 0.4170\, c^{3/2}\,. \tag{16}$$

Since $\phi(V_2)$ and $\phi(K_2)$ are constant when $c < 5.06$, we get $S_k - S_v = 0$. Accordingly B becomes zero and we get a linear relation:

$$10^{12}\beta = 44.11 - 1.495\, c\,. \tag{17}$$

The concentration c_T at the transition point between (16) and (17) has been found to be 5.29 mole by equating both equations. In Fig. 4 the compressibility-curve is drawn

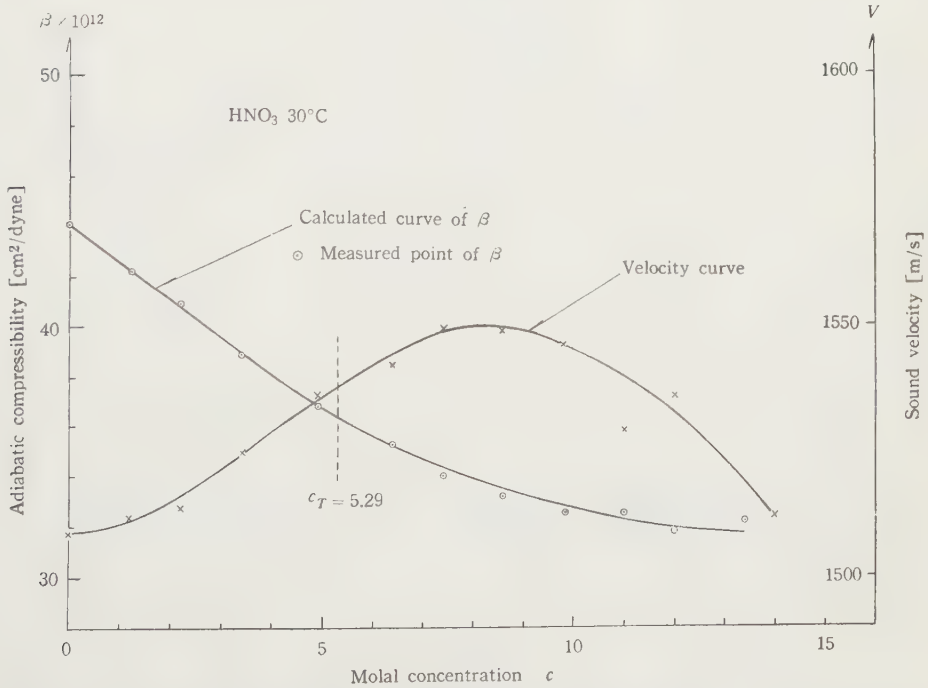

Fig. 4. Adiabatic compressibility and ultrasonic sound velocity *versus* concentration in the case of $(HNO_3)_{aq}$.

by the use of the formula (16) when $c>5.29$ and of the formula (17) when $c<5.29$. The measured values are also plotted and it is found that they coincide well with the calculated curve, the mean deviation being 0.4%. The velocity-curve is also drawn in the same figure. It has a maximum at about 8 mole.

III. Case of H_2SO_4

The $\phi(V_2)-\sqrt{c}$ curve and the $\phi(K_2)-\sqrt{c}$ curve of $(H_2SO_4)_{aq}$ are shown in Fig. 5 (a) and (b). $\phi(V_2)$ varies linearly with $\sqrt{c}$ up to $\sqrt{c}=3.8$, and deviates upward

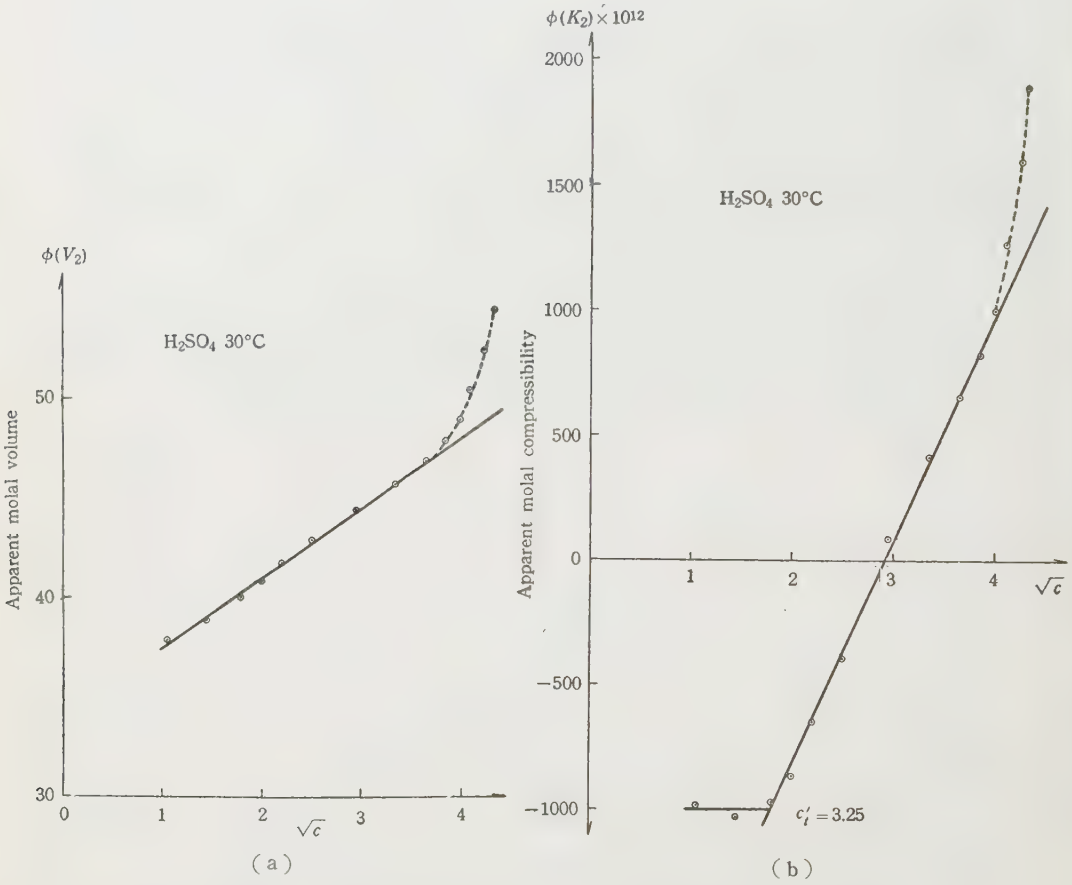

Fig. 5. Apparent molal volume and apparent molal compressibility *versus* square root of concentration in the case of $(H_2SO_4)_{aq}$.

rapidly from the straight line when $\sqrt{c}>3.8$. In the region of the straight line, we get

$$\phi(V_2) = 33.89+3.511\, c^{1/2}. \qquad (18)$$

$\phi(K_2)$ is constant when $\sqrt{c}<1.8$ and varies linearly with $\sqrt{c}$ in the region $1.8<\sqrt{c}<4$ and deviates upward from the straight line when $\sqrt{c}>4$. And we get

$$10^{12}\phi(K_2) = -994.3 \qquad \text{when } \sqrt{c} < 1.8, \qquad (19a)$$

$$10^{12}\phi(K_2) = -2609 + 895.6\, c^{1/2} \qquad \text{when } 1.8 < \sqrt{c} < 4. \qquad (19b)$$

The concentration c_t', at the transition point, is 3.25 mole. In the region $1.8 < \sqrt{c} < 3.8$, we get from (18) and (19b):

$$10^{12}\beta = 44.11 - 4.104\, c + 0.7407\, c^{3/2}. \qquad (20)$$

Since S_k becomes zero when $\sqrt{c} < 1.8$, we obtain:

$$10^{12}\beta = 44.11 - 2.489\, c - 0.1548\, c^{3/2}. \qquad (21)$$

It should be noted that the coefficient of $c^{3/2}$ is negative in (21). When $\sqrt{c} > 3.8$, β cannot be expressed by any formula of this form.

In Fig. 6 the compressibility-curve is drawn by the formula (21) when $c < 3.25$ and by the formula (20) when $c > 3.25$. The measured values are also plotted and it is found that they coincide well with the calculated curve when $c <$ about 14 mole, the mean deviation being 0.4%, but they disagree with it beyond the concentration of 14 mole. Since the transition seems to occur at the minimum point of $\beta - c$ curve, the concentration c_T at the transition point can be calculated to be 13.63 mole by solving the equation $d\beta/dc = 0$ obtained from (20). Beyond the concentration of 13.63

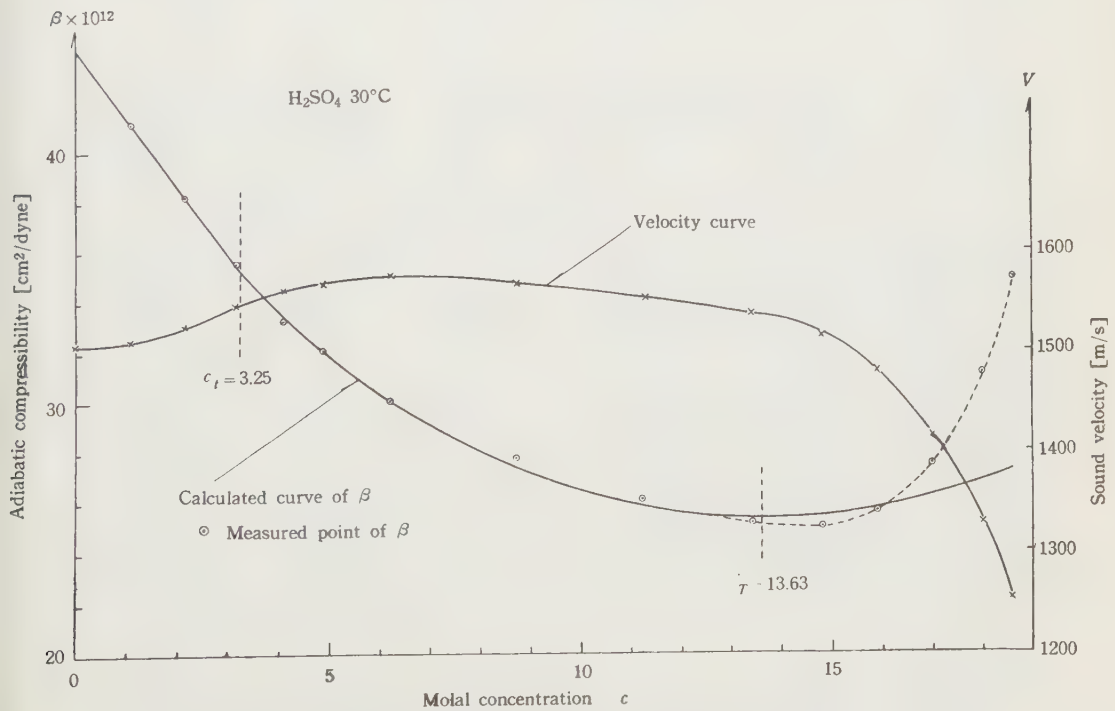

Fig. 6. Adiabatic compressibility and ultrasonic sound velocity *versus* concentration in the case of $(H_2SO_4)_{aq}$.

mole, the form of β has not yet been found. Consequently the form of β of $(H_2SO_4)_{aq}$ is divided into three parts. The velocity-curve is also drawn in the same figure and has a flat maximum which covers a wide range of concentration.

4. Summary and discussion

In Table I the coefficients of the experimental formulae which were obtained in the preceding section are summarized and compared with those given by Bhimasenachar and Subrahmanyam (**5**).

Table I. Coefficients of experimental formulae.

	Present author (30°C)			Bhimasenachar-Subrahmanyam (27°C)		
	Range of concentration [mol]	$A\times10^{12}$ [C.G.S.]	$B\times10^{12}$ [C.G.S.]	Range of concentration [mol]	$A\times10^{12}$ [C.G.S.]	$B\times10^{12}$ [C.G.S.]
HCl	$0<c<12.5$	−1.825	+0.3629	$0<c<4.5$	−1.692	+0.226
HNO_3	$0<c<5.29$	−1.495	0.0000	$0<c<6.0$	−1.8097	+0.1855
	$5.29<c<13.4$	−2.454	+0.4170			
H_2SO_4	$0<c<3.25$	−2.489	−0.1548	$0<c<3.4$	−3.402	+0.123
	$3.24<c<13.6$	−4.104	+0.7407	$3.4<c<9.0$	−4.695	+0.957
	$13.6<c$	undetermined				

Both groups of values almost coincide with each other to the first order. We want to point out that the measurement of Bhimasenachar and Subrahmanyam was done in a comparatively narrow range of concentration. They determined also the coefficients A and B by direct application of the method of least squares to the compressibility-curve, on the assumption that the formula (9) would fit the curve. For the purpose of finding the coefficients A and B, their method is appropriate, but our method is more fundamental and orthodox. Moreover, the following instance may confirm the superiority of our method. As the value of B of H_2SO_4 at lower concentration, the author obtained the value of -0.1548, while they gave a quite different value of $+0.123$. When we calculate the value of B by direct application of the method of least squares to $\beta-c$ curve, it occurs that B becomes negative when calculated from the first three data ($0<c<3.2$) and positive when calculated from the first four data ($0<c<4.7$). And there is no definite criterion to determine whether we should take the first three or the first four. But in the author's method, there is a definite reason why B should be negative, namely, that the $\phi(K_2)$ is constant when $c<3.25$.

Acknowledgment

The author wishes to thank Professor I. Takahashi for his continual encouragement and valuable discussions.

APPENDIX

I. HCl (30°C)

Conc. [mol]	Density [g/cm³]	Velocity [m/s]	Measured* $\beta_m \times 10^{12}$	Calculated** $\beta_c \times 10^{12}$	Deviation $\beta_m - \beta_c$
1.190	1.0161	1522	42.49	42.41	+0.08
2.905	1.0435	1542	40.30	40.60	−0.30
3.602	1.0552	1542	39.85	40.02	−0.17
5.798	1.0892	1539	38.75	38.59	+0.16
8.680	1.1331	1525	37.93	37.55	+0.38
12.48	1.1746	1509	37.38	37.33	+0.05

* β_m computed by the formula $1/dV^2$.
** β_c calculated by the experimental formula (13).

II. HNO_3 (30°C)

Conc. [mol]	Density [g/cm³]	Velocity [m/s]	Measured $\beta_m \times 10^{12}$	Calculated* $\beta_c \times 10^{12}$	Deviation $\beta_m - \beta_c$
1.245	1.0357	1512	42.23	42.25	−0.02
2.185	1.0658	1514	40.95	40.84	+0.11
3.416	1.1053	1525	38.89	39.00	−0.11
4.917	1.1522	1536	36.79	36.76	+0.03
6.362	1.1932	1542	35.24	35.19	+0.05
7.400	1.2243	1549	34.04	34.34	−0.30
8.614	1.2551	1549	33.21	33.51	−0.30
9.847	1.2831	1546	32.60	32.84	−0.24
11.06	1.3147	1529	32.54	32.30	+0.24
11.97	1.3322	1536	31.81	32.01	−0.20
13.39	1.3589	1512	32.19	31.68	+0.51

* β_c calculated by the experimental formulae (16) and (17).

III. H_2SO_4 (30°C)

Conc. [mol]	Density [g/cm³]	Velocity [m/s]	Measured $\beta_m \times 10^{12}$	Calculated* $\beta_c \times 10^{12}$	Deviation $\beta_m - \beta_c$
1.104	1.0623	1512	41.18	41.18	0.00
2.138	1.1228	1526	38.24	38.30	−0.06
3.163	1.1799	1546	35.46	35.37	+0.09
4.068	1.2296	1563	33.28	33.49	−0.21
4.860	1.2711	1567	32.04	32.10	−0.06
6.185	1.3395	1577	30.02	30.12	−0.10
8.710	1.4658	1567	27.78	27.40	+0.38
11.24	1.5871	1553	26.12	25.89	+0.23
13.37	1.6844	1536	25.17	25.46	−0.29
14.79	1.7429	1515	25.00	25.54	−0.54
15.93	1.7826	1480	25.61	25.82	−0.21
17.04	1.8113	1416	27.53	26.28	+1.25
18.04	1.8256	1327	31.10	26.82	+4.28
18.63	1.8231	1253	34.94	27.21	+7.73

* β_c calculated by the experimental formulae (20) and (21).

REFERENCES

1. Y. Ishida : J. Phys. Soc. Japan, **13** (1958), 536.
2. Y. Ishida : Mem. Coll. Sci. Univ. Kyoto, A **26** (1958), 91.
3. F. T. Gucker : J. American Chem. Soc., **55** (1933), 2709.
4. C. H. Bachem : ZS. f. Phys., **101** (1936), 541.
5. J. Bhimasenachar and S. V. Subrahmanyam : J. Acous. Soc. America, **29** (1957), 899.

Memoirs of the College of Science, University of Kyoto, Series A,
Vol. XXIX, No. 2, Article 6, 1959.

A NEW COMPOUND IN Au-Pb ALLOY SYSTEM*

BY

Yoshibumi FUJIKI**

(*Received March 1, 1959*)

ABSTRACT

A new phase as observed by the electron diffraction method in the thin films of Au-Pb alloy was confirmed by both the metallographic and X-ray diffraction methods with bulk specimens. This new phase was an intermetallic compound whose composition was $AuPb_3$, and was formed peritectically like the compounds Au_2Pb and $AuPb_2$. The unit cell of $AuPb_3$ is tetragonal with lattice constants $a=11.958$ Å and $c=5.878$ Å. The measured density is 12.8 g cm^{-3} which agrees well with the calculated one on the basis of 8 molecules per unit cell (12.93 g cm^{-3}). The peritectic point of this phase is very close to the eutectic temperature (215°C).

1. Introduction

In Au Pb alloy system, two intermetallic compounds, Au_2Pb and $AuPb_2$, have already been known. The former is cubic with lattice constant $a=7.93$ Å, while the latter is tetragonal with $a=7.31$ Å, $c=5.644$ Å, and both crystallize by the peritectic reaction.

By the electron diffraction study on Au-Pb alloy films prepared by the deposition of metal vapours in vacuum, the writer found a new phase (Fig. 1) in Pb-rich side of this alloy system, and its composition was estimated between the eutectic (15 wt. % Au) and $AuPb_2$ (32.2 wt. % Au). This new phase seemed to be stable but not metastable one. In order to confirm this and to determine the accurate composition and the lattice dimensions, the writer carried out the X-ray diffraction and metallographic investigations with bulk specimens.

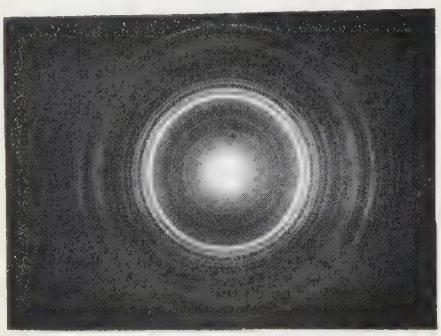

Fig. 1. The electron diffraction pattern of the new phase.

* Communicated by Professor K. Tanaka.

** Institute of Physics, Kyoto Prefectural Medical College.

2. Experimental procedure

Specimens used are 99.99% Au and Merck's Pb. Specimens were vacuum sealed in Terex glass tubes (6~8 mm in diameter and about 1 mm in wall thickness). The amount of specimen in each tube was about 10 g. These specimens were melted in a salt bath at about 400°C for 15~30 minutes, quenched in a mixture of ice and NaCl or air-cooled to room temperatures, and then annealed for a suitable time at about 200°C. After these heat treatments, specimens were polished by emery papers, tooth-paste and silk velvet, etched in the solution of 5% nitric acid in absolute alcohol and then investigated microscopically.

A part of each especimen used in the microscopical study was examined by the X-ray diffraction with powder method using a Cu K_α radiation with Ni filter.

3. Experimental results

(a) *Determination of composition*

Fig. 2 shows a photomicrograph of the typical eutectic structure obtained by the air-cooled specimen of an alloy containing 15 wt. % Au. This specimen does not show any appreciable change of texture after annealing for about 24 hours at about 200°C. An X-ray powder pattern obtained by this specimen showed the presence of Pb and the new phase, thus indicating that the latter is surely present in bulk specimens and its composition is between $AuPb_2$ and the eutectic. Then, starting from the eutectic composition, specimens differing by one or two wt. % Au were prepared and examined microscopically as well as by X-ray diffraction method after heat treatment.

Specimens in the range of compositions of 17~23 wt. % Au indicate two phases of the eutectic and the new phase, one of the photomicrographs being shown in Fig. 3. From the facts that the X-ray patterns of these specimens show very intense diffraction rings of the new phase, it is known that the large grains appeared in Fig. 3 are the crystals of the new phase.

The specimens containing 24 wt. % Au show one phase after suitable annealing, as is shown in Fig. 4. X-ray pattern of this annealed specimen also shows that of the new phase only (Fig. 9).

The alloy containing 25 wt. % Au shows two phases after annealing (see Fig. 5). It is confirmed by X-ray diffraction that these two phases are the new phase and $AuPb_2$.

From the results mentioned above, it seems that this new phase has no appreciable homogeneous range but is a compound like Au_2Pb or $AuPb_2$, and this result should be compared with a calculated value of 24.08 wt. % Au for the formula unit $AuPb_3$.

(b) *Crystal system and unit cell dimensions*

The X ray diffraction pattern of this new compound (Fig. 9) can be indexed on

Table I.

(*hkl*)	*d* (calc.)	*d* (obs.)	*I* (obs.)
(110)	8.456Å	(8.46Å)*	w
(200)	5.979	(5.92)*	vw
(101)	5.275	(5.29)*	w
(220)	4.224	(4.22)*	vw
(211)	3.956	(3.96)*	w
(310)	3.781	(3.78)*	vw
301	3.299	(3.30)*	vw
(002)	2.939	(2.98)*	vvw
(321)	2.888	2.890	s
(330)	2.818	2.822	vs
(112)	2.776	2.781	m
(420)	2.674	2.672	w
(411)	2.600	2.597	vs
(222)	2.413	2.418	s
(510)	2.345	2.338	m
(312)	2.321	2.314	m
(520)	2.221	2.227	vw
(402)	2.096	2.098	vvw
(521)	2.077	2.075	vw
(611)	1.864	1.863	m
(710)	1.691	1.691	s
(602)	1.650	1.651	w
(711)	1.625	1.628	s
(721)	1.582	1.584	w
(542)	1.576	1.574	vw
(650)	1.531	1.533	vw
(731)	1.517	1.519	vw
(004, 523)	1.469	1.470	s
(741, 811)	1.438	1.438	m
(660)	1.409	1.408	vvw
(821)	1.408		
(613, 224)	1.388	1.388	w
(831)	1.362	1.361	w
(840)	1.337	1.335	vw
(910)	1.321	1.320	vvw
(414)	1.311	1.307	w
(901)	1.296	1.293	m
(921, 761)	1.267	1.265	vw
(504, 434)	1.252	1.249	vvw
(851)	1.239	1.240	vw
(444, 653)	1.206	1.205	w
(771)	1.184	1.183	w
(852, 115)	1.164	1.164	vvw
(951)	1.140	1.139	vw
(704)	1.112	1.114	w
(724, 913)	1.095	1.095	w
(844, 10.33)	0.988	0.988_8	vvw
(981, 12.11)	0.977	0.979_2	vvw
(854)	0.959	0.959_8	vvw
(226, 12.31)	0.953	0.954_0	vvw
(406)	0.931	0.930_9	vvw
(805)	0.923	0.924_0	vvw

* These lines were observed by the electron diffraction method.

the basis of a tetragonal unit cell with $a=11.958$ Å and $c=5.878$ Å. The observed and calculated spacings are shown in Table I. (The X-ray diffraction rings corresponding to large spacings were difficult to measure, and therefore the values of these spacings were taken from the electron diffraction data.)

The density of $AuPb_3$ measured by Yoshida and Takei's method (**1**) was found to be 12.8 g cm^{-3} which agrees well with the value 12.93 g cm^{-3} calculated on the basis that the unit cell contains 8 molecules.

(c) *Transformation by the peritectic reaction*

Fig. 6 shows a microphotograph of quenched specimen containing 24 wt. % Au. This shows only two phases. X-ray pattern of this specimen shows the diffraction rings of $AuPb_2$, $AuPb_3$ and Pb, and the relative intensity of $AuPb_3$ and Pb is similar to that of eutectic. This shows that these two phases are $AuPb_2$ and eutectic, but not $AuPb_3$ phase. Similar results were obtained for air-cooled specimens of other compositions between 26 wt. % Au and 17 wt. % Au.

The quenched specimen of 24 wt. % Au transforms easily into one phase after the annealing for about 26.5 hours at about 200°C (Fig. 4), but the air-cooled one of the same composition (Fig. 7) does not completely transform into one phase even after the prolonged annealing for about 60 hours. (see Fig. 8). These facts and the results mentioned in section (a) show that the $AuPb_3$ phase is formed by the peritectic reaction.

The incompletion of transformation in air-cooled specimens may depend upon the fact that the grain size of $AuPb_2$ is relatively large compared with the grain size of

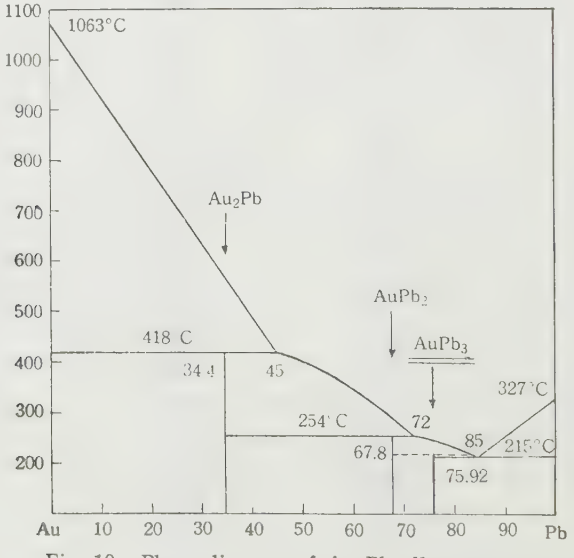

Fig. 10. Phase diagram of Au-Pb alloy system. The position of $AuPb_3$ is shown.

$AuPb_2$ in quenched specimens, and the rate of peritectic reaction is almost interrupted after these grains were surrounded by the new phase.

The fact that the $AuPb_2$ phase presents itself even in the quenched or air-cooled specimens of 17 wt. % Au and the $AuPb_3$ phase is absent suggests that the peritectic point of $AuPb_3$ is very close to the eutectic temperature. In fact, the electron diffraction observations on the highest temperature of stability for the $AuPb_3$ phase support this suggestion (Fig. 10), but the precise determination of the peritectic point requires further investigations.

4. Summary

In Au-Pb alloy system, a new compound was found, the composition of which was metallographically determined to be $AuPb_3$. It was determined by X-ray diffraction method that the unit cell of this compound is tetragonal with lattice constants $a=11.958$ Å and $c=5.878$ Å containing 8 molecules. The measured density was 12.8 g cm^{-3}, while the calculated one was 12.93 g cm^{-3}. It was also confirmed by the metallographic study that the new compound $AuPb_3$ is formed peritectically like Au_2Pb or $AuPb_2$ and the peritectic point of this compound is very close to the eutectic temperature (215°C).

Acknowledgements

The writer wishes to express his gratitude to Prof. K. Tanaka for encouragement and advice in the course of this investigation. He also wishes to thank Prof. K. Iwase and Dr. M. Kyōtani for their kind advice and discussions. The writer's thanks are also due to Messrs. R. Suganuma and T. Yoshida for their assistance in this work.

REFERENCE

1. U. Yoshida and B. Takei: Mem. Coll. Sci. Univ. of Kyoto, **A15** (1932), 1.

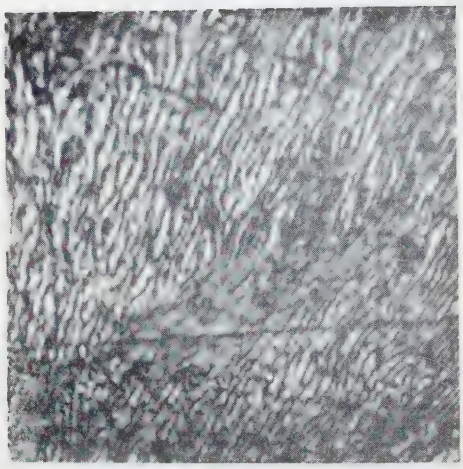

Fig. 2. ×800

15 wt. % Au, air-cooled
(eutectic)

Fig. 3. ×150

23 wt. % Au, annealed for 28 hours at 200°C
($AuPb_3$+eutectic)

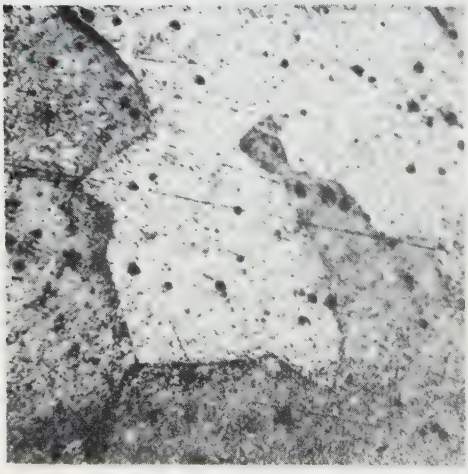

Fig. 4. ×150

24 wt. % Au, quenched and annealed for 26.5 hours at 200°C
($AuPb_3$)

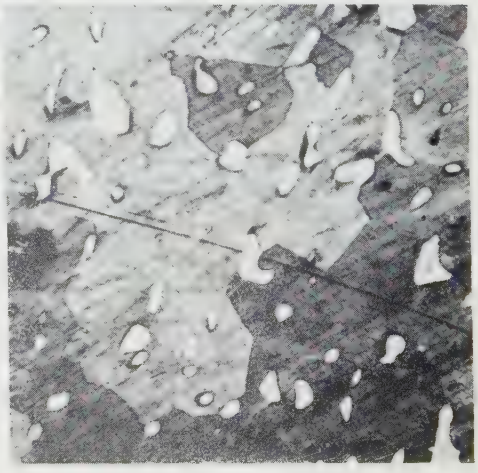

Fig. 5. ×150

25 wt. % Au, annealed for 53 hours at 200°C
($AuPb_3$+$AuPb_2$)

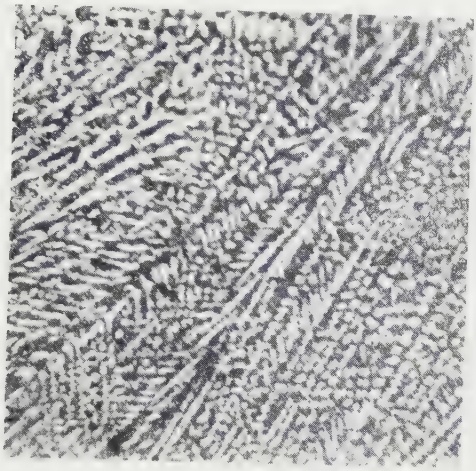

Fig. 6. 150

24 wt. % Au, quenched
($AuPb_2$+eutectic)

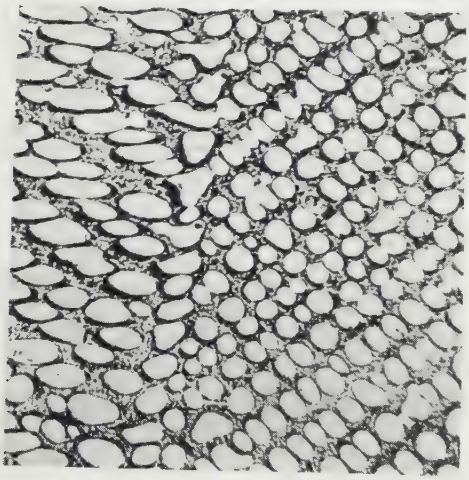

Fig. 7. ×150

24 wt. % Au, air-cooled
($AuPb_2$+eutectic)

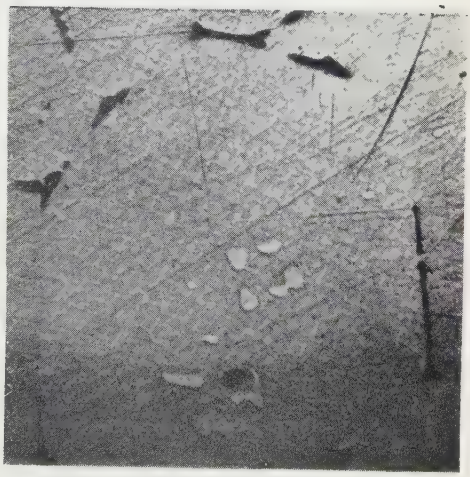

Fig. 8. ×150

24 wt. % Au, air-cooled and annealed for 60 hours at 200°C
($AuPb_3$+$AuPb_2$+eutectic)

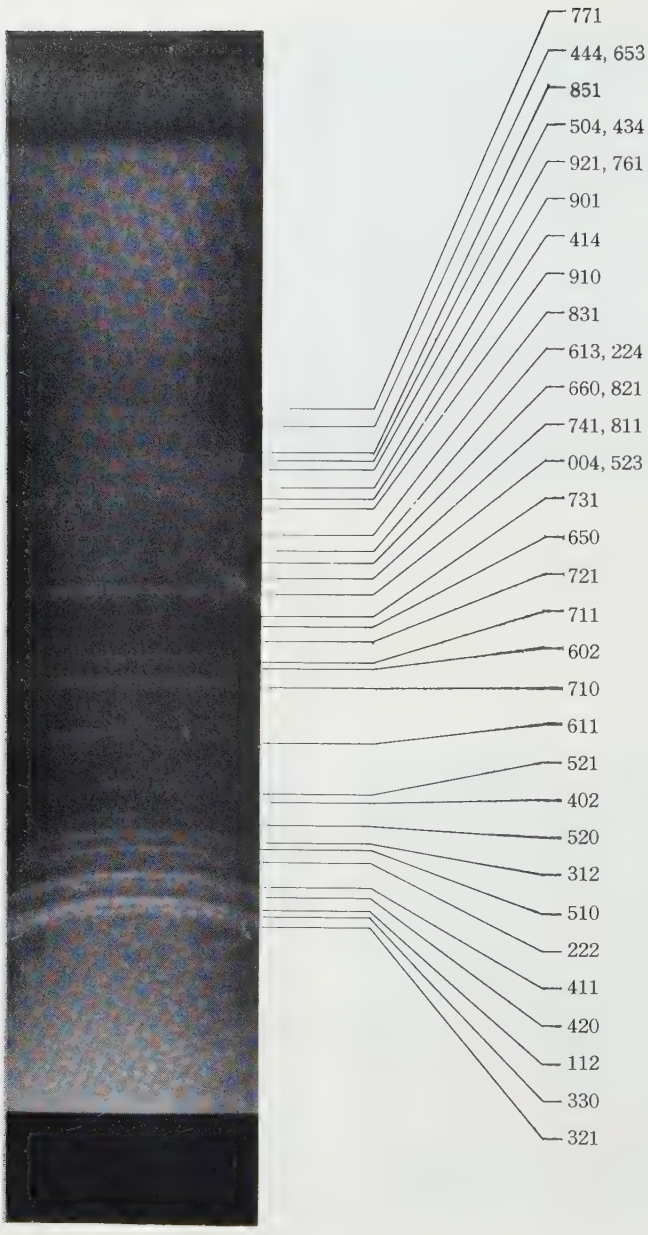

Fig. 9.

24 wt. % Au–Pb ($AuPb_3$)
Tetragonal $a_0 = 11.95_8$Å
$c_0 = 5.87_8$A

Memoirs of the College of Science, University of Kyoto, Series A,
Vol. XXIX, No. 2, Article 7, 1959.

NUCLEAR MAGNETIC RESONANCE PULSE APPARATUS

BY

Tsuneo HASHI, Akira HIRAI, Masahumi SASAKI and **Takao KAWAI**

(*Received June 1, 1959*)

ABSTRACT

A detailed description of the nuclear magnetic resonance pulse apparatus in our laboratory is given. This apparatus is intended for measuring the spin-lattice relaxation time of proton in high polymer between 10 msec and 1,000 msec.

1. Introduction

The nuclear magnetic resonance method has been used to give valuable informations about microscopic states and dynamical characters of many substances (**1**). Recently, the importance of informations about the spin-lattice relaxation time (T_1) has increased, particularly for high polymers, since the data obtained from nuclear magnetic resonance line width or line shape alone are not sufficient for full understanding of the internal motion in high polymer.

The saturation method (**2**), which has been most frequently used for the measurement of T_1 of high polymer, requires knowledge about the spin-spin relaxation time (T_2) and the magnetic rf field intensity (H_1). This method is rather complicated and there are further inconveniences caused by some anomalous phenomena associated with increasing magnetic rf field intensity (**3**, **4**), particularly in solid. The pulse method (**5**) is relatively simple and direct. Thus, we have constructed a pulse apparatus for the purpose of measuring T_1 of proton in high polymer. This apparatus has been successfully operated except for samples in the rigid state which have broad lines and require, for measurement, extremely intense and narrow rf pulse and short receiver recovery time not realized in the present apparatus. This situation, however, is not serious for our present purpose, since the most interesting phenomena to be investigated for high polymers are about the internal motion and therefore the samples concerned are not in the rigid state.

Recently, a few articles have already appeared about the nuclear magnetic resonance pulse apparatus (**6**, **7**). Still we feel it worth-while to report and discuss about our apparatus, because it is more convenient for measuring T_1 from 10 to 1,000 msec than other apparatus already reported, and in addition, it is difficult, in our

country, to use even some of the commercial devices described in the above articles, such as Tektronix Pulse Generator.

2. Construction of apparatus

The diagram of the whole apparatus is given in Fig. 1. We have adopted 90°–90° pulse method for its simplicity of both construction and adjustment. The pulse train method is also applicable but was not adopted because of its critical dependence upon the 90° pulse setting. The T_1 of proton in high polymer is relatively long, so we have measured the pulse interval with a frequency counter consisting of a standard

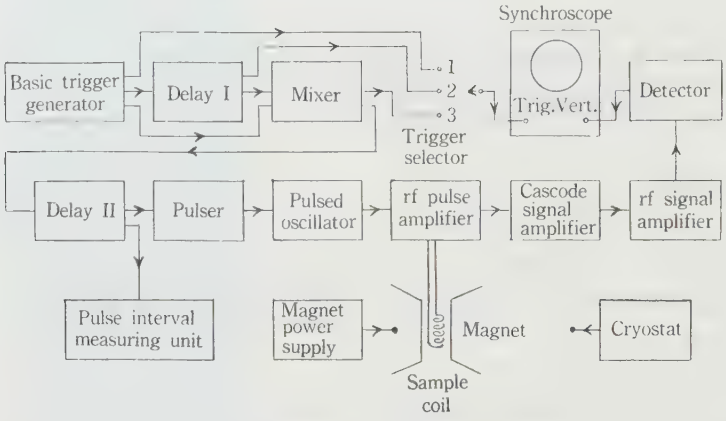

Fig. 1. Block diagram of the whole apparatus.

audio frequency oscillator, a bistable multivibrator, a gate and decatrons. Other units of the present apparatus are all of standard type as used in the ordinary pulse apparatus. Our measurements have been done at 25 Mc/sec and about 6,000 gauss. Each unit is described in delail in the following.

(1) *Basic trigger generator*

This unit determines repetition interval (the interval between basic triggers). The repetition interval should be very long compared with T_1, while the shorter the repetition interval, the easier the measurement. In our measurement the repetition interval has been chosen between 0.5 and 5 sec. That the repetition interval is long enough has been ascertained by checking that the signal amplitude just after the first pulse (y_1) does not become larger for longer repetition interval. To obtain basic triggers, a frequency dividing unit and a decatron system were employed. The block diagram is shown in Fig. 2. Last three sections are inserted for eliminating undesired components of the output from the decatron, whose wave form consists of a desired large pulse, a long tail following and nine small pulses. The circuit diagram of the frequency dividing unit consisting of a cathode coupled monostable multivibrator (8) is shown in Fig. 3.

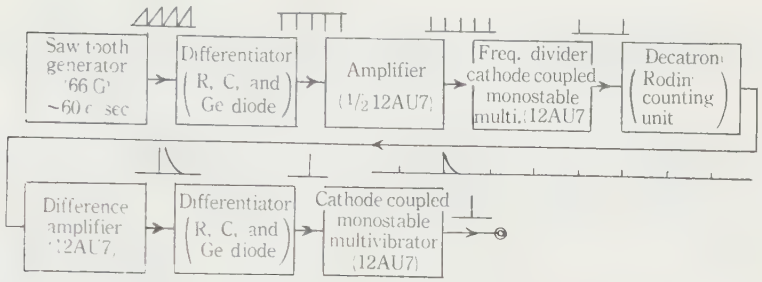

Fig. 2. Block diagram of basic trigger generator.

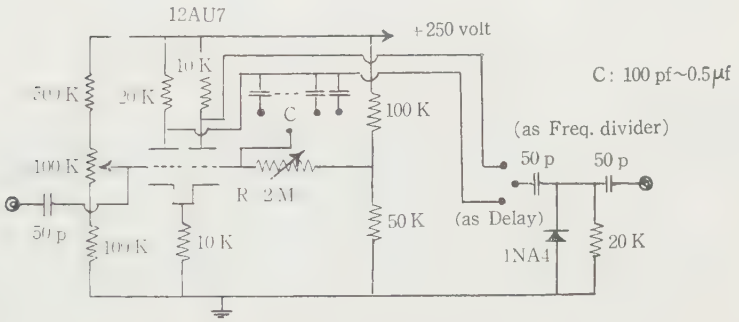

Fig. 3. Circuit diagram of cathode coupled monostable multivibrator as delay unit or as frequency dividing unit.

(2) *Delay I*

This is also a cathode coupled monostable multivibrator as in Fig. 3. This unit determines the pulse interval τ, which is the interval between the first and the second triggers and is measured by the pulse interval measuring unit.

(3) *Mixer*

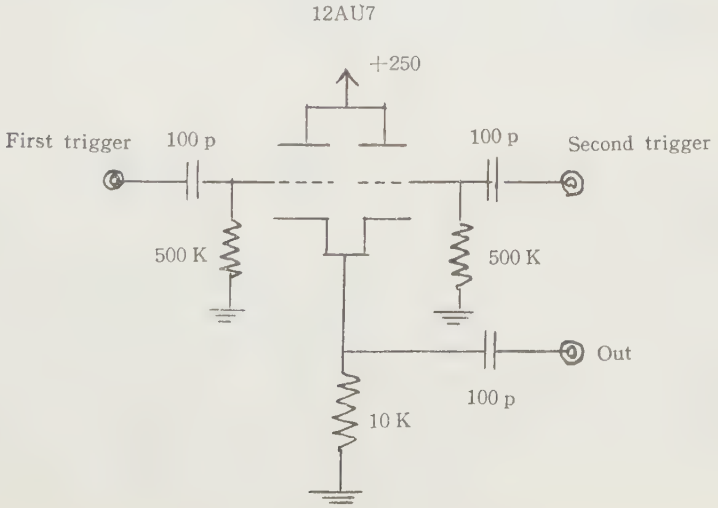

Fig. 4. Circuit diagram of mixer.

In this unit, the first and the second triggers are mixed. They are desired to have the same waveform. For this reason, the last section in the basic trigger generator (Fig. 2) is inserted. The circuit diagram is shown in Fig. 4.

(4) *Delay II*

This unit serves the signal being located at a desired position on the synchroscope screen. The circuit diagram is the same as in Fig. 3.

(5) *Pulser*

This unit is triggered by the output of Delay II and creates a rectangular waveform whose width (t_w) is controllable so as to be $\gamma H_1 t_w = \pi/2$ for 90° pulse. In our case, t_w was about 5μsec for 90° pulse. We have used a cathode coupled monostable multivibrator, though a more excellent circuit, such as plate coupled multivibrator with plate catching diode (**9**), would be desirable.

(**6**) *Pulsed oscillator*

A continuous rf oscillation and pulse modulation system (**7**) would be desirable for the frequency stability and the rf pulse wave shape. But it is very difficult to avoid the rf power leakage during off-time and this leakage makes beat with the nuclear signal, so we have adopted a pulsed oscillation system. This unit is essentially the same as that of E. L. Hahn (**5**). Care must be taken so that both the rf field intensity and the pulse width should not be modulated by heater hum voltage.

(7) *Pulsed rf amplifier*

This unit is inserted for obtaining a large rf magnetic field H_1, which should be several times larger than the resonance line width $\Delta H_{1/2}$. In our apparatus, H_1 was about 15 gauss, which was limited not by the available power from power tube 813 but by rf pulse wave shape. We have lowered the "Q" of the sample coil to preserve good wave shape at the expense of rf field intensity. It is also desirable to set the rf amplifier, the sample coil, and the cascode signal amplifier in one chasis for avoiding the capacitive coaxial cable connections. The circuit diagram of this unit together with the sample coil is shown in Fig. 5.

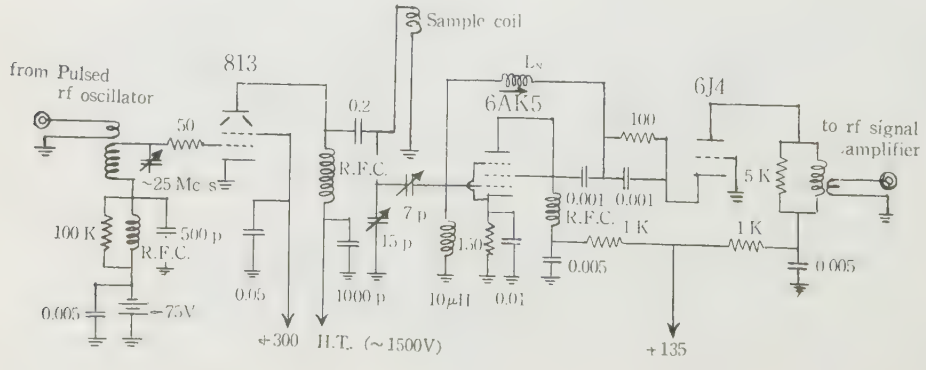

Fig. 5. Circuit diagram of rf pulse amplifier, sample coil, and cascode signal amplifier.

(8) *Cascode signal amplifier*

This unit serves for improving the overall S–N ratio, and is of original Wallman type (**10**). The circuit diagram is shown in Fig. 5.

(9) *rf signal amplifier and detector*

This unit is essentially of the standard type (**11**) with some modifications in the input stage. The circuit diagram of this unit is shown in Fig. 6. We have adopted the straight amplification system (gain 90 db, band-width 4 Mc/sec, receiver recovery time about 10μsec). But a superheterodyne system would be convenient in the

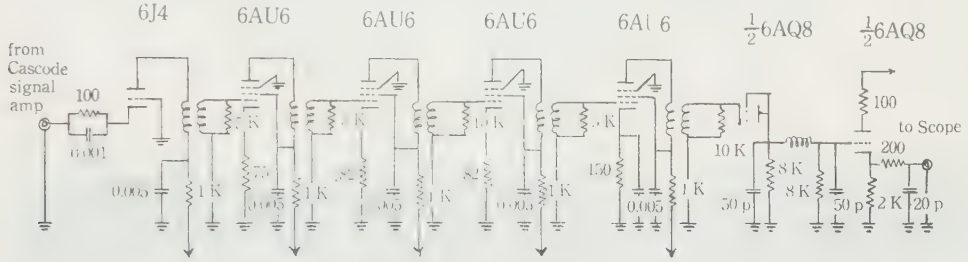

Fig. 6. Circuit diagram of rf signal amplifier.

variable rf frequency measurement. If the synchroscope has a good frequency characteristics up to about 30 Mc/sec, it is desirable to omit the detector to shorten the recovery time.

(10) *Synchroscope*

This is a commercial product. In our measurement, the signal appears on screen only once per several seconds, so a long persistent cathode ray tube or a memoriscope (recently commercialized) would be conveniently used.

(**11**) *Pulse interval measuring unit*

The block diagram of this unit is shown in Fig. 7. The audiofrequency oscillator is a commercial variable audio frequency oscillator, which is sufficient for our present purpose. For more accurate measurement, the crystal oscillator and frequency dividing system should be used. The circuit diagram of the bistable multivibrator (**12**) and

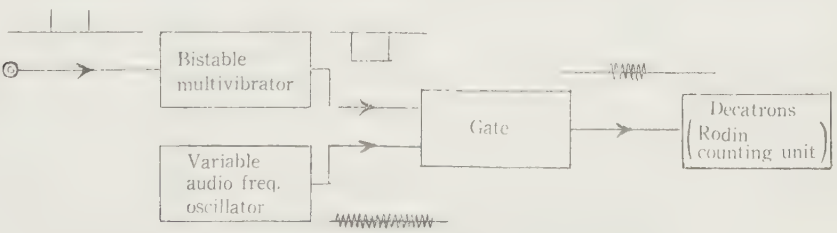

Fig. 7. Block diagram of pulse interval measuring unit.

the gate (**13**) is shown in Fig. 8. It may happen, however, that the decatrons begin counting the interval between the second and the next first triggers instead of the desired pulse interval. The switch in the diagram serves to change the measuring

from the undesired interval to the desired one.

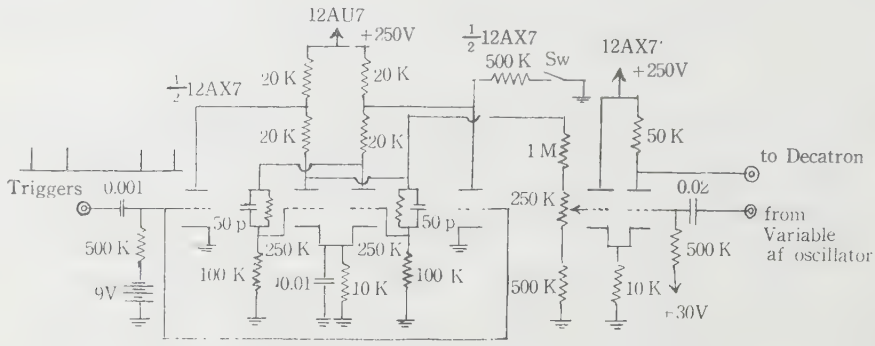

Fig. 8. Circuit diagram of bistable multivibrator and gate.

(12) *Magnet*

The diameter of pole piece is 12 cm. The pole gap is 3.6 cm. The current required for 6,000 gauss is about 500 mA. The field homogeneity is such that the free induction decay signal lasts about 500μsec for narrow lines, which was convenient for adjustment and measurement.

(13) *Magnet power supply*

This is essentially the same as that of H. L. Anderson (**14**). One measurement requires about 15 minutes, at least during which the dc magnetic field intensity (H_0) must be stable.

(14) *Cryostat*

A gas flow cryostat (**15**) has been used. The constancy of our apparatus was not so good, and about ± 1°C. We are now planning some improvements.

3. Procedures

(1) The dc magnetic field intensity H_0 is adjusted for exact resonance, searching for the maximum of the signal after the first pulse for a small pulse width t_w.

(2) Then, the pulse width is gradually expanded so as to satisfy 90° pulse condition, utilizing that the signal after the second pulse should be zero for a small pulse interval (Delay I) and 90°–90° pulse condition (see Fig. 9 (a)). In Fig. 9 (a), the synchroscope trigger selector is set at 1 (in Fig. 1) and the synchroscope sweep speed is relatively low. With the trigger selector set at 3 (in Fig. 1) and the sweep speed increased, and otherwise on the same condition, the screen pattern is like Fig. 9 (b).

(3) Then the pulse interval is gradually expanded by changing R and C in Delay I, and calibrated by the pulse interval measuring unit (see Fig. 10). The difference between the signal after the first pulse y_1 and that after the second pulse (y_2) is plotted against the pulse interval τ on semi-logarithmic section paper. The slope of the plotted line, when straight, gives T_1 (see Fig. 11).

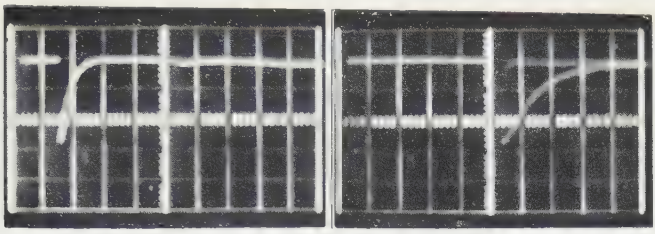

(a) (b)

Fig. 9. Synchroscope screen pattern for 90° – 90 pulse setting, second nuclear signal disappearing,
Sample : PMA, Temperature : 34°C, Repetition interval : 2.2 sec,
Resonance frequency : ν_0=25 Mc/sec,
Pulse width : t_w=7μsec,
a) Synchroscope trigger selector set at 1,
Sweep rate : 200μsec/cm,
b) Synchroscope trigger selector set at 3,
Sweep rate : 50μsec/cm.

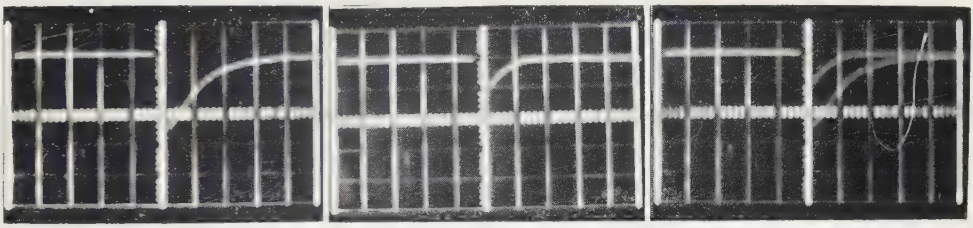

(a) First pulse and nuclear signal

(b) Second pulse and nuclear signal

(c) First and second pulses and nuclear signals

Fig. 10. Synchroscope screen patterns for measuring T_1,
Sample : PMA, Temperature : 34°C, Repetition interval : 2.2 sec,
Resonance frequency : ν_0=25 Mc/sec,
Pulse width : t_w=7μsec,
Sweep rate : 50μsec/cm, Pulse interval : τ=140 msec,
(a) Synchroscope trigger selector set at 1,
b) Synchroscope trigger selector set at 2,
(c) Synchroscope trigger selector set at 3.

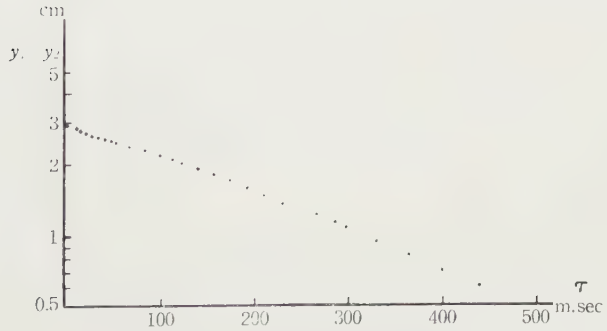

Fig. 11. Semi-logarithmic plot of difference between signal after first pulse (y_1) and that after second pulse (y_2) *versus* pulse interval τ, slope giving T_1=290msec. Data are given in Fig. 9.

The error of our measurement of T_1 is within about 10 per cent. It would come mainly from the reading error of the signal amplitude on the synchroscope screen. The failure in adjustment of 90°-90° pulse condition and the fluctuations in the shape and width of the pulsed rf magnetic field cause also error, particularly in case of narrow intense pulses.

As mentioned in Introduction, the most important points for improvement to make the apparatus applicable to the sample in rigid state are to have a narrow intense rf pulse of good wave shape, and to have a short receiver recovery time. Both are very difficult to attain, though some efforts have been done (**6**, **7**, **16**, **17**, **18**). The present apparatus, however, is sufficient for investigating the internal motion in high polymer. The full data obtained by the present apparatus will be published later.

Acknowledgements

The authors would like to express their sincere thanks to Professor I. Takahashi for his continuous interest and discussion. The authors' thanks are also due to Mr. K. Sugibuchi and other members of our laboratory for their assistance.

REFERENCES

1. See, e.g. E. R. Andrew, *Nuclear Magnetic Resonance* (Cambridge University Press, New York, 1955);
   G. E. Pake, *Nuclear Magnetic Resonance* ('Solid State Physics' edited by F. Seitz and D. Turnbull Vol. 2, Academic Press New York, 1956) p. 1;
   M. H. Cohen and F. Reif, *Quadrupole Effects in Nuclear Magnetic Resonance Studies of* ('Solid State Physics' edited by F. Seitz and D. Turnbull Vol. 5, Academic Press Inc., New York, 1957) p. 321.
2. N. Bloembergen, E. M. Purcell, and R. V. Pound, Phys. Rev., **73** (1948), 679.
3. A. G. Redfield, Phys. Rev., **98** (1955), 1786.
4. K. Tomita, Prog. Theor. Phys., **19** (1958), 541.
5. E. L. Hahn, Phys. Rev., **80** (1950), 580.
6. J. Schwartz, Rev. Sci. Instr., 28 (1957), 780.
7. J. C. Bucha, H. S. Gutowsky and D. E. Woessner, Rev. Sci. Instr., **29** (1958), 55.
8. J. Millman and H. Taub, *Pulse and Digital Circuits* (McGraw-Hill Book Company, New York, 1956) p. 187 ff. and p. 363 ff.
9. Reference 8, p. 174 ff;
   B. Chance, V. Hughes, E. F. MacNichol, D. Sayre and F. C. Williams, *Waveforms*, MIT Radiation Laboratory Series (McGraw-Hill Book Company, New York, 1949) p. 179 ff.
10. G. E. Valley and H. Millman, *Vacum Tube Amplifiers*, MIT Radiation Laboratory Series (McGraw-Hill Book Company, Inc., New York, 1948) p. 656 ff.
11. Reference **10**, p. 166 ff.
12. Reference 8, p. 140 ff.
13. Reference 8, p. 435 ff.
14. H. L. Anderson, Phys. Rev., **76** (1949), 1460.
15. E. L. Andrew and R. G. Eades, Proc. Roy. Soc., A**216** (1953), 398.
16. I. J. Lowe and R. G. Norberg, Phys. Rev., **107** (1951), 46.
17. I. Solomon, Phys. Rev., **110** (1958), 61.
18. R. J. Blume, Phys. Rev., **109** (1958), 1867.

Memoirs of the College of Science, University of Kyoto, Series A,
Vol. XXIX, No. 2, Article 8, 1959.

ON AZIMUTHAL DISTRIBUTION OF THE CRUSTAL POISSON'S RATIO IN CASE OF EARTHQUAKE OCCURRENCES (Preliminaries)

BY

Akira KAMITSUKI

(*Received June 29, 1959*)

ABSTRACT

Applying the *P*–*S* diagram analysis to some shallow earthquakes, it was found that the crustal Poisson's ratio in case of earthquake occurrence has different values in the push- and pull-zone of initial motion of seismic wave. This may be related to the state of stress accumulation causing the earthquake occurrence in the Earth's crust.

1. Introduction

By what causes an earthquake occurs is one of the most interesting problems in geophysics. Many investigators have been trying to solve this problem, but the essential of this problem still remains unsolved to the present time.

In general, the following process of earthquake occurrence may be accepted. First the stress energy is accumulated in a certain confined region of the Earth's interior, and the amount of accumulated stress approaches the limit of the strength of material in the particular part. As soon as the stress exceeds this limit, the fracture occurs and the stored energy is released in the form of elastic waves, crustal deformation, etc. (**1**, **2**, **3**, **4**). In most cases, it is assumed that the stress is accumulated uniformly in the confined region of the Earth's interior and the stored energy is released instantaneously with the emission of elastic waves.

Practically, some models of stress distribution varying azimuthally around the epicenter may be considered presuming from the data of push-pull distribution of initial motion, amplitude distribution of *P*- and *S*-waves, crustal deformation associated with the earthquake occurrence, etc. (see, e.g. **5**). Moreover, earthquakes are frequently accompanied by some aftershocks which occur in the same region with almost similar mechanism to that of the main shock. From this fact, it may be supposed that the stress accumulation is not always released instantaneously and the stored energy remains for the duration of earthquake occurrences. Recently the variation of elastic constants associated with the seismic activities has been reported in some cases (**6**, **7**).

In order to clarify the cause and mechanism of earthquake occurrences, it is very important to investigate the crustal Poisson's ratio in relation to earthquake occurrences. In the present paper, the P–S diagram method is applied to some earthquakes which occurred in the Earth's crust and the azimuthal distribution of Poisson's ratio is examined in some detail.

2. Case of the Daishoji-Oki earthquake on March 7, 1952

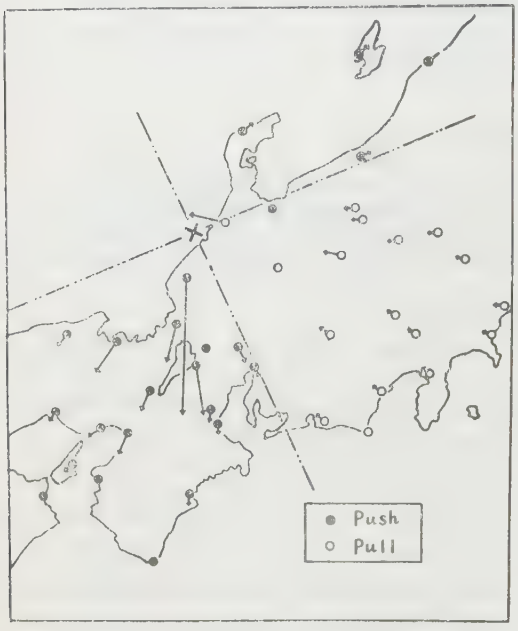

Fig. 1. The epicenter and push-pull distribution of the Daishoji-Oki earthquake on Mar. 7, 1952.

The Daishoji-Oki earthquake occurred on March 7, 1952 and was accompanied by many aftershocks. Its magnitude is reported to be 6.8 in the Bulletin of the Japan Meteorological Agency. The push-pull distribution of initial motion is shown in Fig. 1. The so-called quadrant-type pattern is ascertained in the neighbouring region of the epicenter.

The succeeding aftershocks have a similar pattern to that of the main shock. From this it may be inferred that the stress distribution causing the main shock may remain after its occurrence. The P–S diagram is shown in Fig. 2, and its data are given in Table 1.

Table 1. The Daishoji-Oki earthquake
1952 Mar. $7^d\,16^h\,32^m$ (36°28′.1 N, 136°12′.3 E; H=20 km)

Station	Push or pull	P-wave		S-wave		Δ
		Phase	Time	Phase	Time	
			m s		m s	km
Fukui	+	iP_{NE}	32 46.7	S	32 51.5	46.3
Kanazawa	−	iP_E	46.8	S	54.7	40.8
Toyama	+	P	54.3	S	33 6.2	92.6
Tsuruga	+	iP	54.7	S	6.7	91.5
Takayama	−	eP	56.0	S	10.6	100.1
Wajima	+	iP	58.5	S	14.1	119.6
Maizuru	+	iP	33 0.0	S	17.2	133.4
Hikone	+	iP	1.4	S	24.7	133.4
Gifu	+	iP	1.9	S	—	128.8
Nagoya	+	iP	4.2	S	23.1	161.2
Toyooka	+	iP	4.2	S	25.1	157.5

In Fig. 2, the points are separated into two groups according to the initial motion being either push or pull, and they are arrayed on the two branched lines. The points of stations in the pull-zone are arrayed on the upper line while the points of stations in the push-zone are arrayed on the lower line. These two lines coincide at the further part corresponding to the epicentral distances of over 150 km. The gradient of the upper line is 1.70, while that of the lower line is 1.90. Compared with the normal value of V_p/V_s in the Earth's crust ($\fallingdotseq 1.67$), it is found that the former is a little larger and the latter is much larger than the normal value. It can be safely said that this effect is attributed to the variation of crustal Poisson's ratio, because the distribution of points in the P–S diagram is not affected by any other condition than the elastic properties of the Earth's crust (8). Moreover, the two values mentioned above must be considered to be the apparent ones of V_p/V_s, reflecting upon the drawing method of the P–S diagram. And so if the origin time at the hypocenter is known, the variation of the value of V_p/V_s can be immediately obtained. Assuming that the origin time at the hypocenter is only one, being common to P- and S-waves, it slides on a straight line with 45° gradient passing through the origin of diagram. The two intersection points of this line with the two branched lines mentioned above will give the origin times of the push- and pull-motions respectively. But the difference of about 5 sec in the present case is too large to correlate with the dimension of the hypocenter. From the analysis of time-distance curve as shown in Fig. 3, the origin time is estimated to be about 32^m39^s and is plotted on the segment between two branched lines. Considering that the value of V_p/V_s in the Earth's crust must have its upper and lower limits corresponding to the state of stress accumulation, the linearity of the two branched lines will be broken at the part of left end, and the upper line will be convex upward, and the lower one downward respectively. Finally, their end points converge to one origin time. For the lack of points close to the origin-time point, this breaking of linearity is not yet ascertained.

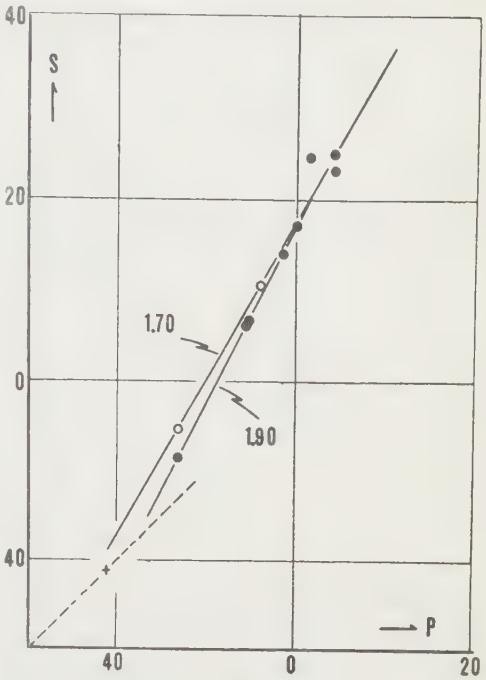

Fig. 2. The P–S diagram of the Daishoji-Oki earthquake.
(Solid circle : push, open circle : pull)

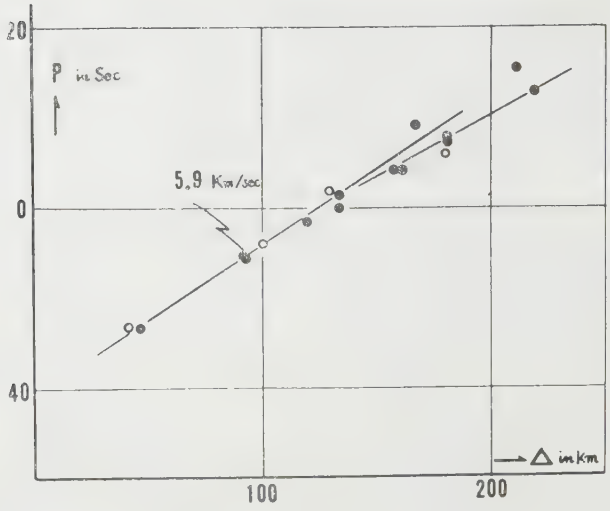

Fig. 3. The time-distance curve of the Daishoji-Oki earthquake.

From the above consideration it may be concluded that the mean value of V_p/V_s estimated along the path from the hypocenter to the station in the push-zone is at first about 1.60 and then increases with the increase of hypocentral distance, while in the pull-zone it is at first about 1.72 and then decreases with the increase of hypocentral distance, both two approaching to the normal value of 1.67. At the epicentral distances of over 150 km they coincide within the observation accuracy. The distance of the point of coincidence of the two branched lines and the deviation of the apparent value of V_p/V_s from the normal one may be correlated to the earthquake magnitude and the state of stress accumulation. This fact is ascertained by comparison of the case of Daishoji-Oki earthquake with that of Tokushima earthquakes treated in the next section.

In several aftershocks which occurred succeeding to the main shock, the above-stated effect still remains but its amount becomes considerably small. This may correspond to the releasing rate of stress accumulation after the occurrence of the main shock.

3. Some examples in other regions

In Shikoku, especially in the Tokushima Pref., shallow earthquakes have frequently occurred from about 1950. Their magnitudes are estimated to be from about 4 to 5. Among them the earthquake which occurred on July 27, 1955 has the largest magnitude of 6.0 Some earthquakes which occurred before and after this earthquake are examined concurrently.

Table 2. The earthquake on Apr. $10^{d}\ 11^{h}\ 9^{m}\ 12^{s}$
(34.1 N, 134.2 E ; H=10 km ca.)

Station	Push or pull	P-wave		S-wave		Δ
		Phase	Time	Phase	Time	
			m s		m s	km
Tokushima	−	*iP*	9 20.1	*iS*	9 24.8	35.2
Takamatsu	+	*iP*	23.6	*iS*	28.7	27.8
Sumoto	−	*iP*	26.9	*iS*	35.5	70.4
Wakayama	(−)	*eP*	29.8	*eS*	41.7	92.6
Okayama	+	*iP*	29.9	*iS*	39.4	68.6
Kochi	−	*iP*	30.0	*iS*	40.1	87.1
Murotomisaki	+	*iP*	32.1	*S*	42.4	96.4
Kobe	+	*P*	35.4	*iS*	48.4	111.2

Table 3. The earthquake on May $18^{d}\ 13^{h}\ 39^{m}\ 24^{s}$
(33.8°N, 134.3°E ; H=0～20 km)

			m s		m s	km
Tokushima	−	*iP*	39 31.8	*iS*	39 37.3	40.8
Takamatsu	+	*iP*	36.0	*iS*	43.4	61.2
Murotomisaki	+	*iP*	36.4	*S*	43.2	63.0
Kochi	−	*iP*	37.6	*iS*	46.9	76.0
Sumoto	−	*iP*	40.1	*iS*	50.7	83.4
Wakayama	(−)	*iP*	40.8	*iS*	52.9	92.6
Okayama	+	*iP*	43.0	*iS*	55.0	105.6
Shionomisaki	(−)	*eP*	43.9	*iS*	40 0.7	140.8

Table 4. The earthquake on July $27^{d}\ 10^{h}\ 20^{m}\ 49^{s}$
(33.75°N, 134.3°E ; H=0～10 km)

			m s		m s	km
Tokushima	+	*iP*	20 58.5	*iS*	21 3.6	44.5
Murotomisaki	+	*iP*	21 0.9	*iS*	6.6	57.4
Takamatsu	+	*iP*	2.6	*iS*	12.5	66.7
Sumoto	+	*iP*	3.6	—	—	87.1
Kochi	−	*iP*	3.9	*iS*	11.0	74.1
Wakayama	(−)	*iP*	8.7	*iS*	18.3	105.6
Okayama	+	*iP*	10.5	*iS*	24.5	109.3
Kobe	(+)	*iP*	14.1	*iS*	29.5	131.6

(Parenthesized data of *Push or Pull* were presumed from the horizontal motions.)

As shown in Figs. 4 and 5, similar effects to the case of the Daishoji-Oki earthquake are found clearly. The rate of V_p/V_s-variation with the increase of hypocentral distance is smaller than that discussed in section 2. And the distance at which two branched lines coincide is also smaller. This is reasonably accepted, considering the difference of magnitudes of the earthquakes concerned.

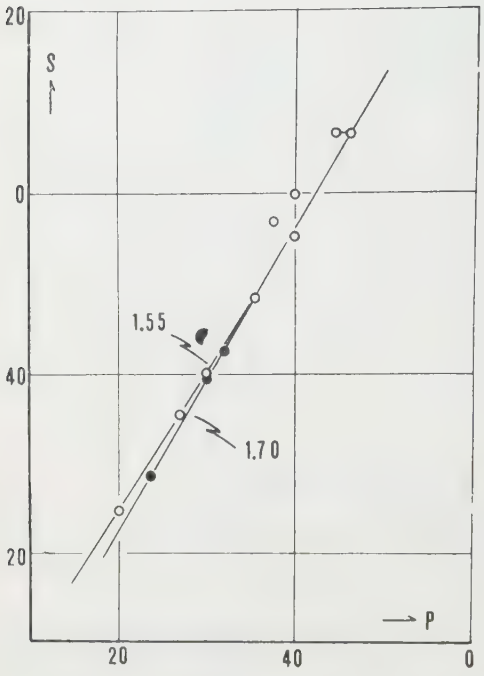

Fig. 4. The *P–S* diagram of the earthquake on Apr. $10^{d}\ 11^{h}\ 9^{m}\ 12^{s}$.

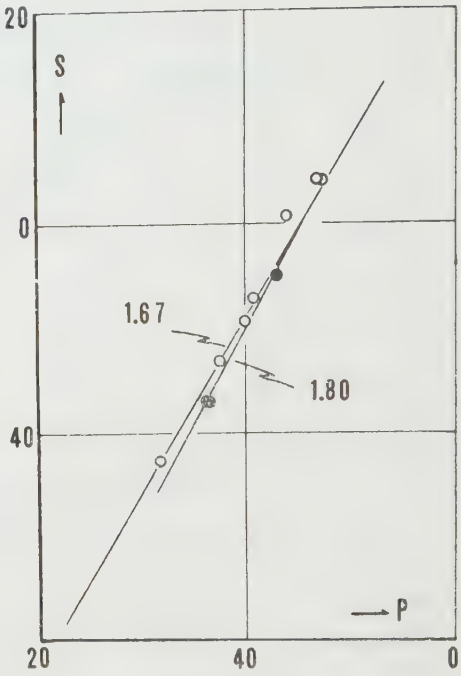

Fig. 5. The *P–S* diagram of the earthquake on May $18^{d}\ 13^{h}\ 39^{m}\ 24^{s}$.

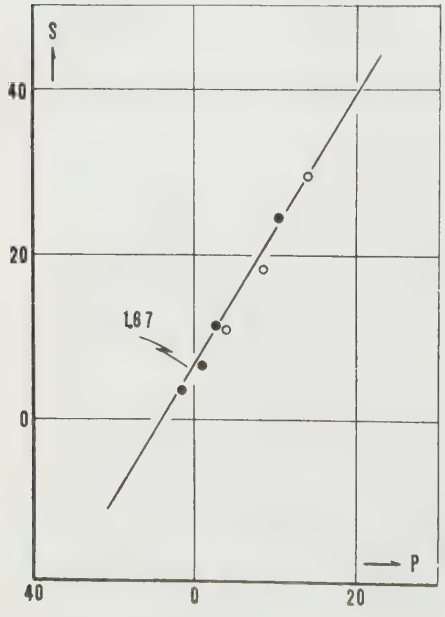

Fig. 6. The *P–S* diagram of the earthquake on July $27^{d}\ 10^{h}\ 20^{m}\ 49^{s}$.

The *P–S* diagram of the earthquake occurred on July 27, 1955 is shown in Fig. 6. Owing to the deficiency of good observation condition, the data are not favourable, and its seems probable that the effect is inverse in regard to push- and pull-zones as compared with the previous cases. This tendency is frequently seen in the cases of some earthquakes which occurred after this main shock. This fact must be investigated in future with more abundant data.

In the previous paper (8), some rather deep earthquakes were examined using the *P–S* diagram analysis and it was ascertained that the crustal Poisson's ratio shows no local anomaly in the Shikoku region. And so the above-stated effects must be attributed to the variation of crustal

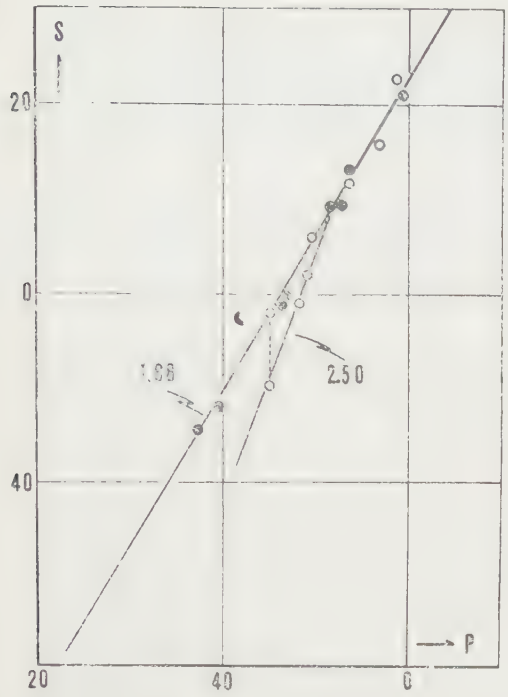

Fig. 7. The P–S diagram of the Fukui earthquake on June 28, 1948.

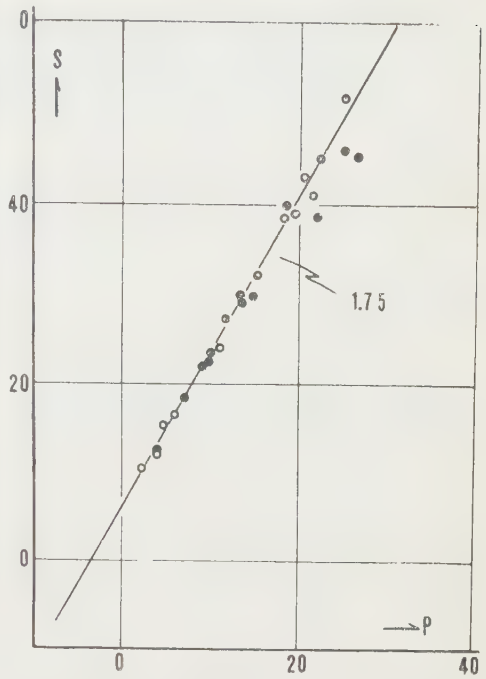

Fig. 8. The P–S diagram of the Yoshino earthquake on July 18, 1952.

Poisson's ratio in case of earthquake occurrences.

On June 28, 1948, the Fukui earthquake occurred. Its focal depth and magnitude are estimated to be about 20 km and 7.0 respectively. The P–S diagram is shown in Fig. 7. The two branched lines are drawn, but the effect is inverse in regard to the push- and pull-zones as compared with the case of the Daishoji-Oki earthquake. The point of Gifu station (pull) is on the line of push-zone station. It may perhaps be attributed to the ambiguity of S-phase identification.

On July 18, 1952, the Yoshino earthquake occurred. Its focal depth and magnitude (M_G) are estimated to be 70 km and 7.0 respectively. In Fig. 8, any conspicuous effect cannot be found in spite of its large magnitude. This may perhaps be due to its greater depth of origin and occurrence mechanism of another type.

4. Summary

Using the P–S diagram method, the azimuthal distribution of the crustal Poisson's ratio in case of earthquake occurrences is investigated. It is favourable that the value of Poisson's ratio obtained by this method depends only on the elastic preperties of the Earth's crust. Some shallow earthquakes which occurred with the so-called

quadrant-type distribution of intial motion are examined and the value of Poisson's ratio is found to be considerably different in the push- and pull-zones. The correlation between its variation mode and the push-pull sense is, however, not decided uniquely. This may be related to the partition of stress energy causing the *P*- and *S*-waves.

In the last part of section 3, the Yoshino earthquake whose focus is situated below the Mohorovičić discontinuity is treated. But in this case any conspicuous effect cannot be found. This may perhaps be due to its greater depth and occurrence mechanism of another type.

The problem of stress accumulation in the Earth's crust is very interesting in relation to the earthquake occurrences and so it is desirable to investigate this problem in more detail with more abundant data.

Acknowledgments

The writer wishes to express his hearty thanks to Prof. E. Nishimura for his kind guidance and encouragement throughout the present study. The writer is also deeply indebted to the Directors and Members of the Japan Meteorological Agency for their generous permission for copying seismograms obtained at their observatories. The cost of the present study was partly defrayed by a grant-in-aid for scientific research of the Ministry of Education.

REFERENCES

1. H. Benioff, Seismic evidence for the fault origin of oceanic deeps, Bull. Geol. Soc. America, **60** (1949), 1837–1856.
2. T. Matuzawa, Feldtheorie der Erdbeben, Bull. Earthq. Res. Inst. **31** (1953), 179–201.
3. C. Tsuboi, Earthquake energy, earthquake volume, aftershock area, and strength of the Earth's crust, J. Phys. Earth, **4** (1956), 63–66.
4. K. Kasahara, The nature of seismic origins as inferred from seismological and geodetic observations, Bull. Earthq. Res. Inst., **35** (1957), 473–532; **36** (1958), 21–53.
5. H. Honda, *The Seismic Waves* (2nd ed., Iwanami-Shoten, 1954), (in Japanese).
6. K. Sassa, *Earthquakes and Disasters* (Kobunsha, 1948), (in Japanese).
7. E. Nishimura, On change of state of the materials in the Earth's crust with relation to seismic activity, Bull. Disaster Prevention Res. Inst., Mem. Issue, (1956), 8–13.
8. A. Kamitsuki, On local character of Poisson's ratio in the Earth's crust, Mem. Coll. Sci. Kyoto Univ., **29** (1959), 163–186.

Memoirs of the College of Science, University of Kyoto, Series A,
Vol. XXIX, No. 2, Article 9, 1959.

A CONSIDERATION ON GENERATION MECHANISM OF LOCAL EARTHQUAKES

BY

Takeshi MIKUMO

(*Received July 8, 1959*)

ABSTRACT

The mechanism of occurrence of local earthquakes generated in Wakayama District was studied from the "push-pull" pattern of initial motions and the amplitude distributions of the *P*- and *S*-waves. It may safely be explainable to be of a conical type rather than a quadrant one.

A consideration on the former type of mechanism may suggest an azimuthal difference in the dimension of focal region.

1. Introduction

The study on the mechanism of earthquake occurrence, based on the distribution of dilatation and compression of seismic initial motions, may be one of the most interesting and important problems in seismology. This problem has already been studied by many seismologists and many brilliant results have been piled up. The progresses of these researches are historically reviewed by some Japanese seismologists in their elaborate papers (**1**, **2**).

Nowadays, it is generally accepted, from the excellent investigations hitherto made, that there exist several kinds of types in the geographical "push-pull" distributions of the initial motions: the predominant one is a quadrant type.

This is such a case in which the "push-pull" distribution or the pattern of the initial anaseismic and kataseismic movements is divided into quadrants by two nodal planes intersecting perpendicularly at the focus. This type of distribution was found first by T. Shida in 1917 and was called "the crack-earthquake" by himself. Many seismologists paid increasing attention to his discovery and this was a first step in Japan towards the study on the mechanism of earthquakes.

According to a series of studies made especially in our country, it was ascertained theoretically that the quadrantal push-pull distribution could be caused by a couple of compressional and tensile stresses working perpendicularly at the origin (**2**), or even by a uniform shear stress resulting in a single fracture (**3**). The so-called "fault-plane" solution (**4**, **5**) belongs also to this broad category.

Another case is, on the other hand, a conical type in which the nodal curves on the Earth's surface for the pattern of condensation and rarefaction of the initial motions can be expressed as a kind of conical section. The case was detected by

Tanahashi in a deep-seated earthquake in 1931. Some investigators confirmed thereafter the existence of this type, and one of them gave a first theoretical explanation to this sort of distribution. The theoretical studies on the mechanism of occurrence which causes a conical type distribution will be mentioned subsequently.

In contrast to the case of great earthquakes, we can find only a few investigations (**6**, **7**, **8**, **9**, **10**) about the generation mechanism of minor earthquakes, such as local shocks or aftershocks.

In 1954 and 1956, seismometric observations were carried out in the epicentral region of local earthquakes in Wakayama District (**11**) for the purpose of clarifying the unsolved natures of micro-earthquakes and presuming the crustal structure in the area concerned. The results obtained in these observations may be considered to have offered a clue to the above-mentioned problems.

In the present paper, the mechanism of earthquake occurrence will be studied in some detail, not only from the aspect of the push-pull pattern of initial *P*-waves but also from comparison of the amplitudes recorded at each station with the theoretical distribution of the amplitudes of the longitudinal and transversal waves. We shall investigate that the generation mechanism for these shocks is interpreted to be of which type stated above, and we shall make some considerations on the origin of the earthquakes.

2. Observed data

The data used in the present study are a great number of seismograms recorded in the observations in 1954 and 1956 at our six stations : Idakiso, Wakanoura, Fuyuno, Nokami, Kainan and Yoro, and several observatories of the Earthquake Research Institute of Tokyo University. All of these stations were selected so as to be situated in a metamorphic rock zone within the epicentral area of about 10 km in radius, taking Kainan City as its centre. The positions of the observation stations and the epicentres of earthquakes mentioned in this analysis were shown in the previous paper. In these observations, some ten local shocks were clearly recorded by the electromagnetic seismometers of variable reluctance type of 0.45 sec in natural period connected with the galvanometer of 0.40 sec in free period.

The push-pull distribution of initial motions in every earthquake was here studied by use of the data obtained at the respective stations. When the nodal curves were tentatively assumed to be a pair of lines (**11**), the distribution indicated a type similar to the quadrant one in the case of very shallow earthquakes (**6**). But in many cases the nodal lines do not always cross at right angles or do not intersect at the epicentre. Upon reconsidering the matter, the focal depths for most of these earthquakes were determined to be as shallow as 4～10 km, but are of comparable order with their epicentral distances. Hence, when these shocks are regarded as an earthquake analogous to the "deep-focus earthquake" in the ordinary sense, the push-pull distribution in most cases will be understandable to be a quadrant type.

A closer examination shows, however, that it can reasonably be explained to be rather of a conical type, if the previously assumed nodal curves were redetermined. Fig. 1 shows several examples of the push-pull distribution in the case of conical type.

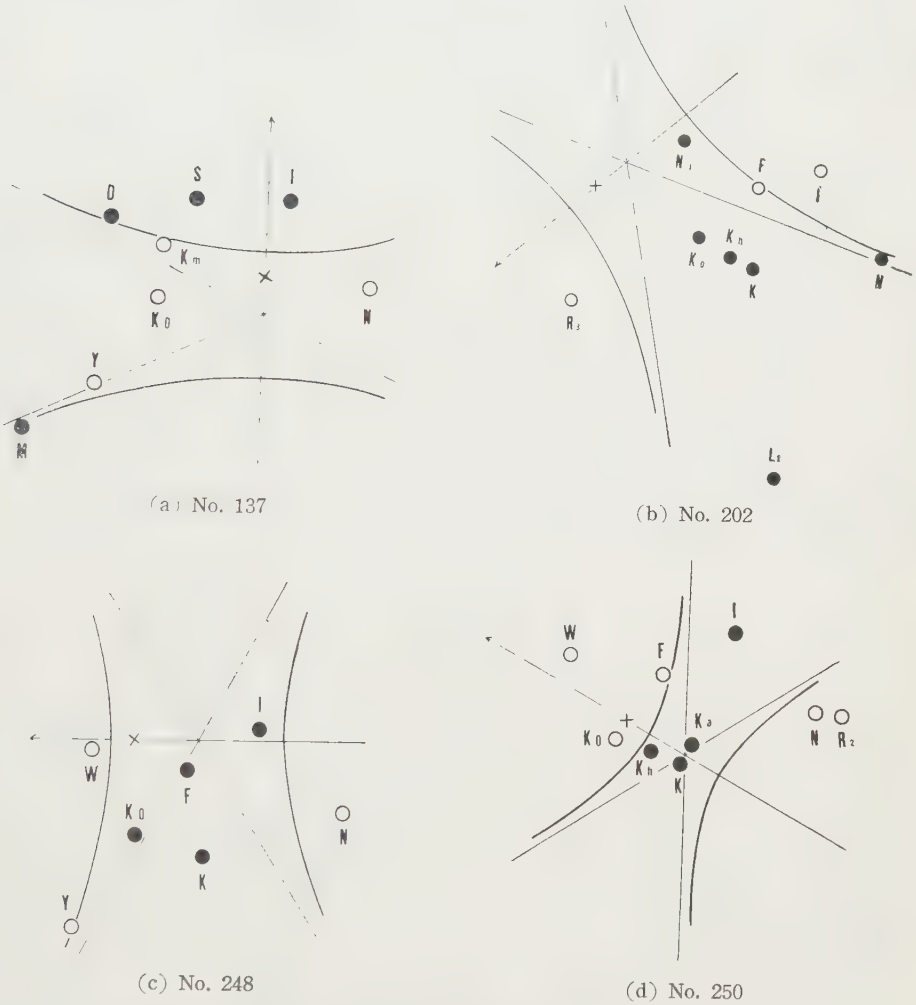

Fig. 1. Examples of push-pull distribution of initial motions.
(○: push, ●: pull)

Naturally, it is difficult to conclude solely from the push-pull pattern, without any study on the amplitude distribution of the *P*- and *S*-waves, that the mechanism of these local shocks corresponds to either type of the two. We are probably allowed, however, to suppose that the local earthquakes in this region may have a mechanism bearing a conical type distribution. For this reason, the already-made theoretical studies

will be reviewed in the next paragraph, in order to clarify in what cases this type of distribution can arise.

3. A brief review of the past theoretical studies on conical type distribution

On the mechanism with push-pull distribution of a conical type, some Japanese seismologists, such as Ishimoto, Kawasumi, Inouye, Takagi, Usami and Hirono have made theoretical studies in various cases.

M. Ishimoto (**12**) investigated practical examples of the push-pull pattern in many earthquakes and came to the conclusion that in all cases the nodal curves for distribution of the initial movements are represented by a conical section with push-sense inside. For this mechanism, he proposed such an origin-model that was composed of two zonal harmonics, $P_2(\cos\theta)$ (quadruple source) and $P_0(\cos\theta)$ (single source), which are particular solutions of the fundamental equation of propagation of spherical waves. This is the well-known hypothesis called "magma intrusion theory."

Following Ishimoto's idea, H. Kawasumi (**13**) made more detailed theoretical and practical studies. He investigated theoretically, by an excellent method, the propagation of spherical waves in a homogeneous isotropic medium, obtaining the same solution as Sezawa's (**14**). Namely, his general solutions for the equations $(\nabla^2+h^2)\phi=0$, $(\nabla^2+k^2)\psi=0$ (where $h^2=\rho p^2/(\lambda+2\mu)$, $k^2=\rho p^2/\mu$) are expressed by

$$\begin{cases} \phi=\sum_{n=0}^{\infty}\sum_{m=0}^{\infty}A_{nm}\dfrac{H^{(2)}_{n+1/2}(hr)}{\sqrt{r}}P_n^m(\cos\theta)\sin(m\varphi+\varepsilon)\,, \\ \psi=\sum_{n=0}^{\infty}\sum_{m=0}^{\infty}B_{nm}\dfrac{H^{(2)}_{n+1/2}(kr)}{\sqrt{r}}P_n^m(\cos\theta)\sin(m\varphi+\varepsilon)\,, \end{cases}$$

where ϕ and ψ are scalar- and vector-potentials respectively, and the displacements in all directions can be derived from these quantities. Kawasumi dealt especially with the conical type distribution corresponding to the case of $n=2$ and $m=0$ in the above solutions, and compared the observed values at each station with the theoretical amplitudes of the longitudinal and transversal waves, taking the effects due to crustal structure into consideration.

In addition, the case of $n=2$ and $m=2$ in the above or Sezawa's solution is equivalent to the type studied by Matuzawa (**15**) and Hasegawa (**16**), and the case of $n=2$ and $m=1$ to the type discussed by Honda (**17**). These cases correspond to a quadrant type.

On the other hand, W. Inouye (**18**) studied the behaviour of the dilatational waves generated from a model of seismic origin, in which the normal pressure varying periodically on the surface of spherical cavity can be represented by the sum of two zonal harmonics $P_0(\cos\theta)e^{ipt}$ and $P_2(\cos\theta)e^{ipt}$. He also elucidated that the displacement at large distances is of the conical type distribution when the wavelengths of

the longitudinal waves are of comparable order with the dimension of seismic origin.

S. Takagi (**19**) calculated theoretically the radial displacement of elastic waves emitted from the same cavity as mentioned above when the outward normal force of harmonic, aperiodic or hydrostatic type acts on a pole, two poles or equatorial plane of the source, and confirmed that the azimuthal distribution of the initial amplitudes can be expressed in most cases as a combination of $P_0(\cos\theta)$ and $P_2(\cos\theta)$, indicating a conical type.

Moreover, T. Usami and H. Hirono (**20, 21**) recently investigated the amplitude distribution of the dilatational and distortional waves generated from a prolate or oblate spheroidal cavity in an infinite elastic medium when hydrostatic pressure or a force of harmonic type is applied on the surface of the cavity. As a result of numerical calculations, it was found that at a distant point the push-pull distribution of conical type was produced in a radial displacement of P-waves in the case of certain shapes of cavity and values of wavelength.

It is to be remarked that the conical type distribution with pull-sense inside can be found in the cases treated by Usami and Takagi.

We shall now analyse our observed data referring to the above-described theories.

4. Determination of the vertical angle of nodal cone and the inclination of its polar axis from data of push-pull distribution

Now, the nodal curves on the Earth's surface in a conical type distribution are represented, in general, by a hyperbola or an ellipse. Their shape and dimension depend upon the angle of vertex of the nodal cone, the inclination of its polar axis and the depth of hypocentre. Ishimoto, Kawasumi and Minakami (**22**) suggested the possibility of determining the axial inclination of the cone or the focal depth from the form of the curves. In this case they supposed a constancy of the vertical angle of cone, but this is functionally related with the ratio of wavelength to the dimension of the origin, in the cases investigated by Usami and Inouye. Furthermore, the shapes of nodal curves are known to be of complicated styles deformed from a conical section, if the effects due to discontinuity surfaces in the crust are taken into account (**13, 22, 23**).

Here, for the sake of simplicity, the crust mentioned in this analysis is assumed to be of a uniform medium. Under this assumption, the vertical angle and axial inclination of nodal cone will be determined from data of push-pull distribution. This is attributable to a simple problem in analytical geometry. Takagi (**23**) has already studied the present problem, but more definite expressions to estimate the above unknowns can be obtained in our case.

We shall first consider an orthogonal left-hand coordinate system $x'y'z'$, taking a hypocentre (strictly, a centre of focal region) as the origin of the coordinates, the

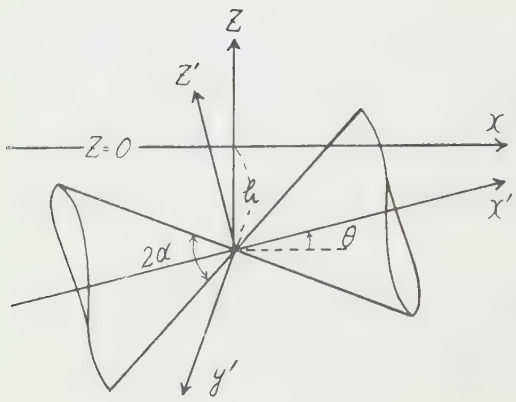

Fig. 2.

polar axis of a nodal cone as the x'-axis, and an axis parallel to the ground surface as the y'-axis (Fig. 2).

The equation of the nodal cone with the vertical angle 2α is expressed as follows:

$$-x'^2\tan^2\alpha+y'^2+z'^2=0. \quad (1)$$

Next, another coordinate system xyz having the epicentre as its origin is taken in such a way that the xy-plane coincides with the ground surface and the y-axis is parallel to y'. Then, the equation of the cone referred to the xyz-system becomes

$$(\tan^2\alpha-\tan^2\theta)x^2+2x(z+h)\sec^2\alpha\tan\theta-y^2\sec^2\theta-(1-\tan^2\alpha\tan^2\theta)(z+h)^2=0, \quad (2)$$

where θ is the angle of inclination to the ground surface and h the focal depth. The conical section on the surface can immediately be obtained by putting $z=0$ in Eq. (2). Thus,

$$(\cos 2\theta-\cos 2\alpha)x^2+2h\sin 2\theta\cdot x-(1+\cos 2\alpha)y^2=(\cos 2\theta+\cos 2\alpha)h^2. \quad (3)$$

(1) *Case of* $0\leqq\theta<\alpha$

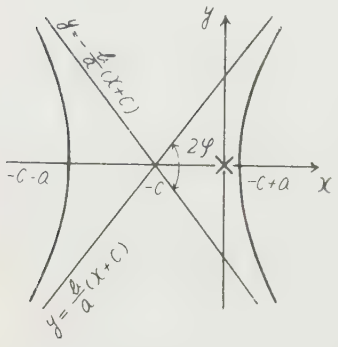

Fig. 3.

Eq. (3) can be rewritten in the form:

$$\frac{(x+c)^2}{a^2}-\frac{y^2}{b^2}=1, \quad (4)$$

where

$$\left.\begin{aligned} a^2&=\left(\frac{\sin 2\alpha}{\cos 2\theta-\cos 2\alpha}\right)^2h^2,\\ b^2&=\frac{2\sin^2\alpha}{\cos 2\theta-\cos 2\alpha}h^2,\\ c&=\frac{\sin 2\theta}{\cos 2\theta-\cos 2\alpha}h. \end{aligned}\right\} \quad (5)$$

Consequently, the nodal curve on the surface expressed by Eq. (4) is a hyperbola as shown in Fig. 3. In this case the epicentre lies on the axis of symmetry traversing the curves. Let the angle of intersection of the asymptotes of the hyperbola (4) be denoted by 2φ. Then we obtain

$$\tan^2\varphi=\left(\frac{b}{a}\right)^2=\frac{\cos 2\theta-\cos 2\alpha}{1+\cos 2\alpha}. \quad (6)$$

a) When the focal depth h, the angle of intersection of the asymptotes 2φ and

the distance c between the epicentre and the point of intersection of the asymptotes are determined from observation, we get θ and α from Eqs. (5) and (6) as:

$$\tan\theta = c\sin^2\varphi/h\,, \tag{7}$$

$$\cos\alpha = \cos\varphi\cos\theta\,. \tag{8}$$

b) When h, 2φ, and the distance a between the epicentre and the nearer vertex of the nodal curve are estimated, α and θ can be determined from the following formulae:

$$\tan\alpha = a\tan^2\varphi/h\,, \tag{9}$$

$$\cos\theta = \cos\alpha/\cos\varphi\,. \tag{8'}$$

Here, the following relationship needs to hold in the above two cases:

$$\frac{c}{a} = \frac{\sin 2\theta}{\sin 2\alpha}\,. \tag{10}$$

c) When we can determine h, c and a, α and θ can easily be obtained from Eqs. (5) and (10), as follows:

$$\tan 2\alpha = 2p/(p^2-q^2-1)\,, \tag{11}$$

$$\tan 2\theta = 2q/(p^2-q^2+1)\,, \tag{12}$$

where $p=a/h$ and $q=c/h$. In this case Eq. (8) is required to hold.

(2) Case of $\alpha<\theta\leqq\pi/2$

In this case, the nodal curve becomes an ellipse shown in Fig. 4, and α and θ can be obtained in the same way as in the former case, by determining the longer and shorter axes or their ratio and the distance between the epicentre and the centre of the ellipse.

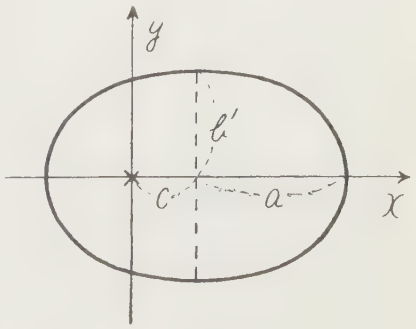

Fig. 4.

In the special case of $\theta=\alpha$ the nodal curve becomes a parabola, while in the case of $\theta=\pi/2$, it becomes a circle.

In short, the vertical angle and the axial inclination of the nodal cone can be estimated from the push-pull distribution of initial motions, by determining beforehand the focal depth by a travel-time analysis. Estimation of these quantities, however, will inevitably be attended with considerable errors, unless a sufficiently dense net of observation stations is spread over the area concerned. In our case, nodal curves in some possible extreme cases were examined and their mean values were adopted.

The results obtained by applying the above-described method to our data in 28

Table 1. Vertical angle and inclination angle of nodal cone in every earthquake.

Shock No.	h (km)	Φ_N	a (km)	c (km)	φ	α	θ
121	11.2	108° ± 19°	5.0 ± 0.7	2.2 ± 0.7	67° ± 4°	67° ± 4°	7° ± 2°
122	3.7	204 ± 15	2.0 ± 0.3	0.9 ± 0.3	63 ± 3	64 ± 4	11 ∓ 2
123	3.3	171 ± 18	2.0 ± 1.1	0.8 ∓ 0.8	59 ± 15	60 ± 16	10 ± 10
135	4.6	15 ± 12	2.7 ± 0.3	0.4 ± 0.2	61 ± 4	61 ± 4	4 ∓ 2
136	4.7	136 ± 7	4.8 ± 0.8	5.0 ∓ 0.5	53 ± 8	59 ± 8	32 ± 6
137	5.1	0 ± 2	3.0 ± 0.2	2.0 ± 0.2	62 ± 2	63 ± 2	17 ∓ 2
140	6.3	0 ± 20	3.3 ± 0.7	5.5 ± 0.7	68 ± 4	72 ± 3	35 ± 6
151	5.8	14 ± 22	2.9 ± 0.9	3.8 ∓ 0.9	67 ± 7	69 ± 10	39 ± 8
201	10.3	5 ± 30	8.0 ± 1.0	1.0 ± 1.0	52 ± 2	53 ± 3	4 ± 4
202	6.2	140 ± 5	4.0 ± 0.8	2.0 ∓ 0.9	58 ± 8	60 ± 9	14 ± 7
206	9.3	278 ± 13	5.0 ± 2.5	5.0 ± 2.5	64 ± 11	67 ± 10	24 ∓ 10
207	3.6	303 ± 28	2.9 ± 1.1	0.8 ± 1.1	58 ± 15	59 ± 15	11 ± 4
217	7.9	93 ± 3	1.4 ± 0.2	6.4 ± 0.3	81 ± 3	83 ± 2	38 ∓ 2
218	5.6	154 ± 22	2.7 ± 0.6	3.3 ∓ 0.6	66 ± 15	70 ± 13	27 ± 10
220	5.1	270 ± 11	4.4 ± 0.6	0.0 ∓ 0.5	49 ± 5	49 ± 5	0 ± 4
222	4.4	318 ± 27	3.5 ± 2.3	4.0 ± 2.5	59 ± 17	64 ± 13	31 ∓ 15
223	5.2	92 ± 11	2.1 ± 0.5	3.2 ± 0.3	69 ± 6	73 ± 5	29 ∓ 2
224	8.9	358 ± 20	3.6 ± 1.9	2.8 ± 2.0	69 ± 10	70 ± 10	15 ∓ 10
226	7.4	187 ± 8	3.4 ± 0.8	0.8 ± 0.8	65 ± 4	66 ± 3	5 ± 5
228	7.3	318 ± 23	5.8 ± 0.3	0.0 ± 3.5	52 ± 5	52 ± 3	0 ± 15
230	8.4	334 ± 3	5.0 ± 0.8	4.7 ± 0.8	61 ± 5	64 ± 3	24 ∓ 3
236	6.3	252 ± 10	4.1 ± 1.8	1.7 ± 1.7	57 ± 5	58 ± 4	11 ∓ 7
247	12.0	214 ± 20	6.0 ± 2.4	2.0 ± 2.0	64 ± 9	64 ± 7	8 ∓ 8
248	4.6	89 ± 4	4.1 ± 0.8	2.9 ± 1.5	56 ± 10	58 ± 4	24 ± 10
249	8.8	174 ± 10	3.6 ± 1.0	2.7 ± 0.8	68 ± 6	69 ± 5	20 ± 2
250	3.7	58 ± 8	2.0 ± 0.4	2.9 ± 0.6	67 ± 3	70 ± 2	33 ∓ 6
251	5.3	305 ± 33	4.0 ± 1.0	5.5 ± 0.5	61 ± 10	68 ± 10	38 ∓ 6
253	6.6	181 ± 18	4.6 ± 2.6	2.4 ± 2.4	57 ± 17	58 ± 15	14 ∓ 14

α: the vertical angle of nodal cone; θ: the inclination of polar axis of the cone; Φ_N: the axial orientation of nodal cone measured from northward.

earthquakes are tabulated in Table 1. Eqs. (11) and (12) were used in the present case. The errors in α and θ do not exceed 10° for most of the shocks.

5. Amplitude distribution in the case of conical type

In this section, the amplitude distribution will be calculated theoretically from the data listed in Table 1, and will be compared with the amplitudes observed at each station.

As reviewed in § 3, theoretical studies on various mechanisms causing the distribution of conical type have been made. In almost all the cases mentioned there, the azimuthal distribution of radial and tangential displacements at large distances, as compared with the wavelength, can exactly or approximately be expressed by a combination of spherical harmonic functions: $a_0P_0(\cos\eta)+a_2P_2(\cos\eta)$ and $bP_2^1(\cos\eta)$ respectively, with arbitrary constants a_0, a_2 and b (**12, 13, 18, 19, 20, 21**). It can safely be regarded also in Usami's model that the distribution approaches the above form with fairly good accuracy.

Hence in these cases, the radial amplitude, u, and tangential one, v, on a spherical surface with radius r can be represented by the following form in terms of the vertical angle of the nodal cone, 2α:

$$\left.\begin{aligned} u &\propto a_0P_0(\cos\eta)+a_2P_2(\cos\eta) = A\cos 2\eta+B = 2A(\cos^2\eta-\cos^2\alpha)\,, \\ v &\propto C\sin\eta\cos\eta\,, \end{aligned}\right\} \qquad (13)$$

where η is the angle measured from the polar axis.

We shall here consider two spherical coordinates referred to the $x'y'z'$-system as in the preceding section, and the $\bar{x}\bar{y}\bar{z}$-system having a common origin with the former. The latter is taken in such a way that each of them is parallel to each exis of the xyz-system. When the angles, Θ', Φ' etc. are measured as indicated in Fig. 5, we get, $x'=r\cos\Theta'\cos\Phi'=r\cos\eta$, $z'=r\sin\Theta'$ and $\bar{x}=r\cos\Theta\cos\Phi$, $\bar{z}=r\sin\Theta$. From the relation between the two systems: $x'=\bar{x}\cos\theta+\bar{z}\sin\theta$, η can be connected with Θ and Φ as follows:

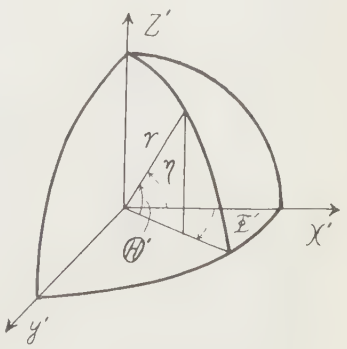

Fig. 5.

$$\cos\eta = \cos\Theta'\cos\Phi' = \cos\Theta\cos\Phi\cos\theta+\sin\Theta\sin\theta\,. \qquad (14)$$

For the xyz-system, we have

$$x = \Delta\cos\Theta\cos\Phi\,, \quad h = \Delta\sin\Theta\,, \quad (\Delta^2 = x^2+y^2+h^2)\,,$$

Δ being the hypocentral distance.

When elastic waves emitted from a focus are propagated in the form of spherical

waves, their divergence factor of amplitude is found to be $1/\Delta$. Taking account of this factor, the amplitudes of the initial P- and S-waves, A_P and A_S, which will be observed at a distant station on the Earth's surface, are expressible by the following formulae, under the assumption of uniform medium:

$$A_P = \frac{2A_{P0}}{\Delta}\left[(\cos\Theta\cos\Phi\cos\theta + \sin\Theta\sin\theta)^2 - \cos^2\alpha\right] \tag{15}$$

$$= \frac{2A_{P0}}{\Delta}\left[\left(\frac{x\cos\theta + h\sin\theta}{\Delta}\right)^2 - \cos^2\alpha\right], \tag{16}$$

$$A_S = \frac{A_{S0}}{\Delta}\left(\frac{x\cos\theta + h\sin\theta}{\Delta}\right)\sqrt{1-\left(\frac{x\cos\theta + h\sin\theta}{\Delta}\right)^2}. \tag{17}$$

A_{P0} and A_{S0} depend upon the earthquake magnitude. Naturally, the nodal curves expressed by Eq. (3) are equivalent to the case of $A_P = 0$ in the above formula.

While, the following relations hold between the amplitude of the incident P- or SV-waves and that with the vertical component, A_{PV} or A_{SV}, and the horizontal component, A_{PH} or A_{SH}, which will be observed on the ground surface. That is,

$$\left.\begin{aligned} A_{PV}/A_P &= f_P(i_P), \quad A_{PH}/A_P = g_P(i_P), \\ A_{SV}/A_S &= f_S(i_S), \quad A_{SH}/A_S = g_S(i_S), \end{aligned}\right\} \tag{18}$$

where i_P and i_S are the incident angles of the P- and SV-waves respectively. Since values of these functions have already been calculated in terms of Poisson's ratio (**24**, **25**), the amplitudes which will be recorded on the surface can be estimated excepting A_{P0} and A_{S0}.

a) Then, the ratio of the vertical component of theoretical amplitude of the P-waves at any station to that at a standard observatory is given by

$$\frac{A_{PV(j)}}{A_{PV(0)}} = \left(\frac{f_P(i_j)/\Delta_j}{f_P(i_0)/\Delta_0}\right)\cdot\frac{(x_j\cos\theta + h\sin\theta)^2/\Delta_j^2 - \cos^2\alpha}{(x_0\cos\theta + h\sin\theta)^2/\Delta_0^2 - \cos^2\alpha}. \tag{19}$$

b) The ratio of the vertical components of theoretical amplitudes of the P- and SV-waves at each station is,

$$\frac{A_{SV}}{A_{PV}} = \frac{f_S(i_j)}{f_P(i_j)}\cdot\frac{k\sin\eta_j\cos\eta_j}{\cos^2\eta_j^2 - \cos^2\alpha}. \tag{20}$$

We can easily calculate the above ratios, when h, $f_{P,S}(i_j)$ and Δ_j were estimated from the determination of hypocentre, and α, θ and x_j from the push-pull distribution of initial waves.

Table 2 gives the theoretical amplitudes of the P- and SV-waves or their ratios calculated for every earthquake, and the corresponding observed values at respective observatories. The angle of incidence was calculated by $\cos i = h/\Delta$ ($i = i_P = i_S$). The observed value corresponding to Eq. (20) was taken by the amplitudes' ratio of initial

Table 2. Theoretical and observed amplitudes.

No.	St.	Δ_j (km)	i_j	$f_p(i)$	$f_s(i)$	A_{PV}/A_{P0} ×100 (C)	A_{PV}/A_{P0} ×100 (Q)	$\bar{A}_{PV}$ (mm)	$\lvert A_{SV}/A_{PV}\rvert$ (C)	$\lvert A_{SV}/A_{PV}\rvert$ (Q)	$\lvert \bar{A}_{SV}/\bar{A}_{PV}\rvert$
201	I	28.6	69°	0.79	0.92	1.45		1.40	0.68		(0.72)
	K	23.1	64	0.91		1.82		2.30			
	N	25.6	66	1.74		1.92		1.40			
	Y	21.3	61	0.97	1.12			5.05	1.42		(1.32)
207	K	4.9	44	1.39	1.48	6.36		3.60	0.91		0.42
	N	9.5	68	1.73		−5.97		− 2.10			
	Y	7.8	63	0.94	1.08	−3.09		− 1.20	2.25		1.75
217	W	8.0	7	1.97				2.05			
	F	9.5	34	1.61	0.90	1.17		22.0	2.17		(2.83)
	K	11.3	41	1.46	1.57	−0.05		− 3.55	20.3		(18.1)
	N	14.8	58	1.72		0.11		11.15			
	Y	12.0	49	1.26				1.35			
218	I	9.5	54	1.15	1.23	−0.23	− 1.75	− 0.60	19.3	6.86	19.4
	W	7.5	42	1.43	1.52	2.16	2.49	2.90	0.55	0.20	0.69
	F	6.8	35	1.57	0.48	1.48	12.55	2.80	0.51	0.45	1.90
	K	6.3	27	1.74	0.95	0.22	5.43	0.70	21.4	0.10	(12.3)
	N	11.1	59	1.74		1.69		3.85			
220	I	5.1	8	1.97	0.38			2.35	0.53		(2.72)
	W	9.0	55	1.11	1.22	−2.62		− 2.10	2.49		1.33
	F	6.2	35	1.49	0.48	0.89		1.65	4.22		(3.53)
	K	8.3	52	1.20	1.28			1.00	0.73		(1.81)
	N	8.0	50	1.62		2.86		3.15			
	Y	13.3	67	0.82	0.98	0.41		0.80	8.80		(10.7)
223	I	9.2	56	1.10	1.20	0.41	2.73	0.60	10.4	2.22	(14.4)
	W	6.3	36	1.57	0.60	6.26	17.85	3.05	0.65	0.36	0.39
	N	11.4	63	1.75		3.13		3.80			
	Y	7.4	46	1.35	1.42	6.01	0.40	7.45	1.59		(1.71)
226	I	16.1	62	0.95	1.10	−1.31	− 1.92	− 1.50	2.54	1.74	3.10
	W	13.3	56	1.10	1.20	−3.51	− 0.38	− 2.05	1.25	2.53	0.80
	F	13.2	58	1.11	1.17	−1.07	− 1.66	− 2.75	3.39	1.61	(1.70)
	K	10.9	47	1.31		−0.87	− 6.12	− 4.15			
	N	16.0	63	1.75				8.85			
	Y	8.0	22	1.83	0.82	1.97	5.12	3.25	1.37	0.05	(0.92)
228	I	12.5	55	1.13	1.22	1.47		0.70	2.74		1.79
	W	7.9	23	1.81	0.84	8.95		5.40	0.01		0.48
	F	10.3	46	1.35		4.16		1.25			
	N	16.5	64	1.75		2.81		1.45			
	Y	12.6	55	1.13	1.21	1.29		1.00	3.19		1.90
230	I	11.2	42	1.44	1.53	−2.39	− 4.27	− 0.95	2.19	0.12	(2.04)
	W	8.4	3	1.99	0.18	0.42	8.68	0.70	1.12	0.22	3.14
	F	9.3	25	1.79	0.90	−0.11	− 2.66	− 1.15			
	N	14.2	54	1.67		0.24		1.80			
236	W	12.4	59	1.01	1.17	2.28	7.89	0.70	0.13	3.00	
	K	10.9	55	1.13	1.22	−0.48	− 1.75	− 0.50	14.4	1.69	1.14
	N	16.7	68	1.73		−2.02		− 3.45			(15.8)
	Y	6.8	23	1.83	0.84	6.63		17.50	0.42	0.79	(1.15)
247	I	30.9	67	0.83	1.00	0.91		8.50	2.51		1.41
	W	30.1	67	0.84		1.60		4.25			
	F	28.9	66	0.87		1.31		13.40			
	K	25.4	62	0.96		1.61		8.30			
	N	28.2	65	1.75		1.15		10.00			
	Y	23.1	59	1.03	1.16	2.44		19.00	0.90		(0.85)
248	I	7.5	53	1.18	1.25	−1.02	− 9.20	− 0.60	6.65	1.41	5.60
	W	5.0	24	1.79	0.87	6.44	9.50	1.60	0.95	1.47	0.81
	N	11.2	66	1.74		1.94		1.40			
249	I	10.5	33	1.62	0.97	−0.54		− 0.55	5.00		(6.25)
	W	9.3	19	1.87	0.72	3.22		1.10	1.10		3.68
	N	13.8	50	1.62		1.23		1.50			
250	I	7.6	61	0.99		−1.51		− 0.50			
	F	4.6	37	1.55	1.58	1.04		0.80	11.7		(13.2)
	N	9.7	68	1.73		1.23		1.60			
251	F	10.4	60	1.01	1.14	6.23		1.05	0.72		0.92
	N	13.9	67	1.74		9.20		3.10			
253	I	8.5	39	1.49	1.60	1.12		1.40	7.94		(6.00)
	W	8.6	40	1.48	1.58	2.47		1.80	3.69		(5.00)

Δ_j: the hypocentral distance; i_j: the angle of incidence; $f_P(i_j)$, $f_S(i_j)$: the ratio of the amplitude observed on the ground surface to the one of incident P- and SV-waves, respectively, A_{PV}, $\bar{A}_{PV}$: the vertical components of theoretical and observed amplitudes of P-waves respectively, A_{SV}, $\bar{A}_{SV}$: the vertical components of theoretical and observed amplitudes of SV-waves respectively, (C): the case of conical type, (Q): the case of quadrant type.

P- and *SV*-waves in the case of clear commencement of *S*-waves, otherwise by the maximum amplitudes' ratio of both waves. In this calculation the ratios for the stations near nodal curves were excluded on account of their great uncertainty.

Moreover, Eq. (19) does not include the quantity relating to the magnitude of earthquake. It is therefore possible to study by superposing the relationships between the theoretical and observed amplitude ratios for all of these earthquakes, if all shocks were caused by the same mechanism of occurrence.

This relation for the *P*-waves is shown in Figs. 6 and 7, taking Wakanoura and

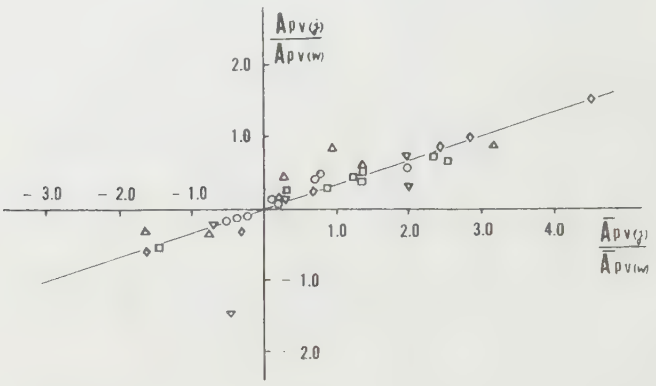

Fig. 6.

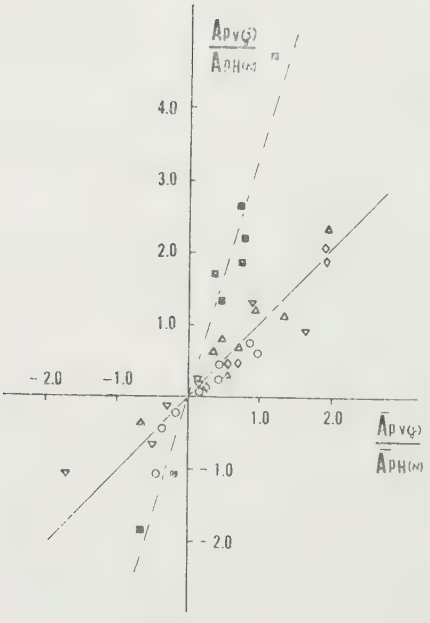

Amplitudes' ratios of initial *P*-waves between any station and a standard one in case of conical type. (ordinate: theoretical ratio, abscissa: observed ratio)
○: I, △: F, ▽: K, ◇: Y, □, ■: N-W

Fig. 7.

Nokami as the standard station respectively. The calculated errors in these ratios are illustrated in Fig. 8. In the former figures the mean values were adopted.

Provided that all assumptions thus far made are correct and that the "ground-coefficient" (which is defined only in this case as a factor of amplification effect of the ground or a stational correction, not included in Eq. (17)) and the response of seismometer used are the same in all stations, the plotted points indicating the above relation are expected to lie on the 45°-line. It can be said that in Fig. 6 these points lie on a certain straight line with satisfactory accuracy, but its gradient is less than 45°. This fact is considered to indicate that the amplitudes observed at Wakanoura are always smaller than the values expected from the theory throughout all shocks but the ground coefficients at another five stations are nearly equal. This can be ascertained also in Fig. 7 from the steeply inclined line indicating $A_{PV(W)}/A_{PH(N)}$ and the line of 45°-gradient relating to the other stations. The coefficient at Wakanoura is estimated to be about one third of that at other stations. This is reasonably explained from the fact that the station at Wakanoura is situated on a hill composed of solid rock (crystalline schist).

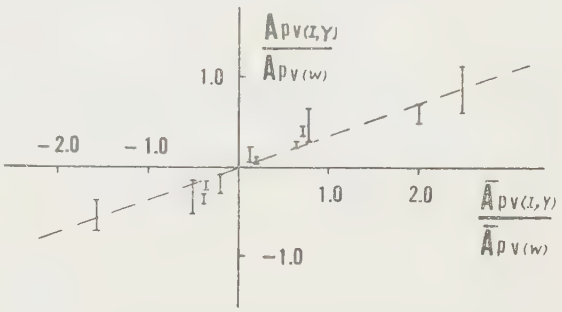

Fig. 8. Amplitude-ratios with calculated errors.

As can also be seen in Fig. 9, the observed amplitude-ratios of the P- and SV-waves may be in fairly good accord with the theoretical ratios.

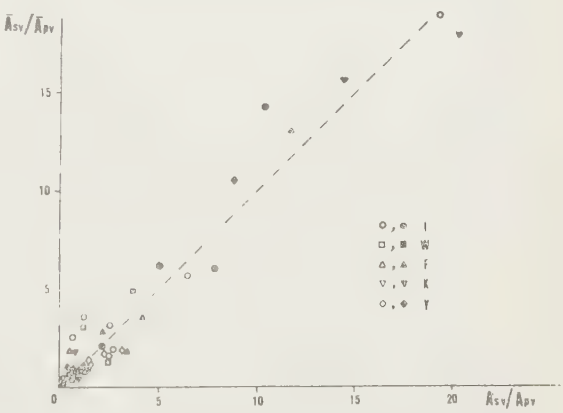

Fig. 9. Theoretical and observed amplitude-ratios of P- and SV-waves at the respective stations in case of conical type. (abscissa: theoretical ratio, ordinate: observed ratio)
Empty symbols denote the initial amplitude-ratios, and filled symbols indicate the maximum amplitude-ratios.

Taking these circumstances into consideration, we may safely consider that the mechanism of local eathquakes in this district is explainable to be of a conical type.

6. Comparison of amplitude distributions in the two types

For the sake of comparison, the theoretical amplitudes in the selected several

shocks were here estimated, assuming the push-pull distribution to be of a quadrant type.

The vertical amplitudes of the P- and SV-waves, which will be recorded on the ground surface, can be expressed, after H. Honda (**17, 26**), as follows:

$$\left.\begin{aligned} A_{PV} &= A_{P0} f_P(i_P) \sin 2\theta \cos\varphi \,, \\ A_{SV} &= A_{S0} f_S(i_S) \cos 2\theta \cos\varphi \,, \end{aligned}\right\} \tag{21}$$

where θ and φ are spherical coordinates taking a hypocentre as the origin.

Determining the distance between the epicentre and the point of intersection of nodal curves on the surface, the inclination and orientation of the polar axis (the intersection of two nodal planes), and hence, θ and φ can be obtained. The theoretical values calculated by Eq. (21) are also given in Table 2. Figs. 10 and 11 illustrate the relation between the theoretical and observed amplitudes analogously to Figs. 6 and 7.

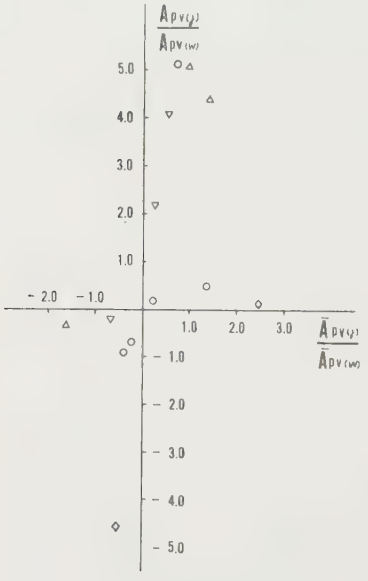

Fig. 10. Amplitudes' ratios of initial P-waves between any station and a standard one in case of a quadrant type.

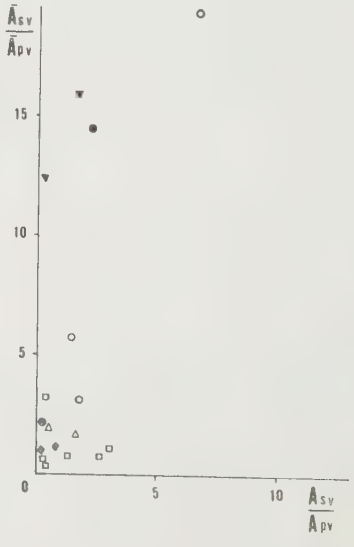

Fig. 11. Theoretical and observed amplitude ratios of P- and SV-waves in case of quadrant type.

Comparing the corresponding figures in the two types with each other, it is found that the plotted points in the case of the conical type scatter less widely than those in the case of the quadrant type. As a matter of course, it is dangerous to deny, from these results alone, a possibility of the latter type in the present case, owing to the poorer data and considerable ambiguity in the determination of nodal curves. However,

the former type of mechanism may be considered to give a more natural explanation for our observed results.

7. Some considerations

The generation mechanism of local shocks treated here can substantially be explained to be of a conical type, as described in the preceding sections. Hence in this section, some considerations will be made on this type of mechanism.

(1) Distribution of nodal cones.

In one of the studies on micro-earthquakes, the push-pull distribution of initial motions in many shocks was found to be identical with each other and similar to the main shock (**6**). However, this tendency could not be recognized in our observations.

Here, the distributions of some kinds of quantities about the nodal cone are briefly discussed in the following.

a) The frequency distribution of the half vertical angle of the cone, α, is shown in Fig. 12. For most of the earthquakes, it is found to be from 60° to 70°. The spectrum indicated in Fig. 12 seems to resemble a Gaussian distribution.

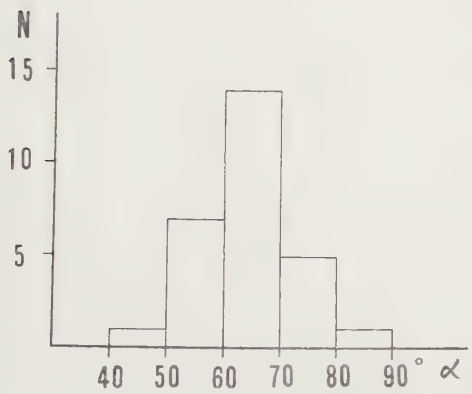

Fig. 12. Frequency distribution of α.

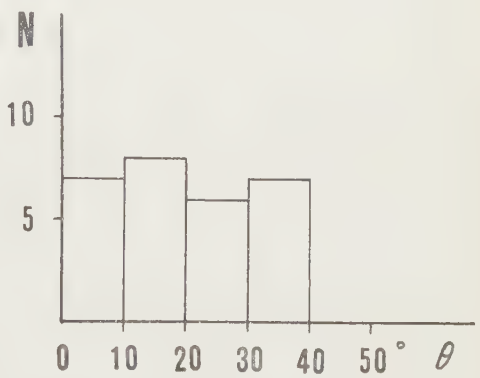

Fig. 13. Frequency distribution of θ.

b) Fig. 13 shows the histogram of the inclined angle to the ground surface, θ, of the conical axis. It seems in our case that the distribution of θ is limited within the range from 0° to 40°. We could not definitely find out the case in which the axis is so inclined that the nodal curve came to an ellipse. This agrees with Fukutomi's result (**27**), in which nodal curves were represented by a hyperbola for most of shallow earthquakes with focal depth from 0 to 25 km.

in $2t_0/\delta T$. Consequently, the travel-time difference between two groups may safely be interpreted to come from the azimuthal difference in the focal shape, though some questions remain unsolved. It may also be said that the present result has added a more possible ground to regard the shape of hypocentral domain as an approximate spheroid or linear source, as far as the present case is concerned.

If a general relationship between the vertical angle of nodal cone and the ratio of the wavelength to the dimension of origin is established, we shall obtain more definite informations about the dimension of focal region.

8. Conclusion

For the purpose of clarifying the mechanism of occurrence in micro-earthquakes, the push-pull pattern of initial motions and the amplitude distribution of the *P*- and *S*-waves was studied for a great number of local shocks generated in Wakayama District.

(1) The geographical pattern of the initial waves indicates a systematic distribution, but it is difficult to judge exactly, solely from the distribution, whether the mechanism is of a quadrant type or of a conical type. There seems to be many cases corresponding rather to the latter type.

(2) The distributions of theoretical amplitudes of the *P*- and *S*-waves in both types were calculated and compared with the observed values at each station. They are in fairly good accord with each other in the case of a conical type, while a larger discrepancy was found in a quadrant type. This fact may be considered to indicate that the mechanism of local earthquakes in this region can be explained to be of a conical type.

The amplitudes observed at Wakanoura are in a constant ratio smaller than the values expected from the theory. This is accepted by the reason that the station is situated on a hill composed of harder rock.

(3) On the basis of this result, the angle of vertex of nodal cone and the inclination angle of conical axis were estimated for all of the shocks. For the greater part of them a half-angle of the former was found to be $60°\sim70°$, and its frequency distribution is similar to a Gaussian distribution. The latter is distributed over $0°\sim40°$. Both of them do not seem to be related with the focal depth. No systematic pattern was recognizable in the geographical distribution of the orientations of conical axis.

(4) Some considerations were made on the origin of these shocks. A certain relationship seems to hold between the vertical angle of the nodal cone and the period of initial waves. It is probably possible to presume from this result that the focal region may have an azimuthal difference in its shape.

Acknowledgements

The writer wishes to express his cordial thanks to Prof. E. Nishimura for his kind guidance, and to Prof. K. Sassa for his instructive advice. Many thanks are also due to Mr. M. Ōtsuka, Dr. T. Nishitake and Mr. A. Kamitsuki for their valuable suggestions, and to Mr. K. Mori for drawing figures. The author is greatly indebted to the data obtained at the stations of the Earthquake Research Institute.

The expense for this study was partly defrayed by a grant-in-aid for scientific researches of the Ministry of Education.

REFERENCES

1. H. Kawasumi, A historical sketch of the development of knowledge concerning the initial motion of earthquake, Bur. Centr. Seism., Travaux Scientifique **15** (1937), 1.
2. H. Honda, The mechanism of the earthquakes, Sci. Rep. Tohoku Univ., [5], **9** (1957).
3. K. Kasahara, The natures of seismic origins as inferred from seismological and geodetic observations (2), Bull. Earthq. Res. Inst., **36** (1958), 21.
4. P. Byerly, Natures of faulting as deduced from seismograms, Geol. Soc. America, Special Paper, **62** (1955), 762.
5. J. H. Hodgson, Natures of faulting in large earthquakes, Bull. Geol. Soc. America, **68** (1957), 611.
6. H. Honda, On the mechanism and types of the seismograms of shallow earthquakes, Geophys. Mag., **5** (1932), 69.
7. B. Gutenberg, Mechanism of faulting in southern California indicated by seismograms, Bull. Seism. Soc. America, **31** (1941), 263.
8. P. G. Gane, P. Seligman and J. H. Stephen, Focal depths of Witwatersland tremors, Bull. Seism. Soc. America, **42** (1952), 239.
9. S. Omote, On the aftershocks of the Fukui Earthquake, Bull. Earthq. Res. Inst., **28** (1950), 311.
10. S. Omote, Aftershocks of Imaichi Earthquake observed at Nishi-oashi station, Bull. Earthq. Res. Inst., **28** (1950), 401.
11. T. Mikumo, Precise seismometric observations in the epicentral region of local shocks, Mem. Coll. Sci. Kyoto Univ., A**28** (1956), 161.
12. M. Ishimoto, Existence d'une source quadruple au foyer sismique d'après l'étude de la distribution des mouvements initiaux des secousses sismique, Bull. Earthq. Res. Inst., **10** (1932), 449.
13. H. Kawasumi, Study on the propagation of seismic waves (2nd Paper), Bull. Earthq. Res. Inst., **11** (1933), 403; **12** (1934), 660.
14. K. Sezawa, Dilatational and distortional waves generated from a cylindrical or a spheroidal origin, Bull. Earthq. Res. Inst., **2** (1927), 13.
15. T. Matuzawa, On the relative magnitude of the preliminary and the principal portion of earthquake motions, Jap. J. Astr. & Geophys., **4** (1926), 1.
16. M. Hasegawa, Die erste Bewegung bei einem Erdbeben, Beitr. z. Geophys., **27** (1930), 102.
17. H. Honda, On the amplitude of the *P* and *S* waves of deep earthquakes, Geophys. Mag., 8 (1934), 153.
18. W. Inouye, Notes on the origin of earthquake, Bull. Earthq. Res. Inst., **14** (1936), 582; **15** (1937), 956.
19. S. Takagi, On the origin of earthquake (2), (3), (4), Quart. J. Seism., C.M.O., **14**-3 (1950), 1; **17**-3 (1953), 53; **17**-4 (1953), 1 (in Japanese).

20. T. Hirono and T. Usami, Stress in an infinite medium around a spheroidal cavity applied with hydrostatic pressure, Pap. in Met. & Geophys., **5** (1954), 64.
21. T. Usami and H. Hirono, Elastic waves from a spheroidal cavity whose wall is subjected to normal stress of harmonic type, Pap. in Met. & Geophys., **7** (1956), 287; Geophys. **29** (1958), 11.
22. T. Minakami, Distribution des mouvements initiaux d'un séisme dont le foyer se trouve dans la couche superficielle et détermination de l'épaisseur de cette couche, Bull. Earthq. Res. Inst., **13** (1935), 114.
23. S. Takagi, On the origin of earthquake (10), Quart. J. Seism., C.M.O., **18**–2 (1953), 52 (in Japanese).
24. T. Matuzawa, An example in case of surface reflection of plane waves J. Seism. Soc., Japan, **3** (1932), 7 (in Japanese).
25. L. Knopoff, R. W. Fredricks, A. F. Gangi and L. D. Porter, Surface amplitudes of reflected body waves, Geophys., **22** (1957), 842.
26. H. Honda and H. Itō, On the reflected waves from deep focus earthquakes, Sci. Rep. Tôhoku Univ., **3** (1951), 144.
27. T. Fukutomi, Some statistical problems concerning intial earthquake motion, Bull. Earthq. Res. Inst., **11** (1933), 510.
28. T. Mikumo, On the periods of seismic waves observed in local earthquakes, Mem. Coll. Sci., Kyoto Univ., A**29** (1958), 1.

Memoirs of the College of Science, University of Kyoto, Series A,
Vol. XXIX, No. 2, Article 10, 1959.

MAGNETIC RESONANCE IN $Ti_mMg_nFe_{3-m-n}O_4$ FERRITES AND THEIR MAGNETIZATION*

BY

Tanehiro NAKAU

(*Received February 11, 1959*)

ABSTRACT

The ferromagnetic resonance absorption and the magnetization were measured on two natural single crystal samples of $Ti_mMg_nFe_{3-m-n}O_4$ ferrites (m=0.51, n=0.075, the Curie point=125°C; and m=0.50, n=0.072, the Curie point=135°C), from room temperature to −195°C. Each saturation magnetization obtained from magnetization measurement showed a broad maximum similar to those of Néel's P-type ferrites. The effective g-value and the magnetocrystalline anisotropy constant were obtained from resonance absorption experiments at the frequency of 25,700 Mc/sec. Each effective g-value showed a remarkable temperature dependence, corresponding to the above-mentioned feature of the magnetization. The magnetocrystalline anisotropy constant (first order anisotropy constant) changed with temperature in a somewhat similar manner to the magnetite, in agreement with the data on the magnetization. The anisotropy constant of one sample changed its sign at −155°C and that of the other at −133°C, and the direction of easy magnetization changed from the [1 1 1] to [1 0 0] direction with the decrease of temperature. These phenomena are discussed.

1. Introduction

Various investigations on ferromagnetic ferrites have been reported in recent years, and few ferrites (**1**∼**5**) are known to show any low temperature transition of magnetocrystalline anisotropy or any remarkable temperature dependence of the g-value observed in microwave absorption experiment.

In the present paper are reported the results of microwave resonance absorption experiments and magnetization measurements on two natural single crystal samples of $Ti_mMg_nFe_{3-m-n}O_4$ ferrites (m=0.51, n=0.075, the Curie point=125°C; and m=0.50, n=0.072, the Curie point=135°C)** of spinel type structure, as summarized in the following.

(1) Each first order anisotropy constant changed its sign at a certain low temperature, which might be a kind of low temperature transition.

* Read before the annual meetings of the Physical Society of Japan, Oct., 19, 1957 and Oct., 16, 1958.

** By spectral analysis, and other components such as Al, Cu, Mn and Si were negligible.

(2) The g-value obtained from the ferromagnetic resonance absorption experiment increased continuously with the decrease of temperature, between room temperature and the temperature at which the anisotropy constant changed its sign, thus showing a remarkable temperature dependence.

(3) A broad maximum of the saturation magnetization was observed at low temperatures*. This is similar in peculiarity to the ferrites of the general formula: $Ni_{1.5-a}Mn_aFeTi_{0.5}O_4$ $(0.4<a<0.675)$ known as Néel's P-type ferrites (**6, 7**). The details of these features will be described in § 3.

2. Experimental arrangement and samples

The method of measuring the resonance absorption was in principle the same as those (**1, 9**) reported by many authors. The sample was mounted in a rectangular resonant cavity driven in the TE_{102} mode and connected with a wave guide magic T bridge. The microwave frequency used was about 25,700 Mc/sec. The external static magnetic field was applied normal to the wide face of the wave guide and orthogonal to the r-f magnetic field. The cavity was thermally insulated from the rest of the wave guide system. A thermocouple was soldered on the cavity, for measuring the temperature.

The samples were prepared as follows. The sample No. 1 was cut in the (1 1 0) plane from a single crystal specimen of the Curie point 125°C and shaped into an ellipse about 0.024 cm thick, of the major axis about 0.18 cm long and the minor axis about 0.11 cm. The sample No. 2 was cut in the (1 0 0) plane from a single crystal specimen of the Curie point 135°C, to be about 0.041 cm thick and of the major axis about 0.18 cm long and the minor axis about 0.013 cm. The X-ray investigation showed that, in the sample No. 1, the direction of the major axis coincided with the [1 1 0] direction of the crystal and the cut plane made an angle of 0.087 radians with the crystal plane (1 1 0). And in No. 2, the cut plane made an angle of 0.087 radians with the crystal plane (1 0 0) and the crystal axis [1 0 0] was in the sample plane, making an angle of 45° with the major axis. The errors of the value of the first order anisotropy constant due to neglecting these errors in the cut plane inclination did not exceed about 3%. The demagnetizing factors were calculated by the method of Osborn (**10**).

The field intensity was measured by using both a proton meter and a fluxmeter calibrated by it.

---

* Read in part before the annual meeting of the Physical Society of Japan, Oct., 19, 1957. Recently, S. Akimoto, T. Katsura and M. Yoshida have reported that they found a particular mode of thermomagnetic curve similar to Néel's P-type ferrite with some specimens of synthetic polycrystals of titanomagnetites as solid solutions (reference 8).

A magnetic torsion balance (**11**) was used for the measurement of the magnetization*.

3. Experimental results

a. *Magnetic resonance*

The first order anisotropy constant was observed to change its sign at a low temperature. The crystalline anisotropy constant K_1 and the effective g-value were calculated from results of resonance absorption experiment by using the value of saturation magnetization obtained by the measurement of magnetization, while the second order anisotropy constant K_2 was neglected, since it was sufficiently small as compared with K_1 and was within the error of the experiment. The observation of resonance absorption was carried out continuously changing the temperature from the liquid nitrogen temperature to room temperature.

The absorption on a sample showed that the absorption was very broad near liquid nitrogen temperature, and especially in the [1 1 0] and [1 1 1] directions, the absorption changed according to both the intensity and the duration of the magnetic field previously applied to the sample. However, in the absorption of the sample which passed through such a process as follows, the above change almost disappeared and the measured results became steady and reproducible. Our results were obtained in this way.

The samples were cooled from room temperature to liquid nitrogen temperature in the magnetic field of 11,000~12,000 oersteds. After cooling, they were kept in the field of about 10,000 oersteds from liquid nitrogen temperature to a temperature about 40°C higher than the transition temperature of K_1** (−110°C in the sample No. 1 and −100°C in the sample No. 2) except for the case when the field strength was decreased for the observation of resonance. Further, the resonance was observed with the field strength decreasing, because of the low permeability of the specimen. The analysis of results was limited from room temperature to a temperature near the transition temperature of K_1, since the resonance absorption became very broad and moreover a second order deformation of crystal structure might be expected below the transition temperature of K_1. The absorption was measured by observing the relative absorption, i.e. the change in the power P_r reflected from the cavity on

* The fused silica was used. The temperature was measured by a thermocouple set near the position of the sample. For the correction, the simultaneous measurements of the temperatures at this position and at the position of the sample were also carried out. The character of the magnetization measuring apparatus was tested to be good for the purpose by using a thin nickel plate of 0.004 cm thick.

** The temperature at which K_1 changes its sign is called the transition temperature of K_1 in the following.

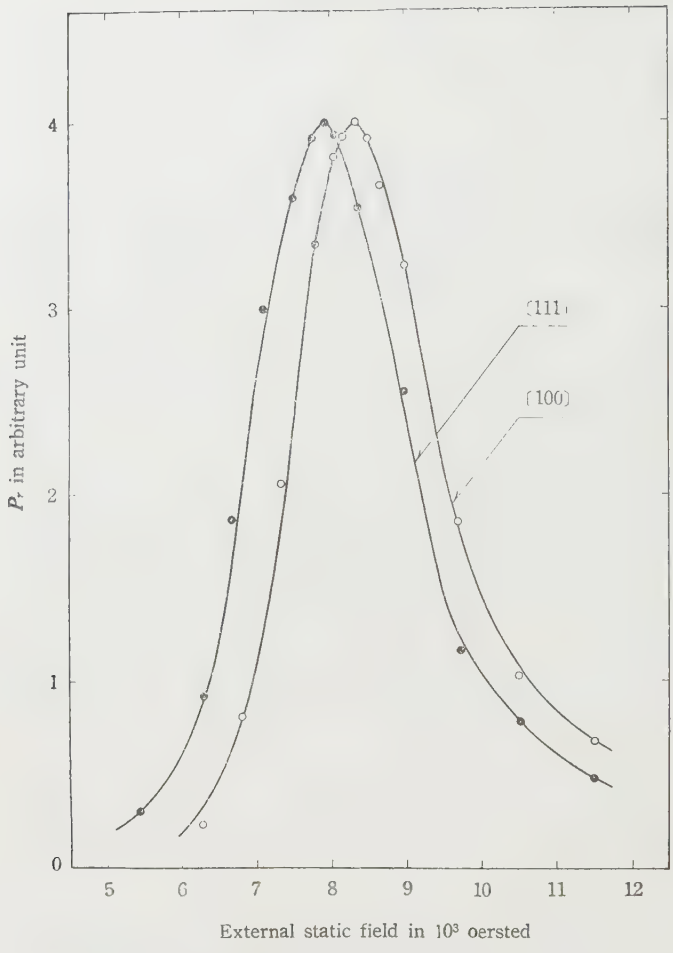

Fig. 1. Absorption curves of the sample No. 1 at room temperature.

resonance, with the incident power P_i maintained constant. It gives also qualitative information of the line breadth. The effective g-value and the value of K_1 were calculated from the following expressions (1), (2a), (2b), (3a) and (3b) derived from the general formula (**12**) of resonance condition and corrected with respect to the inclination errors mentioned in §2.

When a sample is an ellipsoidal ferromagnetic body whose principal axes are x, y, z-axes, the resonance angular frequency ω in the case of cubic symmetry is given by

$$\omega = \gamma\{[H_\zeta + (N_x\cos^2\theta + N_z\sin^2\theta - N_x\sin^2\theta - N_z\cos^2\theta + N_\xi^e)M] \times [H_\zeta + (N_y - N_x\sin^2\theta - N_z\cos^2\theta + N_\eta^e)M]\}^{1/2} \quad (1)$$

under appropriate conditions. Here, the coordinate system (ξ, η, ζ) is obtained by the rotation through the angle θ round the y-axis ($y \equiv \eta$), and H_ζ is the external static magnetic field, the other quantities being usual ones (**13, 14**).

For a sample whose (1 0 0) plane is parallel to the $(\xi\zeta)$ plane, by neglecting K_2 which is small as compared with K_1, N_ξ^e and N_η^e are given by

$$N_\xi^e = (K_1/M^2)\cos 4\phi\,, \tag{2a}$$

$$N_\eta^e = \left(\frac{3}{2}+\frac{1}{2}\cos 4\phi\right)K_1/M^2\,, \tag{2b}$$

where ϕ is the angle between ζ-axis and [1 0 0] direction. If the (1 1 0) plane is parallel to the $(\xi\zeta)$ plane, we have

$$N_\xi^e = (2-\sin^2\phi-3\sin^2 2\phi)K_1/M^2\,, \tag{3a}$$

and

$$N_\eta^e = 2\left(1-2\sin^2\phi-\frac{3}{8}\sin^2 2\phi\right)K_1/M^2\,. \tag{3b}$$

When the $(\xi\zeta)$ plane makes a small angle with either of the (1 0 0) and (1 1 0) planes, the resonance condition differs from the expression (1).

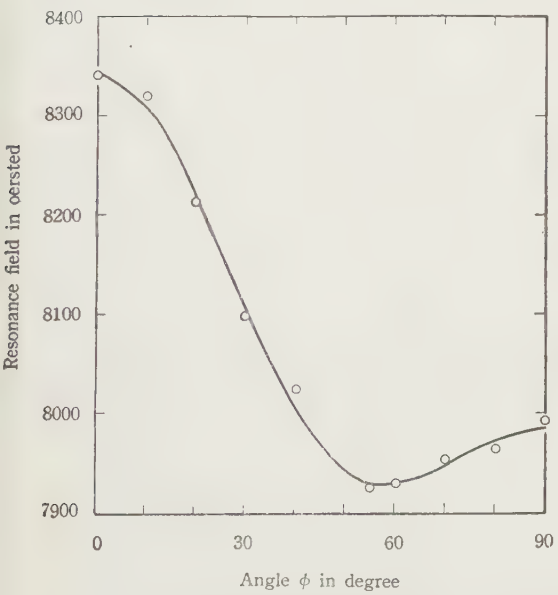

Fig. 2. Resonance field *versus* crystal orientation in the (110) plane of the sample No. 1 at room temperature.

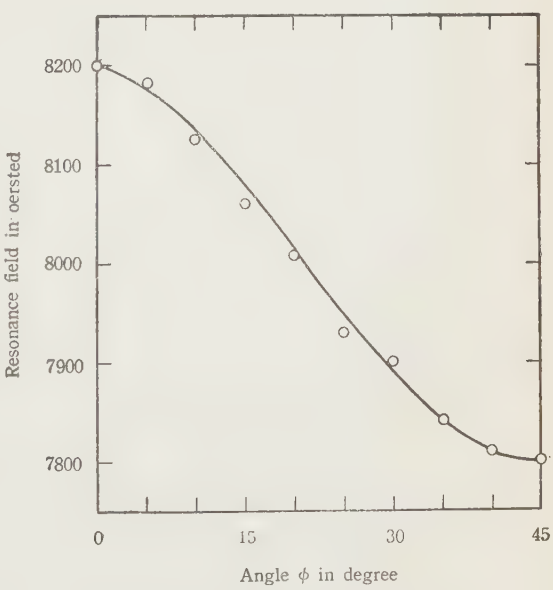

Fig. 3. Resonance field *versus* crystal orientation in the (100) plane of the sample No. 2 at room temperature.

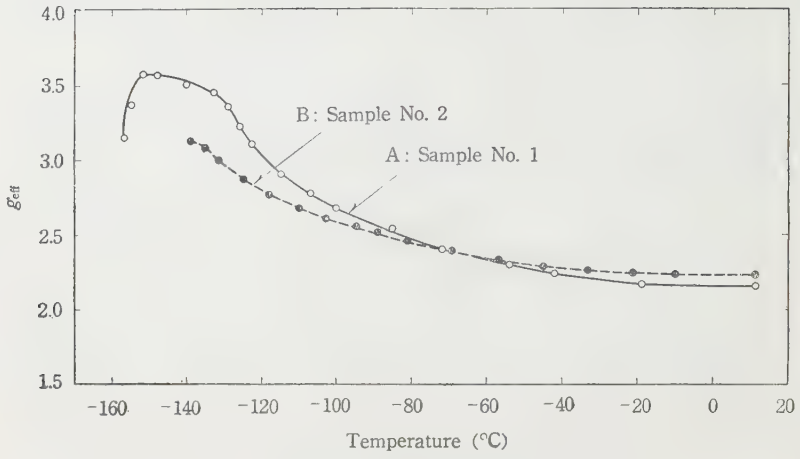

Fig. 4. Temperature dependence of effective g-value.

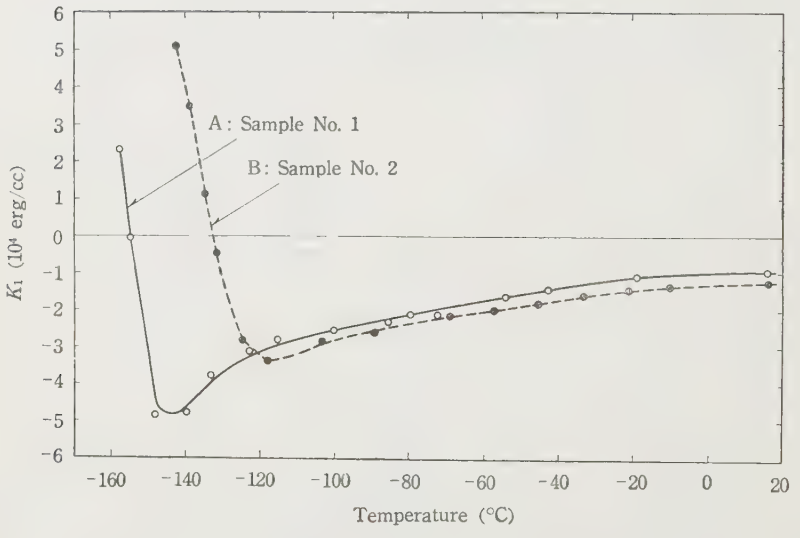

Fig. 5. Temperature dependence of anisotropy constant K_1.

Table I.

Sample	g_{eff}	K_1
No. 1	2.17 ± 0.04	$(-0.96 \pm 0.15) \times 10^4$ ergs/cc
No. 2	2.23 ± 0.04	$(-1.26 \pm 0.19) \times 10^4$ ergs/cc

The sample No. 1

In this case, the sample was cut in the (1 1 0) plane. The magnetic absorption was observed mainly in the [1 0 0], [1 1 0] and [1 1 1] directions, applying the external static magnetic field parallel respectively to these directions and perpendicular to the r-f magnetic field parallel to the (1 1 0) plane.

Fig. 1 shows the relative absorption at room temperature in the [1 0 0] and [1 1 1] directions. Table I gives the average values of effective g-value and K_1 at room temperature. Fig. 2 shows the resonance field at room temperature as a function of crystal orientation. ϕ is the angle between the [1 0 0] direction and the external static field. The field strength at resonance decreased continuously with the decrease in temperature, so that the effective g-value became large at low temperature. This phenomenon is parallel to the change of magnetization *versus* temperature. The curve A in Fig. 4 represents the temperature dependence of the effective g-value calculated from the experimental results. The increasing tendency of the effective g-value becomes distinct around the temperature where the magnetization stops increasing (cf. Fig. 9). The curve A in Fig. 5 shows the value of K_1 *versus* temperature, calculated from the experimental results. From this, it is recognized that the first order anisotropy constant changes its sign at about −155°C and consequently the direction of easy magnetization changes.

With the decrease in temperature, the absorption became broad as shown in Figs. 1 and 6. This phenomenon corresponds to the decrease in permeability at low temperature. At about −160°C, the absorption became very broad and the effective g-value showed the decreasing tendency also. These might be associated with a kind of low temperature transition.

The values of K_1 and effective g-value are given in Table II.

Table II.

Temperature (°C)	g_{eff}	K_1 (10^4 ergs/cc)
−157	3.15	+2.05
−155	3.37	−0.03
−148	3.57	−4.94
−140	3.50	−4.75
−133	3.45	−3.73
−123	3.10	−3.12
−115	2.91	−2.86
−100	2.67	−2.58
− 85	2.53	−2.37
− 79	2.41	−2.07
− 72	2.40	−2.11
− 54	2.29	−1.61
− 42	2.24	−1.47
− 19	2.17	−1.08

The sample No. 2

The sample No. 2 was cut in the (1 0 0) plane. Magnetic absorption was observed mainly in the [1 0 0] and [1 1 0] directions and the direction making an angle of 15° with the [1 0 0] direction in the (1 0 0) plane.

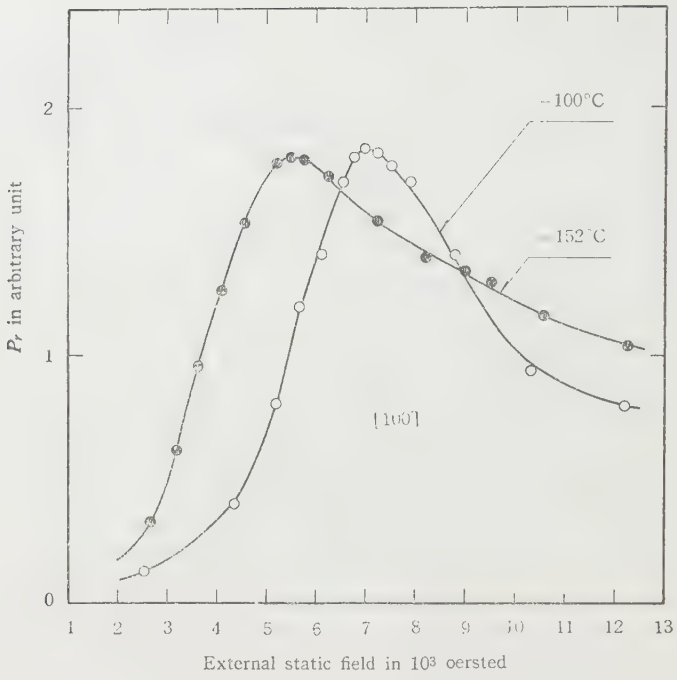

Fig. 6. Absorption curves in the [100] direction of the sample No. 1 at −152°C and −100°C.

In this case, the external static magnetic field was applied parallel to the (1 0 0) plane and normal to the r–f magnetic field parallel to the (1 0 0) plane.

The experimental results were essentially the same as those with the sample No. 1. The temperature dependence of the effective g–value was similar to that of the sample No. 1, and the first order anisotropy constant K_1 changed its sign at a low temperature as in the sample No. 1.

Fig. 3 shows the experimental value of the resonance field as a function of the crystal orientation. ϕ is the angle between the external static magnetic field and the [1 0 0] direction. The effective g–value is plotted as a function of temperature in the curve B of Fig. 4. The curve B in Fig. 5 gives the value of K_1 as a function of temperature, showing that K_1 changes its sign at about −133°C. The increasing tendency of K_1 is remarkable in the figure at temperatures near the transition temperature of K_1, but the curve becomes flat at lower temperatures, under the assumption that the crystal is still cubic below −152°C, though the value of K_1 was not plotted for the reason mentioned above.

The value of K_1 and the effective g–value are listed in Tables I and III.

The results obtained from the resonance absorption experiment on the sample

No. 2 agreed with those on the sample No. 1 in main features. In the sample No. 2, the temperature at which an anomaly starts in the resonance broadness and the decrease of effective g-value was by about 15°C lower than the transition temperature of K_1, while in the sample No. 1, the corresponding temperature almost agreed with the transition temperature of K_1, thus the anomaly temperatures of the two samples being near together. This difference may be induced by any difference in condition of crystallization, though contents of their main components are not the same.

Table III.

Temperature (°C)	g_{eff}	K_1 (10^4 ergs/cc)
−142	3.04	+5.12
−139	3.12	+3.48
−135	3.09	+1.14
−132	3.00	−0.48
−125	2.86	−2.79
−118	2.77	−3.38
−103	2.60	−2.86
− 89	2.51	−2.59
− 69	2.40	−2.20
− 57	2.34	−2.01
− 45	2.29	−1.82
− 33	2.26	−1.62
− 21	2.24	−1.46
− 10	2.23	−1.33

b. Magnetization

The experimental results of measurement of magnetization showed a fall of magnetization and a change in the direction of easy magnetization at low temperatures. It was studied whether the feature of the fall of magnetization is the same as that displayed by magnetite (**15, 16, 17**) or not. We observed the warming curve of magnetization in various fields and the magnetization curve after cooling in strong field as well as in zero field. The result showed that the fall of magnetization at low temperatures was not similar to that of magnetite but similar to that of Néel's P-type ferrite; namely the curve of saturation magnetization *versus* temperature showed a broad maximum. This property corresponds to the increasing tendency of the effective g-value in the resonance absorption at low temperatures. The experimental results are described in the following.

The sample No. 1

The magnetization curves in Fig. 7 show that the direction of easy magnetization changes from the [1 1 1] to [1 0 0] direction at low temperatures*. The value of the anisotropy constant K_1 was calculated by using results of the resonance absorption at temperatures near and above the transition temperature of K_1. However, K_1 was calculated from the difference between the energies required for magnetization obtained from the magnetization curves. The value was of the order of 10^5 erg/cc at −180°C, on the assumption that the crystal has a cubic symmetry.

* A simple observation was made for ascertaining the change of the direction of easy magnetization: a sample placed in magnetic field rotated at low temperatures with temperature decrease, which corresponds to the change of the direction of easy magnetization.

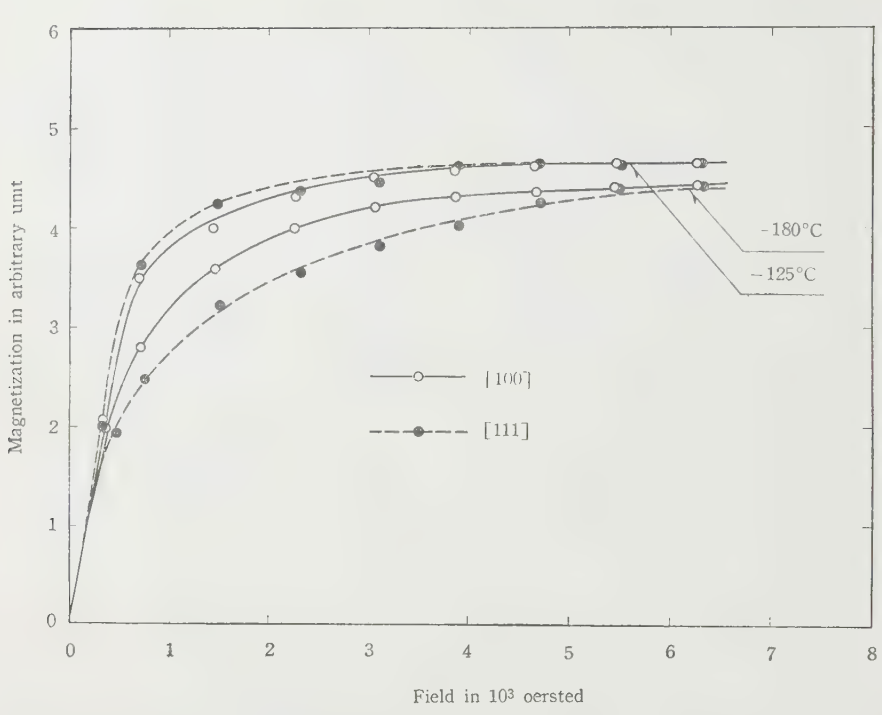

Fig. 7. Magnetization curves in the [100] and [111] directions of the sample No. 1.

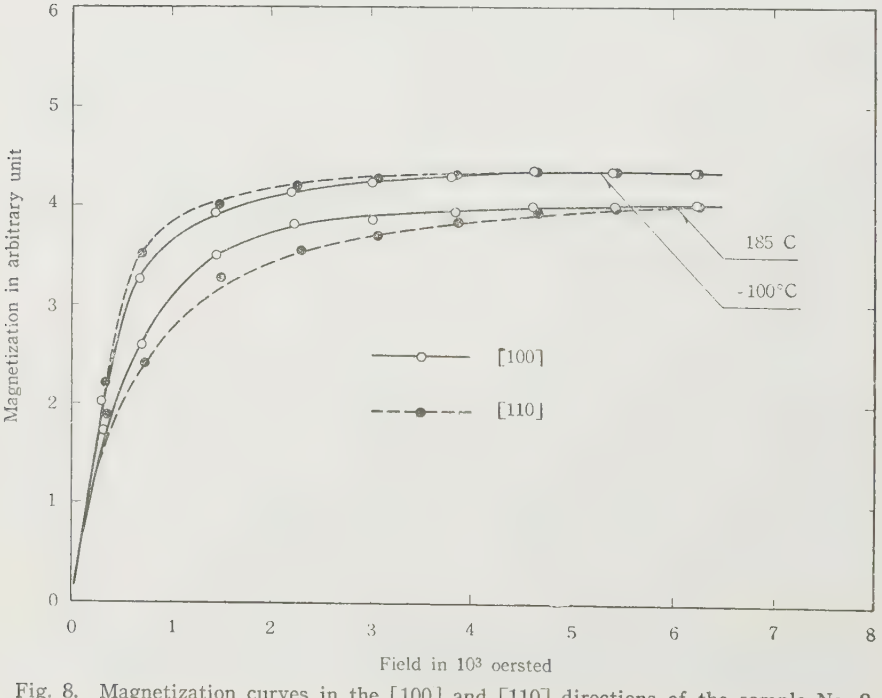

Fig. 8. Magnetization curves in the [100] and [110] directions of the sample No. 2.

The saturation magnetization was determined by using a nickel plate* as the standard. The value of saturation magnetization** at room temperature was 95 cgs. The curve A in Fig. 9 represents a temperature dependence of magnetization in the [1 0 0] direction of the sample No. 1. This is a warming curve in which the value of magnetization was measured in the field of 8,000 oersteds after cooling in the field of 11,000 oersteds in the [1 0 0] direction from room temperature to liquid nitrogen temperature. This curve can be regarded to show the curve of saturation magnetization *versus* temperature as shown in the discussion later. The curve A in Fig. 10 shows a warming curve of magnetization in the [1 1 1] direction in the field of 7,200 oersteds. From these results, it can be supposed that the values of magnetization

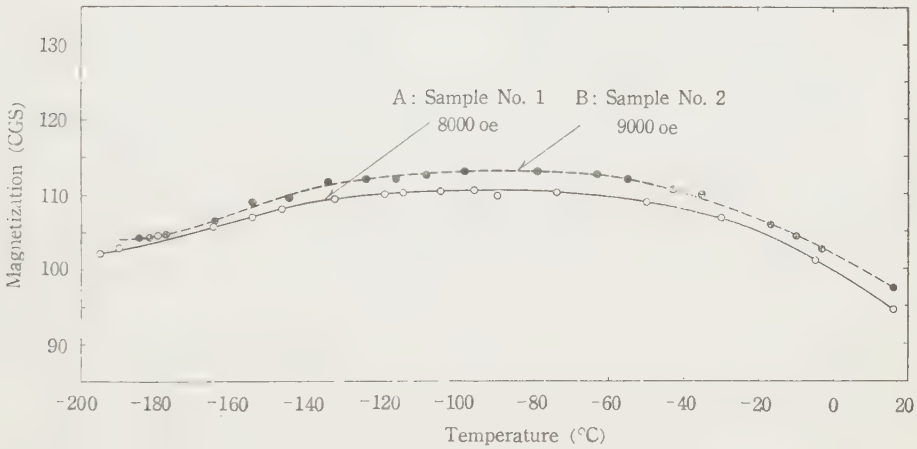

Fig. 9. Warming curves in the [100] direction of the samples No. 1 and No. 2 after cooling in field of 11,000 oersteds parallel to [100].

in various directions of the crystal almost coincide with each other in such strong fields, in spite of the influence of crystalline anisotropy, etc. The magnetization curves in Fig. 11 were obtained after cooling from room temperature to liquid nitrogen temperature in the field of 11,000 oersteds in the [1 0 0] direction. The values at --190°C were obtained by decreasing the field strength and the values at −180°C by increasing the field strength from zero. In either case, the magnetization took the nearly saturated value in the field of about 3,000 oersteds. Therefore, it is resonable to regard the fall of magnetization as that of the saturation magnetization. Besides, by considering the magnitization curves in Figs. 7 and 11, it is concluded that the magnetization in Fig. 9 represents the value of saturation magnetization.

* The nickel content being 99.6%.

** From this measurement, the value per gramme is known, and the value per unit volume is calculated, using the density determined from lattice constant of pure titanomagnetite, since the error seems to be within about 1% (reference 18).

The temperature dependence of saturation moment (per gramme) is represented by a smooth curve as shown in Fig. 13, so the crystal is evidently of sufficiently stable single phase (**18**, **19**, **20**).

The sample No. 2

The magnetization was observed in the [1 0 0] and [1 1 0] directions. The magnetization curves in Fig. 8 show that the direction of easy magnetization changes as in the sample No. 1. The energy difference obtained from the magnetization curves gives also the value of the order of 10^5 erg/cc at $-185°C$, on the same assumption as with the sample No. 1.

The value of saturation magnetization at room temperature was 98 cgs. A warming curve of the magnetization in the [1 0 0] direction is shown in Fig. 9. The value of magnetization was obtained in the field of 9,000 oersteds after cooling in the field of 11,000 oersteds in the [1 0 0] direction. The temperature at which the magnetization begins to fall is higher than that of the sample No. 1. A warming curve of magnetization in the [1 1 0] direction is shown in Fig. 10. From the curves in Fig. 8 and the magnetization curve in Fig. 12 which was obtained after cooling in the field of 6,400 oersteds, it is evident that the curve B in Fig. 9 shows that of saturation magnetization versus temperature. The temperature dependence of saturation moment is also quite similar to that of the sample No. 1. Thus the features of the sample No. 2 are essentially the same as those of the sample No. 1.

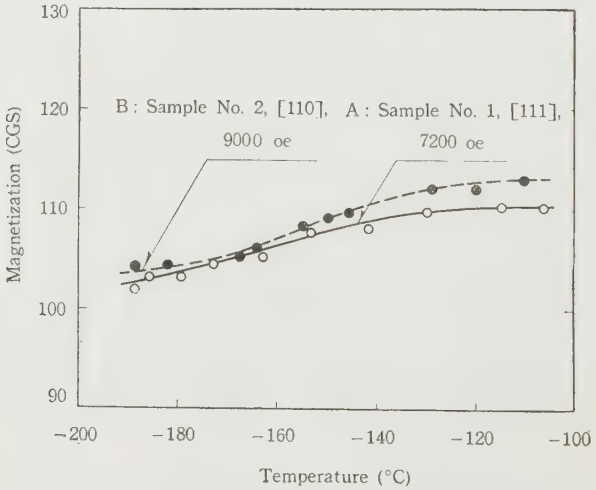

Fig. 10. Warming curves in the [111] direction of the sample No. 1 and in the [110] direction of the sample No. 2.

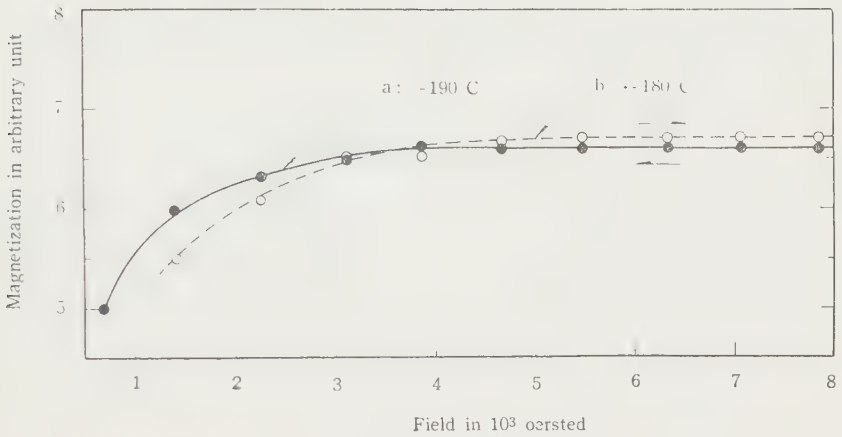

Fig. 11. Magnetization curves in the [100] direction of the sample No. 1 at −190°C and −180°C after cooling in the field of 11,000 oersteds parallel to [100].

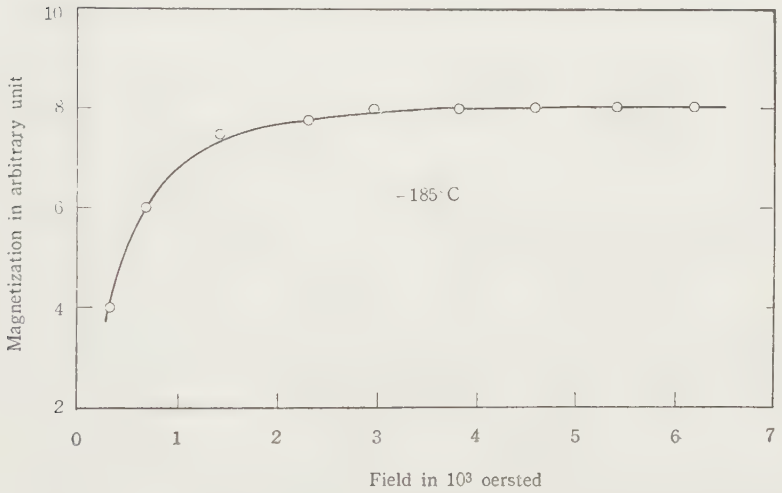

Fig. 12. Magnetization curve in the [100] direction of the sample No. 2 at −185°C after cooling in the field of 6,400 oersteds parallel to [100].

4. Discussion of results

The structure of the specimens is of spinel type, and their direction of easy magnetization changed from the [1 1 1] to [1 0 0] direction as shown in Fig. 5, in accordance with the results of measurement of magnetization. This phenomenon is somewhat similar to that of magnetite. In magnetite, the data by Bickford (**1**) show that the transition temperature of the crystalline anisotropy is by about 12°C lower than the temperature at which the first order anisotropy constant changes its sign.

Besides, a sudden fall of the magnetization and the other anomalies are observed around the transition temperature (**15**, **16**, **17**, **21**, **22**). In the present specimens, however, such a clear sudden fall as observed in magnetite could not be found, though an anomaly in magnetic resonance absorption was observed as described in § 3. The phenomena in magnetite are related to the ordered arrangement of ferrous and ferric ions in octahedral lattice sites (**21**, **23**). But it is not accepted that such a mechanism might contribute to interpreting the phenomena in the present case, since plausibly Fe^{3+} ions as a small content of metal ions and Fe^{2+} ions as a large content exist together in octahedral lattice sites. Then, titanium ions might play an important role in the present phenomena from a structural point of view.

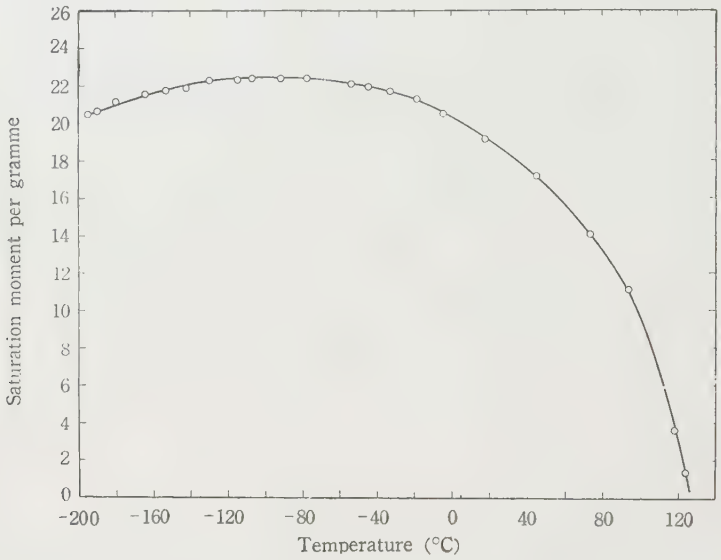

Fig. 13. Saturation magnetization *versus* temperature of the sample No. 1.

We try an explanation for the increase of effective g-value with the decrease of temperature by using the formula derived by Wangsness (**24**) and others (**6**, **25**). Now, at 0°K, the effective g-value is given by

$$g_{\text{eff}} = (\sum g_{A_i} S_{A_i} - \sum g_{B_i} S_{B_i}) / (\sum S_{A_i} - \sum S_{B_i}) , \qquad (4)$$

where S_{A_i} and S_{B_i} are respectively the resultant electron spin quantum numbers of an individual ion in A sites (tetrahedral sites) and B sites (octahedral sites). In order to evaluate g_{eff} as a function of temperature, S_{A_i} and S_{B_i} in (4) are replaced by $S_{A_i} B_{A_i}$ and $S_{B_i} B_{B_i}$, where B_{A_i}, B_{B_i} are Brillouin functions.

Then, for simplifying the problem, we consider titanomagnetites, where the configuration of titanium ions governs the magnetization, though magnesium ions of

small content might play a particular role. If the Ti^{4+} ions are assumed to occupy always B sites, for $m \geqq 0.5$ the configuration of $Ti_mFe_{3-m}O_4$ can be given by

$$Fe^{3+}_{2-2m}Fe^{2+}_{2m-1}(Fe^{2+}_{2-m}Ti^{4+}_{m})O^{2-}_4$$

with the saturation moment $(2-2m)\mu_B$, (**26**, **27**)

where the ions in the bracket occupy B sites. As Néel (**26**) pointed out, however, the experimental facts are not sufficiently existing to support this formula.

A calculation of g_{eff} using $Ti_{0.5}Fe_{2.5}O_4$ as an approximation is carried out on the assumption that the configuration is represented by the above formula. Now, Fe^{3+} ions occupy A sites only and Fe^{2+} ions B sites only. The atomic ground state of Fe^{3+} ion is ^6S and that of Fe^{2+} ion ^5D. So it is reasonable that g_A is 2. When g_B is 2.2, g_{eff} becomes 3.2 from (4), because S_A is 5/2 and S_B is 2. If the effective g-value at the temperature at which K_1 changes its sign is equal to that at 0°K, this value almost agrees with the experimental value of the sample No. 2. A trial calculation of g_{eff} and the magnetization as functions of temperature for $Ti_{0.5}Fe_{2.5}O_4$ was carried out by using the above values of g's and Brillouin functions in the case of $S_A=5/2$ and $S_B=2$, adjusting the parameters such that the effective g-value and the magnetization take the values near the experimental values. It could explain qualitatively the experimental results. However, since the formula for g_{eff} is an approximate one and the parameters mentioned above are obtained by the measurement of susceptibility at high temperatures (**7**), we will not go further into the discussion of g_{eff}. The decrease of the effective g-value may be another problem considering it as an anomaly.

From the above-mentioned formula, the saturation moment at 0°K is evaluated by assuming the formula $[Ti_lFe_{3-l}O_4]_{1-n}[MgFe_2O_4]_n$ for $Ti_mMg_nFe_{3-m-n}O_4$. If $[MgFe_2O_4]$ has the formula $[Fe^{3+}(Mg^{2+}Fe^{3+})O^{2-}_4]$, the calculated saturation moment at 0°K is $0.83\,\mu_B$ for the specimen No. 1 and $0.86\,\mu_B$ for the specimen No. 2. These values show good agreement with the values $0.81\,\mu_B$ and $0.83\,\mu_B$ for the specimens No. 1 and No. 2 at 0°K respectively as estimated from the curves in Fig. 9.

Toe broadness of the absorption is evidently related to the low permeability, though it may also be due to other causes.

For a more exact explanation of the above phenomena, we need other measurements at low temperatures, i.e., measurements of electrical conductivities, specific heat and etc., and also X-ray study at low temperatures.

Acknowledgments

The author wishes to thank cordially Professor I. Takahashi for his kind guidance. He is also indebted to Professor N. Kumagai, Dr. N. Kawai and Mr. S. Kume for the

use of their equipment and for their help, and to Mr. T. Seto for his X-ray analysis, to Mr. S. Okasaki of Matsushita Elec. Co. for his spectral analysis, and to Dr. K. Yoshida for his useful discussions.

REFERENCES

1. L. R. Bickford, Phys. Rev., **78** (1950), 449.
2. D. W. Healey, Phys. Rev., **86** (1952), 1009.
3. W. A. Yager, J. K. Galt and F. R. Merrit, Phys. Rev., **99** (1955), 1203.
4. T. Okamura, Y. Torizuka and Y. Kojima, Phys. Rev., **84** (1951), 372.
5. T. R. McGuire, Phys. Rev., **97** (1955), 831.
6. E. W. Gorter, Philips Res. Rep., **9** (1954), 295, 321, 403.
7. L. Néel, Ann. Phys., **3** (1948), 137.
8. S. Akimoto, T. Katsura and M. Yoshida, J. Geomag. Geoelect., **9** (1957), 165.
9. R. D. Arnold and A. F. Kip, Phys. Rev., **75** (1949), 1199.
10. J. A. Osborn, Phys. Rev., **67** (1945), 351.
11. N. Kawai, Report International Congress, Mexico (1956).
12. J. Smit and H. G. Beljers, Philips Res. Rep., **10** (1955), 113; H. Suhl, Phys. Rev., **97** (1955), 555.
13. C. Kittel, Phys. Rev., **73** (1948), 155.
14. C. Kittel, Phys. Rev., **76** (1949), 743.
15. P. Weiss and R. Forrer, Ann. Phys., [10] **12** (1929), 279.
16. C. A. Domenicalli, Phys. Rev., **78** (1950), 458.
17. B. A. Calhoun, Phys. Rev., **94** (1954), 1577.
18. N. Kumagai, N. Kawai and S. Kume, Memo. Coll. Sci. Univ. Kyoto, **21** (1954), 287.
19. N. Kawai, S. Kume and S. Sasajima, Proc. Japan Acad., **30** (1954), 588.
20. N. Kawai, Proc. Japan Acad., **31** (1955), 346.
21. E. J. W. Verwey, Nature **144** (1939), 327; E. J. W. Verwey and P. W. Haayman, Physica **8** (1941), 979.
22. S. C. Abrahams and B. A. Calhoun, Acta. Cryst., **6** (1953), 105.
23. C. G. Shull, Colloque International de Magnétisme de Grenoble, (1958).
24. R. K. Wangsness, Phys. Rev., **91** (1953), 1085.
25. N. Tsuya, Prog. Theor. Phys., **7** (1952), 263.
26. L. Néel, Advanc. Phys., **4** (1955), 191.
27. E. W. Gorter, Advanc. Phys., **6** (1957), 336.

CONTENTS

Optical Observations of the Second Russian Earth Satellite.

By *Akira Hattori* and *Bunta Yada* 107

Absolute Measurement of γ-quanta.

By *Teruo Nakamura, Kiyoji Fukunaga, Kunio Takamatsu* and *Shinjiro Yasumi* 141

Ferromagnetic Resonance in Ni-Cd Ferrite System at Microwave Frequencies.

By *Susumu Takemoto* 153

On Local Character of Poisson's Ratio in the Earth's Crust.

By *Akira Kamitsuki* 163

Adiabatic Compressibility of Aqueous Solution of Inorganic Acid.

By *Yoshio Ishida* 187

A New Compound in Au-Pb Alloy System.

By *Yoshibumi Fujiki* 197

Nuclear Magnetic Resonance Pulse Apparatus.

By *Tsuneo Hashi, Akira Hirai, Masahumi Sasaki* and *Takao Kawai* 205

On Azimuthal Distribution of the Crustal Poisson's Ratio in case of Earthquake Occurrence.

By *Akira Kamitsuki* 213

A Consideration on Generation Mechanism of Local Earthquake.

By *Takeshi Mikumo* 221

Magnetic Resonance in $Ti_mMg_nFe_{3-m-n}O_4$ Ferrites and their Magnetization.

By *Tanehiro Nakau* 241

Printed by NIPPON INSATSU SHUPPAN

Fukushima, Osaka